

# REPORT DOCUMENTATION PAGE

Form Approved  
OMB NO. 0704-0188

Public Reporting burden for this collection of information is estimated to average 1 hour per response, including the time for reviewing instructions, searching existing data sources, gathering and maintaining the data needed, and completing and reviewing the collection of information. Send comment regarding this burden estimates or any other aspect of this collection of information, including suggestions for reducing this burden, to Washington Headquarters Services, Directorate for information Operations and Reports, 1215 Jefferson Davis Highway, Suite 1204, Arlington, VA 22202-4302, and to the Office of Management and Budget, Paperwork Reduction Project (0704-0188,) Washington, DC 20503.

1. AGENCY USE ONLY ( Leave Blank)		2. REPORT DATE May 2006		3. REPORT TYPE AND DATES COVERED Final Report 01 July 00 - 31 July 05	
4. TITLE AND SUBTITLE Very Low NF, High DR Heterodyne RF Lightwave Links Using a Simple, Versatile Photonic Integration Technology				5. FUNDING NUMBERS DAAD19-00-1-0415	
6. AUTHOR(S) Stephen R. Forrest					
7. PERFORMING ORGANIZATION NAME(S) AND ADDRESS(ES) Princeton University School of Engineering and Applied Sciences Engineering Quad Princeton, NJ 08544				8. PERFORMING ORGANIZATION REPORT NUMBER	
9. SPONSORING / MONITORING AGENCY NAME(S) AND ADDRESS(ES)  U. S. Army Research Office P.O. Box 12211 Research Triangle Park, NC 27709-2211				10. SPONSORING / MONITORING AGENCY REPORT NUMBER  4 1 3 1 4 . 1 - E L - D R P	
11. SUPPLEMENTARY NOTES The views, opinions and/or findings contained in this report are those of the author(s) and should not be construed as an official Department of the Army position, policy or decision, unless so designated by other documentation.					
12 a. DISTRIBUTION / AVAILABILITY STATEMENT  Approved for public release; distribution unlimited.				12 b. DISTRIBUTION CODE	
13. ABSTRACT (Maximum 200 words)  The program goals were to demonstrate ultra-low noise RF links, and to demonstrate several key integrated optoelectronic components employing a versatile asymmetric twin waveguide technology. All objectives set forth in the proposal were either met or exceeded. These achievements included: Demonstration of a versatile integration technology based on the asymmetric twin waveguide platform that allowed for the realization of a broad range of components useful in RF photonic components. This resulted in the demonstration of a fully integrated heterodyne receiver operating to 5 GHz, as well as balance photodiode/semiconductor optical amplifier pairs, and a wavelength tunable laser used as the local oscillator on the ATG platform. In addition we have demonstrated the highest bandwidth heterodyne links operating at 5GHz and 16GHz. These links were based on phase modulation and represent an extremely high sensitivity route to analog optical transmission. Paths to commercialization involve a close partnership Apogee Photonics, Inc., a start up from our group whose charter is to fabricate low cost photonic integrated circuits based on twin waveguide technology.					
14. SUBJECT TERMS				15. NUMBER OF PAGES	
				16. PRICE CODE	
17. SECURITY CLASSIFICATION OR REPORT <b>UNCLASSIFIED</b>		18. SECURITY CLASSIFICATION ON THIS PAGE <b>UNCLASSIFIED</b>		19. SECURITY CLASSIFICATION OF ABSTRACT <b>UNCLASSIFIED</b>	
				20. LIMITATION OF ABSTRACT  <b>UL</b>	

**REPORT DOCUMENTATION PAGE (SF298)  
(Continuation Sheet)**

**(1) List of papers submitted or published under contract sponsorship**

**(a) Manuscripts submitted, but not published:**

None

**(b) Papers published in peer-reviewed journals:**

1. "Monolithic integration of a semiconductor optical amplifier and a high bandwidth p-i-n photodiode using asymmetric twin-waveguide technology", F. Xia, J. Wei, V. Menon, and S. R. Forrest, *IEEE Photon. Technol. Lett.*, **15**, 452 (2003).
2. "A fully integratable, 1.55 $\mu$ m wavelength, continuously tunable asymmetric twin-waveguide distributed Bragg reflector laser", H. Wang, C. Li and S. Forrest, *IEEE Photon. Technol. Lett.*, **15**, 1189 (2003).
3. "A Monolithically Integrated Long Wavelength Balanced Photodiode Using Asymmetric Twin Waveguide Technology", S. S. Agashe, S. Datta, F. Xia and S. R. Forrest, *IEEE Photon. Technol. Lett.*, **16** 236 (2004).
4. "A High Bandwidth Analog Heterodyne RF Optical Link with High Dynamic Range and Low Noise Figure", S. Datta, S. Agashe and S. R. Forrest, *IEEE Photon. Technol. Lett.*, **16**, 1733 (2004).
5. "Reduction of absorption loss in asymmetric twin waveguide laser tapers using argon plasma-enhanced quantum well intermixing", Y. Huang, F. Xia, V. M. Menon, S. R. Forrest, *IEEE Photon. Technol. Lett.*, **16**, 2221 (2004).
6. "Photonic integration using asymmetric twin-waveguide (ATG) technology. I. Concepts and theory", F. Xia, V. M. Menon, and S. R. Forrest, *IEEE J. Sel. Topics in Quant. Electron.*, **11**, 17 (2005)
7. "Photonic integration using asymmetric twin-waveguide (ATG) technology. II. Devices", V. M. Menon, F. Xia, and S. R. Forrest, *IEEE J. Sel. Topics in Quant. Electron.*, **11**, 30 (2005)
8. "A 16GHz Linear Analog Heterodyne RF Optical Link Employing a WIRNA Receiver", S. Datta and S. R. Forrest, *Photon. Technol. Lett.*, **17**, 890 (2005).

9. "A monolithically integrated optical heterodyne receiver", F. Xia, S. Datta, and S. R. Forrest, *IEEE Photon. Technol. Lett.*, **17**, 1716 (2005).

**(c) Papers published in non-peer-reviewed journals or in conference proceedings**

1. "Monolithic integration of a semiconductor optical amplifier (SOA) and a high-speed waveguide p-i-n photodiode using asymmetric twin-waveguide technology", F. Xia, V. Menon and S. R. Forrest, Opt. Fiber Commun. Conf. '03, Paper TuG, Atlanta (March 25, 2003).
2. "Monolithically Integrated Balanced Photodiode Using Asymmetric Twin Waveguide Technology", S. Agashe, S. Datta and S. R. Forrest, 15<sup>th</sup> Int'l. Conf on InP and Related Mat., Paper FA1.7, Santa Barbara (May, 2003).
3. "Photonic Integration Made Easy Using Asymmetric Twin Waveguide Technology", S. R. Forrest, V. Menon, F. Xia, invited, 2003 IEEE/LEOS Summer Top. Mtg., Vancouver (July 15, 2003).
4. "Optical analog heterodyne FM link using a monolithically integrated balanced photodiode and WIRNA receiver", S. Datta, S. Agashe, F. Xia, and S. R. Forrest, IEEE LEOS Ann. Mtg., Paper ThK 4, Tucson (Oct. 30, 2003).
5. "Asymmetric Twin Guide Technology: A Simple and Versatile Solution for Photonic Integration", V.M. Menon, F.Xia, W. Tong, S. Agashe, and S. R. Forrest, invited, Optical Fiber Commun. Conf., San Francisco (March, 2004).
6. "A WIRNA Receiver Architecture Based 16GHz Optical Analog Heterodyne FM Link", S. Datta and S. R. Forrest, *CLEO/QELS '05*, Paper CMH4, Baltimore (May, 2005)
7. "A Monolithically Integrated Optical Heterodyne Receiver", F. Xia, S. Datta and S. R. Forrest, *CLEO/QELS '05*, Paper CMGG2, Baltimore (May, 2005)

**(d) Papers presented at meetings, but not published in conference proceedings**

1. "Very low NF high DR heterodyne RF lightwave links using a simple, versatile photonic integration technology", S. R. Forrest, V. Menon, S. Agashe and S. Datta, GOMAC, Monterey, CA (2004).

2. “Photonic integration made easy using asymmetric twin waveguide technology”, S. Forrest, invited, 4<sup>th</sup> NSF-MEXT Symposium on Nanophotonics: Beyond the Limits of Optics, Tokyo (Oct. 25, 2004).
3. “Photonic Integrated Circuits for RF, Analog Links, WDM and Other Advanced Application based on Asymmetric Twin Waveguide Technology”, V. Menon, F. Xia, S. Agashe, S. Datta and S. R. Forrest, *Int. Photonics Res. and Apps.*, invited, San Diego (April, 2005).
4. “Photonic Integrated Circuits for Analog and Digital Optical Communications Systems”, S. R. Forrest, V. Menon, S. Agashe and S. Datta, *Conf. on Int. Photonics and Systems (CIPS)*, invited, Mass. Inst. Technol. (May, 2005).
5. “Photonic Integrated Circuits for Advanced Applications Based on Asymmetric Twin Waveguide Technology”, S. R. Forrest, keynote address, *CEATEC 2005*, Chiba, Japan (Oct., 2005).

**(2) “Scientific personnel” supported by this project [current address]**

Hongsheng Wang, PhD, 2003 [Alphion, Inc.]  
Fengnian Xia, PhD, 2005 [IBM Research Labs]  
Shubohashish Datta, PhD, 2005 [Lightspin Technologies]  
Shashank Agashe, PhD, 2006 [Infinera]  
Vinod Menon, post-doc [CUNY, Queens]

**(3) “Report of Inventions”**

U.S. Patent application entitled “Photonic Integrated Detector Having a Plurality of Asymmetric Waveguides”

**(4) “Scientific progress and accomplishments”**

The program goals were to demonstrate ultra-low noise RF links, and to demonstrate several key integrated optoelectronic components employing a versatile asymmetric twin waveguide technology. All objectives set forth in the proposal were either met or exceeded. These achievements included:

1. Demonstration of a versatile integration technology based on the asymmetric twin waveguide platform that allowed for the realization of a broad range of components useful in RF photonic components. This resulted in the demonstration of a fully integrated heterodyne receiver operating to 5 GHz, as well as balance photodiode/semiconductor optical amplifier pairs, and a wavelength tunable laser used as the local oscillator on the ATG platform.

2. Demonstration of the highest bandwidth heterodyne links operating at 5GHz and 16GHz. These links were based on phase modulation and represent an extremely high sensitivity route to analog optical transmission.
3. Paths to commercialization involve a close partnership Apogee Photonics, Inc., a start up from our group whose charter is to fabricate low cost photonic integrated circuits based on twin waveguide technology.

A detailed summary of our accomplishments are provided in the pages following this brief summary. All of the results have been published in very high prestige journals, including Photonics Technology Letters, the IEEE Journal of Quantum Electronics, and the IEEE Journal of Lightwave Technology.

#### **(5) “Technology transfer”**

ASIP, Inc., now Apogee Photonics is a NJ start-up company founded to commercialize ATG Photonic Integrated circuits. This company has worked closely with us to develop the ATG components and are now a successful company (possibly the largest domestic supplier of semiconductor lasers) based in Pennsylvania. They have licensed the concepts and have immediate plans to commercialize the components.

#### **Invention Disclosures:**

1. A Peer-to-Peer Architecture for Distributed Real-Time Gesture Recognition (12/20/2004)
2. Reduction of Absorption Loss in Asymmetric Twin Waveguide Lasers using Plasma-Enhanced Quantum Well Intermixing (05/26/2004)
3. Efficient Coupling of Light into Phontonic Bandgap devices using Asymetric Twin Guide (ATG) Tapered Mode Transformer (08/25/2002)

**A High Bandwidth Analog Heterodyne RF Optical Link with High Dynamic Range  
and Low Noise Figure**

S. Datta, S. Agashe and S. R. Forrest

*Department of Electrical Engineering, Center for Photonics and Optoelectronic*

*Materials (POEM) Princeton University,*

*Princeton, New Jersey, 08544, USA*

**Abstract**

We demonstrate a 1.55 $\mu\text{m}$  wavelength, 5 GHz analog heterodyne optical link with a noise figure of (20 $\pm$ 2) dB and spurious-free dynamic range of (102 $\pm$ 2) dB-Hz<sup>2/3</sup>. A wideband rectifier narrowband receiver architecture is employed to allow for phase noise cancellation. Advantages of using an integrated balanced photodiode pair and external modulation in the reduction of relative intensity noise and an increase in link linearity are experimentally demonstrated.

## I. INTRODUCTION

Analog optical links can be used for a variety of applications, including optically controlled phased array antennas [1] – [3], cable television distribution systems [4], and wireless communication networks [5]. High performance links using intensity modulated direct detection (IMDD) systems have been demonstrated both with and without external modulation of the signal laser [6], [7]. For example, a 1MHz link employing a linearized external modulator with a spurious-free dynamic range (SFDR) of 132 dB normalized to a bandwidth of 1Hz has been demonstrated [8]. A 130MHz direct detection link with a noise figure of 2.5dB has also been demonstrated [9]. However, coherent heterodyne optical links are more suitable for dense wavelength division multiplexed (WDM) applications where electronic RF filters can be used to effectively replace high quality factor optical filters for channel separation [4]. Moreover, IMDD links are limited by laser relative intensity noise (RIN) at high optical powers. In coherent links, balanced photodiodes (BPD) can be used to substantially reduce, or even eliminate RIN [10]. Also, coherent links allow the signal to be carried by the optical phase, giving rise to a superior noise performance than their amplitude modulated counterparts [11],[12]. Kalman and co-workers [12] predicted that a 1GHz heterodyne FM link can exhibit an SFDR of  $>110\text{dB}\cdot\text{Hz}^{2/3}$  when a laser with RIN of  $-130\text{ dB/Hz}$  and operating at 10mW is employed. Sabido, et al. improved upon their 1GHz link which had a dynamic range of  $88\text{dB}\cdot\text{Hz}^{2/3}$  [13] by using a cascaded linearized modulator to attain a 2GHz link with  $\text{SFDR} = 110\text{dB}\cdot\text{Hz}^{2/3}$  [14]. Phase noise cancellation (PNC) schemes in Ref. [15] – [18] are necessary in FM systems to overcome the degradation due to laser phase noise. A wideband rectifier narrowband amplifier (WIRNA) architecture [11], [15], [19] is an

effective solution for PNC owing to its simplicity. Analog FM heterodyne links using the WIRNA architecture have been reported to be limited in performance by phase-to-intensity (PTI) noise [19]. Here, an external modulator is used with the input laser to decrease the non-linearity of the link, thereby reducing the PTI noise. Advantages of using a BPD and external modulation in the reduction of RIN and in the linearization of the link are also experimentally demonstrated. A 1GHz directly modulated heterodyne FM optical link employing a single-ended detector with noise figure and SFDR of 57dB and 85dB-Hz<sup>2/3</sup>, respectively, has been previously demonstrated [15]. Here, a 1.55 $\mu$ m wavelength, 5 GHz analog heterodyne optical FM link with pre-emphasis is described. The link has a low noise figure of NF = (20 $\pm$ 2) dB and SFDR = (102 $\pm$ 2) dB-Hz<sup>2/3</sup>. For comparison, link performance in the present as well as previous work is summarized in Table 1.

## II. LINK DESCRIPTION

The externally modulated FM-WIRNA optical link is shown schematically in Fig. 1. Two continuous wave (CW),  $\lambda=1.55\mu\text{m}$  distributed feedback (DFB) lasers detuned by intermediate frequency (IF), are used as the transmitter and the local oscillator (LO). The transmitter output is modulated by inputting the RF signal directly into a phase modulator. The signal source in an FM link typically should be time integrated before being embedded in the phase. In our simplified FM link design, pre-emphasis was used to increase the signal-to-noise ratio (SNR) [20]. The differentiating pre-emphasis filter cancels the integrator, thereby reducing the number of components required, along with their associated insertion losses. Similarly at the receiver, the differentiating discriminator

is eliminated by the de-emphasis integrating filter. The modulator output is fed into the BPD through a polarization controller along with the LO output. The BPD eliminates the RIN of the two lasers along with other common mode terms, preserving only the mixed term comprised of the product of the LO and transmitter outputs. The photodiode output is passed through a bandpass filter that selects the IF peak and the lower frequency side lobe (Fig. 2(a)) as input to a Schottky diode that acts as a square law device (SLD). The SLD mixes the IF peak with the side lobe, and generates a signal at the baseband frequency. The baseband signal is selected by a narrowband filter, thereby producing the output signal. Figure 2(b) shows a 4GHz input signal (solid line) along with the corresponding outputs with the LO turned on (dashed line) and off (dotted line). The identical shapes of the input and the output with the LO is a result of phase noise cancellation (PNC) that occurs during mixing in the SLD. Moreover, the non-linear PNC circuit acts like a precise automatic frequency control. As a result, it is not necessary to accurately stabilize the two laser frequencies as long as the IF and the lower FM sidelobe are within the pass band of the IF amplifier. Also, the absence of any detectable output signal in the absence of the LO shows the lack of non-heterodyne terms. This is due to the low AM efficiency of the phase modulator as well as a good balance of the BPD. The direct modulation signal in Fig. 2(a) gives rise to the non-heterodyne term which should be compared to the product of the IF peak, the lower FM sidelobe, and the SLD efficiency that constitutes the heterodyne term.

### III. LINK ANALYSIS

#### III. A. Externally Modulated Link with BPD

For our FM heterodyne link [15], the electric fields of the modulated transmitter,  $e_S$ , and the LO,  $e_{LO}$ , are :

$$e_S(t) = \sqrt{2\eta P_S (1 + A_{PM} m(t))(1 + \xi_{RIN,S}(t))} \cos\left(2\pi f_S t + \frac{\pi R_{PM}}{V_\pi} m(t) + \Phi_S(t)\right) \hat{s} \quad (1)$$

$$e_{LO}(t) = \sqrt{2\eta P_{LO} (1 + \xi_{RIN,LO}(t))} \cos(2\pi f_{LO} t + \Phi_{LO}(t)) \hat{l} \quad (2)$$

where  $\eta$  is the optical mode impedance,  $P_S$  and  $P_{LO}$  are the transmitter and LO laser powers,  $A_{PM}$  is the amplitude modulation index per unit input current of the phase modulator,  $\xi_{RIN,S}$  and  $\xi_{RIN,LO}$  are the RIN fluctuations,  $f_S$  and  $f_{LO}$  are the signal and LO laser frequencies,  $R_{PM}$  is the input resistance of the modulator,  $V_\pi$  is the voltage bias required to produce a  $\pi$  phase shift in the phase modulator,  $m(t)$  is the RF input message signal current,  $\Phi_S$  and  $\Phi_{LO}$  are the transmitter and LO phase noises, and  $\hat{s}$  and  $\hat{l}$  are the electric field polarization vectors. Ideally,  $A_{PM}$  should be as small as possible. The output current,  $i_{BPD}$ , of the BPD is:

$$\begin{aligned} i_{BPD}(t) = & G_{INS} G_{MMI} \Re_{DET} \left( \frac{1 - b_{MMI}}{1 + b_{MMI}} \right) P_S A_{PM} m(t) + \\ & 2G_{INS} G_{MMI} \Re_{DET} \left( \frac{2\sqrt{b_{MMI}}}{1 + b_{MMI}} \right) \times \\ & \cos(\theta_{MMI}) \sqrt{P_{LO} P_S (1 + A_{PM} m(t)) r(t)} \cos\left(2\pi f_{IF} t + \frac{\pi R_{PM}}{V_\pi} m(t) + \Phi(t)\right) \hat{s} \cdot \hat{l} + n(t) \end{aligned} \quad (3)$$

where,

$$r(t) = (1 + \xi_{RIN,S}(t))(1 + \xi_{RIN,LO}(t)), \quad (4)$$

$$f_{IF} = f_S - f_{LO}, \quad (5)$$

$$\Phi(t) = \Phi_S(t) - \Phi_{LO}(t), \quad (6)$$

and  $n(t)$  is white noise current with spectral density, i.e. the noise power per unit bandwidth, given by :

$$N = 2eG_{INS}G_{MMI}\mathfrak{R}_{DET}(P_{LO} + P_S) + \frac{4k_B T}{R_L} + \left( G_{INS}G_{MMI}\mathfrak{R}_{DET} \left( \frac{1-b_{MMI}}{1+b_{MMI}} \right) \right)^2 \left( P_S^2 10^{RIN_S/10} + P_{LO}^2 10^{RIN_{LO}/10} \right) \quad (7)$$

Moreover,  $G_{INS}$  is the insertion loss in the various optical components including fiber-to-waveguide coupling losses,  $G_{MMI}$  is the optical power transfer ( $<1$ ) in the MMI,  $b_{MMI}$  is the ratio of the output optical powers from the two output waveguides in the MMI, and  $\theta_{MMI}$  is the relative phase from two output arms of the MMI when only one input arm is illuminated, thereby denoting its amplitude and phase balance. Also,  $\mathfrak{R}_{DET}$  is the responsivity of the individual diodes in the BPD,  $f_{IF}$  is the intermediate frequency of the link,  $e$  is the electron charge,  $k_B$  is the Boltzman's constant,  $T$  is the absolute temperature,  $R_L$  is the output load resistance of the BPD, and  $RIN_S$  and  $RIN_{LO}$  are the transmitter and LO laser RIN, respectively. The bandwidth of the BPD is assumed to be large enough to encompass a significant part of the signal. Ideally, for a balanced MMI,  $b_{MMI} = 1$  and  $\theta_{MMI} = 0$ . Also assuming that  $A_{PM} = 0$ , we get:

$$i_{BPD}(t) = 2G_{INS}G_{MMI}\mathfrak{R}_{DET}\sqrt{P_{LO}P_S}r(t) \cos\left(2\pi f_{IF}t + \frac{\pi R_{PM}}{V_\pi}m(t) + \Phi(t)\right) \hat{s} \cdot \hat{l} + n(t) \quad (8)$$

where the power spectral density of  $n(t)$  is now given by:

$$N = 2eG_{INS}G_{MMI}\mathfrak{R}_{DET}(P_{LO} + P_S) + \frac{4k_B T}{R_L} \quad (9)$$

In Eq. (9), the BPD dark current is assumed to be negligible compared to the photocurrent. Comparing Eqs. (3) and (8) we see that the direct detection signal term at the base band disappears if either the MMI is perfectly balanced ( $b_{MMI} = 1$  and  $\theta_{MMI} = 0$ ), or the phase modulator has zero amplitude modulation index ( $A_{PM} = 0$ ). In that case, only the sinusoidal heterodyne term contributes to  $i_{BPD}(t)$ . Furthermore, comparing Eqs. (7) and (9) we find a reduction in RIN due to the BPD. For narrow band FM, the output current  $i_{BPF}$  of the band pass filter (BPF) is given by:

$$i_{BPF} = 2G_{INS}G_{MMI}G_{BPF}\Re_{DET}\sqrt{P_{LO}P_S}r(t)\left(1 + \frac{\pi R_{PM}}{2V_\pi}\tilde{m}(t)\right)\cos(2\pi f_{IF}t + \Phi(t)) - G_{INS}G_{MMI}G_{BPF}\Re_{DET}\sqrt{P_{LO}P_S}r(t)\frac{\pi R_{PM}}{V_\pi}m(t)\sin(2\pi f_{IF}t + \Phi(t)) + n_{BPF}(t) \quad (10)$$

where  $\tilde{m}(t)$  is the Hilbert transform of  $m(t)$  and

$$n_{BPF}(t) = n(t) * h_{BPF}(t), \quad (11)$$

where  $h_{BPF}$  and  $G_{BPF}$  are the impulse function and gain of the band pass filter. Neglecting the higher order noise terms, the output of the SLD,  $i_{SLD}$ , is given by:

$$i_{SLD} = 2\Gamma_{SLD}G_{MMI}^2G_{BPF}^2\Re_{DET}^2P_{LO}P_S\left(1 + \frac{\pi R_{PM}}{V_\pi}\tilde{m}(t) + \left(\frac{\pi R_{PM}}{2V_\pi}\right)^2(m^2(t) + \tilde{m}^2(t))\right) + n_{SLD}(t) \quad (12)$$

where  $\Gamma_{SLD}$  is the SLD efficiency, and :

$$n_{SLD}(t) = 2\Gamma_{SLD}G_{INS}G_{MMI}G_{BPF}\Re_{DET}\sqrt{P_{LO}P_S}n_{BPF}(t)\cos(2\pi f_{IF}t + \Phi(t)) \quad (13)$$

The polarization states of the LO and the transmitter lasers are assumed to be identical. Here the phase noise in the message signal is cancelled due to mixing. Finally, the narrow band filter retains only the base band signal term. The output current,  $i_{OUT}$ , is given by:

$$i_{OUT} = 2\Gamma_{SLD}G_{NBF}G_{INS}^2G_{MMI}^2G_{BPF}^2\Re_{DET}^2P_{LO}P_S\frac{\pi R_{PM}}{V_\pi}\tilde{m}(t) + n_{OUT}(t) \quad (14)$$

where

$$n_{OUT}(t) = n_{SLD}(t) * h_{NBF}(t) \quad (15)$$

and  $G_{NBF}$  and  $h_{NBF}$  are the gain and the impulse function of the narrow band filter.

Assuming the link noise is dominated by thermal and shot noise, the noise power  $P_{Noise}$  in the signal band,  $\Delta f$ , across a load resistance  $R_L$  is:

$$P_{Noise} = 4\Gamma_{SLD}^2 G_{NBF}^2 G_{INS}^2 G_{MMI}^2 G_{BPF}^4 \mathfrak{R}_{DET}^2 P_{LO} P_S \Delta f (eG_{INS} G_{MMI} \mathfrak{R}_{DET} (P_{LO} + P_S) R_L + 2k_B T). \quad (16)$$

Hence, the RF power link gain,  $LG_{BPD}^{EXT}$ , is given by:

$$LG_{BPD}^{EXT} = \left( 2\Gamma_{SLD} G_{NBF} G_{INS}^2 G_{MMI}^2 G_{BPF}^2 \mathfrak{R}_{DET}^2 P_{LO} P_S \frac{\pi R_{PM}}{V_\pi} \right)^2 \quad (17)$$

The noise figure,  $NF_{BPD}^{EXT}$ , is the ratio of the input to the output SNR and hence is a measure by which the link degrades the SNR. Then:

$$\begin{aligned} NF_{BPD}^{EXT} &= \frac{P_{Noise}}{4LG_{BPD}^{EXT} k_B T \Delta f} + 1 \\ &= \left( 2G_{INS} G_{MMI} \mathfrak{R}_{DET} \frac{\pi R_{PM}}{V_\pi} \sqrt{P_{LO} P_S} \right)^{-2} \left[ 2 + \frac{eR_L G_{INS} G_{MMI} \mathfrak{R}_{DET} (P_{LO} + P_S)}{k_B T} \right] + 1 \end{aligned} \quad (18)$$

The expression for noise figure assumes that at the input, thermal noise dominates. Additional input noise will decrease the noise figure due to the resulting decrease in the contribution of the noise added by the link in the output noise.

Spurious free dynamic range (SFDR) is defined as the output SNR at which the third order terms are equal to the noise floor [11]. The link DR can be derived by expanding Eq. (8) to its third order terms and substituting the message,  $m(t)$ , and by a two tone input  $I_0(\cos(2\pi f_1 t) + \cos(2\pi f_2 t))$ . The third order inter-modulation terms are:

$$i_{OUT}^{IM} = -\frac{1}{2} G_{NBF} \Gamma_{SLD} G_{BPF}^2 G_{INS}^2 G_{MMI}^2 \mathfrak{R}_{DET}^2 P_{LO} P_S \left( \frac{\pi R_{PM}}{V_\pi} \right)^3 I_0^3 \times (\sin(2\pi(2f_1 - f_2)t) + \sin(2\pi(2f_2 - f_1)t)) \quad (19)$$

The SFDR is then:

$$SFDR_{BPD}^{EXT} = \left[ \frac{2k_B T}{R_L} \left( \frac{\pi R_{PM}}{V_\pi} \right)^2 NF_{BPD}^{EXT} \right]^{-2/3} \quad (20)$$

### III. B. Comparison of the Performance of Different Links for a Single Tone Input

The performance of an externally modulated link with a BPD is now compared with directly modulated links using a single ended photodiode (SPD). The photodiode output current in various cases for a single tone input  $m(t) = I_M \cos(2\pi f_M t)$  can highlight the differences between the BPD and SPD based links.

#### III. B. 1. Directly Modulated Link using a BPD

For a directly modulated link, the response with a BPD is:

$$i_{BPD}^{DIR}(t) = 2G_{INS} G_{MMI} \mathfrak{R}_{DET} \sqrt{P_{LO} P_S (1 + A_{DFB} I_M \cos(2\pi f_M t))} r(t) \times \cos(2\pi f_{IF} t + 2\pi k_{DFB} \Gamma_{DIFF} I_M \cos(2\pi f_M t) + \Phi(t)) \hat{s} \cdot \hat{l} + n_{BPD}^{DIR}(t) \quad (21)$$

and  $k_{DFB}$  and  $A_{DFB}$  are the FM and AM modulation indices of the transmitter DFB laser, respectively, and  $\Gamma_{DIFF}$  is the efficiency of the pre-emphasis differentiating filter. Here,  $n_{BPD}^{DIR}(t)$  is the white noise current whose spectral density is given by Eq. (9). The non-heterodyne term does not exist for a perfectly balanced detector, although the heterodyne term itself is a mixed AM and FM signal. The AM contribution can be removed by using an amplitude limiter that is implemented with an amplifier driven in saturation. However,

this non-linear circuit element inevitably increases the PTI noise introducing a roll-off of noise figure and SFDR of the link at high laser powers [15]. Hence, the amplitude limiter shall not be used in this link in following discussion. Also, the FM efficiencies of DFB lasers can be large, on the order of 1GHz/mA. Hence, an externally modulated link would need a modulator with low  $V_\pi$  (e.g.  $\sim 0.5$  V) to rival the link gain achieved by typical directly modulated links. Carrying on with the analysis similar to the externally modulated BPD link for directly modulated BPD link we get:

$$LG_{BPD}^{DIR} = \left( 4\pi k_{DFB} \Gamma_{DIFF} \Gamma_{SLD} G_{NBF} G_{INS}^2 G_{MMI}^2 G_{BPF}^2 \mathfrak{R}_{DET}^2 P_{LO} P_S \right)^2, \quad (22)$$

$$NF_{BPD}^{DIR} = \left( 4\pi k_{DFB} \Gamma_{DIFF} G_{INS} G_{MMI} \mathfrak{R}_{DET} \sqrt{P_{LO} P_S} \right)^{-2} \left[ 2 + \frac{eR_L G_{INS} G_{MMI} \mathfrak{R}_{DET} (P_{LO} + P_S)}{k_B T} \right] + 1 \quad (23)$$

and

$$SFDR_{BPD}^{DIR} = \left[ \frac{2k_B T}{R_L} (2\pi k_{DFB} \Gamma_{DIFF})^2 NF_{BPD}^{DIR} \right]^{-2/3}. \quad (24)$$

### III. B. 2. Externally Modulated Link using SPD

For an externally modulated link, the response with a SPD is:

$$i_{SPD}^{EXT}(t) = G_{INS} \mathfrak{R}_{DET} \sqrt{P_{LO} P_S} r(t) \cos \left( 2\pi f_{IF} t + \frac{\pi R_{PM}}{V_\pi} I_M \cos(2\pi f_M t) + \Phi(t) \right) \hat{s} \cdot \hat{l} + n_{SPD}^{EXT}(t) \quad (25)$$

The power spectral density of the white noise  $n_{SPD}^{EXT}(t)$  is given by:

$$N_{SPD}^{EXT} = eG_{INS} \mathfrak{R}_{DET} (P_{LO} + P_S) + \frac{4k_B T}{R_L} + G_{INS}^2 \mathfrak{R}_{DET}^2 \left( P_S^2 10^{RIN_S/10} + P_{LO}^2 10^{RIN_{LO}/10} \right) \quad (26)$$

The signal consists of a pure heterodyne FM term similar to a BPD-based link except that half the optical power from the MMI or 3-dB coupler is lost. This translates into a reduction in link gain by a factor of 16, all other system parameters being equal. The link gain is given by:

$$LG_{SPD}^{EXT} = \left( \frac{1}{2} \Gamma_{SLD} G_{NBF} G_{INS}^2 G_{BPF}^2 \mathfrak{R}_{DET}^2 P_{LO} P_S \frac{\pi R_{PM}}{V_\pi} \right)^2. \quad (27)$$

Also, the laser RIN is not reduced. In Eq. (25), DC terms are neglected since they are removed by the bandpass filter. The noise performance of the link is given by:

$$NF_{SPD}^{EXT} = 1 + \left( \frac{1}{2} G_{INS} \mathfrak{R}_{DET} \frac{\pi R_{PM}}{V_\pi} \sqrt{P_{LO} P_S} \right)^{-2} \times \left[ 2 + \frac{eR_L G_{INS} \mathfrak{R}_{DET} (P_{LO} + P_S)}{2k_B T} + \frac{eR_L (G_{INS} \mathfrak{R}_{DET})^2}{2k_B T} (P_{LO}^2 10^{RIN_{LO}/10} + P_S^2 10^{RIN_S/10}) \right] \quad (28)$$

and

$$SFDR_{SPD}^{EXT} = \left[ \frac{2k_B T}{R_L} \left( \frac{\pi R_{PM}}{V_\pi} \right)^2 NF_{SPD}^{EXT} \right]^{-2/3}. \quad (29)$$

### III. B. 3. *Directly Modulated Link using SPD*

Neglecting the DC terms, the detector output current shows a direct AM term besides the mixed AM/FM heterodyne term, viz.:

$$i_{SPD}^{DIR}(t) = \mathfrak{R}_{DET} \frac{P_s}{2} A_{DFB} I_M \cos(2\pi f_M t) + n_{SPD}^{DIR}(t) + \mathfrak{R}_{DET} \sqrt{P_{LO} P_S (1 + A_{DFB} I_M \cos(2\pi f_M t))} r(t) \cos(2\pi f_{IF} t + 2\pi k_{DFB} \Gamma_{DIFF} I_M \cos(2\pi f_M t) + \Phi(t)) \hat{s} \cdot \hat{l} \quad (30)$$

The power spectral density of the white noise  $n_{SPD}^{DIR}(t)$  is given Eq. (26).

### III. B. 4. *Externally Modulated BPD vs. SPD Links*

The calculated noise figures and dynamic ranges for various links using parameters given in Table 2 and Eqs. (18), (20), (23), (24), (28) and (29) are shown in Fig. 6, along with measurements for directly modulated BPD link. In the calculations, the phase-to-intensity noise has not been taken into account.

The BPD link (Fig. 6(a) dashed line) has a lower noise figure than the SPD link (Fig. 6(a) dotted line), especially at higher LO power where RIN, which is absent in a perfectly balanced BPD, dominates the noise of the latter system. Our measurement for the BPD link was limited by the noise floor of the RF spectrum analyzer for LO powers less than  $\sim 0$ dB. The real noise figure in this region is actually less than the measured values. At higher LO powers, the roll off seen in the measured noise figure is due to the phase-to-intensity noise which has not been taken into account in the calculations. As a result, the calculations inaccurately predict a low NF at LO powers  $> 3$ dBm.

### III. B. 5 *External Modulation vs. Direct Modulation in BPD Links*

The amplitude modulation indices of the DFB laser and the external modulator can be calculated from the non-heterodyne term at the detector output, i.e. the output of SPD based externally and directly modulated links with the LO turned off (see Eqs. (25) and (30), Figs. 7(a) and (b), insets) and are found to be  $\sim 1.1 \text{ A}^{-1}$  and  $< 0.06 \text{ A}^{-1}$ , respectively. The directly modulated link proposed by Taylor and Forrest [15] employs a SPD along with an amplitude limiter to eliminate the parasitic AM signal. However the non-linear limiter implemented by an amplifier operating at saturation introduces PTI noise. As a

result, the noise figure and SFDR rolled off at 57dB and 85dB-Hz<sup>2/3</sup> in that 1GHz link [15]. The theoretically calculated noise figures and dynamic ranges for externally modulated (dashed line) and directly modulated (solid line) links with a BPD are shown in Fig. 6. The SFDR of the directly and externally modulated links are the same, since the two differ only by their FM modulation indices. The dynamic range remains the same although the corresponding values of the maximum and minimum RF input powers change. However, the NF, which is inversely proportional to the link gain, depends inversely on the square of the FM modulation index.

Therefore, the calculations suggest that minimum noise at the highest gain is obtained by using a directly modulated link with a balanced detector, but without an amplitude limiter. The BPD eliminates the non-heterodyne AM signal along with the RIN, resulting in a mixed AM/FM heterodyne link. An externally modulated FM link employing a phase modulator with  $V_{\pi}=0.5\text{V}$  is also expected to result in a similar link gain and noise figure as the mixed AM/FM link.

#### IV. EXPERIMENTAL RESULTS

The linearity, bandwidth, balance, dark current and responsivity of the balanced photodetector pair have a direct impact on the gain, bandwidth and dynamic range of the link. For our link, the balanced photodiodes were monolithically integrated along with a 1:1 multi-mode interference (MMI) coupler using asymmetric twin-waveguide (ATG) technology [21], [22], and were mounted in an RF package. Monolithic integration of the two diodes ensures that they have a nearly identical responsivity and bandwidth, whereas integration of the photodiodes with a 1:1 MMI splitter ensures amplitude and phase

balance between the two diode outputs. The schematic diagram of the device, whose detailed fabrication and performance have been previously described [21], [22], is shown in the inset of Fig. 3. The BPD has a DC responsivity of 0.32 A/W and is linear to > 3dBm optical power (Fig. 3). It exhibits a balanced response to within 0.5dB (Fig. 3 inset) which translates to a common mode rejection ratio (CMRR) >34dB, (see Fig. 4 inset). The CMRR was measured by comparing non-heterodyne direct modulation terms of the output of the BPD with a similar single-ended photodiode. Finally, the BPD has a bandwidth of 15GHz (Fig. 4), setting the upper limit of the IF. This, in turn, limits the bandwidth of the system which should typically be less than one-third of the IF bandwidth for narrow-band FM signals. A dark current of 5 $\mu$ A is observed at 2V reverse bias.

The externally modulated link with the BPD was compared with directly modulated and SPD links. Unless otherwise mentioned, all other components and system parameters were kept constant to compare their performances with externally modulated links using a BPD. The SPD was a commercially available (ASIP, Inc., Somerset, NJ) 40GHz detector also based on ATG technology [23]. It had a linear responsivity of 1A/W up to >10dBm optical power, and a dark current of 1 $\mu$ A at 1.5V reverse bias.

The directly modulated links were not amplitude limited, and hence are not pure FM heterodyne links. The transmitter and the LO laser powers in all four links were 0dBm and 3dBm, respectively. The lasers were commercial DFB laser modules with FM efficiencies of 1.4GHz/mA and RIN of -140dB/Hz. The LO and transmitter lasers were detuned by an IF of  $f_{IF}$  =14GHz. The LiNbO<sub>3</sub> phase modulator had  $V_{\pi}$ =5.6V, and was operated at a DC offset of 2.8V. The bandpass filter amplifier had a gain of 27dB and a

pass band between 6GHz and 15GHz. The narrowband filter retained the baseband terms and rejected all frequencies above 6GHz.

Figure 5 shows the response of the various links at different received optical powers and frequencies. The directly modulated link with the SPD is not considered here because it had a significant non-heterodyne AM term. A measured noise figure of  $(20\pm 2)$  dB (Fig. 6(a)) and an SFDR of  $(102\pm 2)$  dB-Hz<sup>2/3</sup> (Fig. 6(b)) was achieved for the directly modulated link with the BPD. The noise figure rolls off at LO powers  $>3$ dBm. For LO powers less than 0dB, we were limited at low signal powers by the noise floor of the spectrum analyzer at -95dBm. As a result, the lower error bar varies inversely as the LO power Fig. 6(a). This link (Fig. 5(c)) has a 1dB compression point above 10dBm input RF power.

Comparing Eqs. (9) with (26), we observe that the BPD reduces the RIN of the LO and transmitter laser. The existence of laser RIN can be observed by comparing the noise floor of the output signal with and without the LO turned on (Fig. 7(a)). This discrepancy was not observed for lower optical powers, as we were limited by the noise floor of the spectrum analyzer. For links using direct modulation, the non-heterodyne contribution to the output is observed by turning off the LO (Fig. 7(b)). Lack of the non-heterodyne term for the BPD-based link shows a nearly 1:1 balance (see Sec. II. B). Comparing Fig. 5(a) and 5(b), we observe that the BPD link has 10dB less link gain than that with the SPD. The link gain varies as the fourth power of the detector responsivity, see Eq. (17). The measured responsivities of the BPD and SPD are 0.34A/W and 1A/W, respectively, and since the SPD detects only half the optical power, we expect the BPD link to have 6.7dB less link gain than with the SPD. The remaining discrepancy of 3.3 dB

link gain for the case of the BPD can be explained by the  $\sim 20\%$  variation of coupling efficiency between the lensed fiber and the unpackaged integrated BPD fiber waveguides when switching setups for responsivity [21], [22] and the link measurements. In contrast, the coupling efficiency, and hence the responsivity, of the packaged SPD was stable.

The gain of the externally modulated link suffers a reduction of approximately 25dB as compared to the directly modulated case (see Fig. 5 (a) and (c)). Comparing Eqs. (17) and (27), the link gain of the externally modulated link is expected to be 21dB less than for direct modulation. The discrepancy of 4dB could also be a result from  $\sim 20\%$  variation in fiber-to-waveguide coupling efficiency of the BPD. Using a phase modulator with  $V_\pi=0.5V$  will increase the link gain by 21dB. Reduced link power also increases the noise figure (Eq. 18) in case of external modulation.

The frequency response of the link (Fig. 8(a)) is limited by that of the SLD whose transfer function is shown in Fig. 8(b). A two-tone signal was input into the SLD, and the output was measured as the frequencies of the tones were varied. The frequency offset, or the IF between the two tones, was kept constant at 14GHz, as in the link. The response shows a 6dB drop in SLD efficiency as frequency increases from 4GHz to 6GHz. Increasing the magnitude and the uniformity of the SLD response should lead to improvements in both the link gain and bandwidth. Also, as the BPD and the phase modulator are linear across the range of operation, the SLD is the only significant non-linear element in the link. However, unlike the amplitude limiter [15], it is an indispensable component of the WIRNA receiver. Hence, the roll-off in NF and dynamic range in Fig. 6 is ultimately limited by PTI noise introduced by the non-linearity of the SLD.

## V. CONCLUSION

A comparison of the present result along with the previous link achievements are mentioned in Table 1. It is possible to achieve low noise figure for links operating at lower frequencies [7] - [9] where electronic linearization [8] and impedance matching [9] are easier to implement than at higher frequencies. Moreover, noise figure is proportional to the square of the operating frequency [19]. Cox, et al. have observed that NF increases from 6dB to 33dB as the operating frequency of the link was increased from 22MHz to 1GHz [7]. We have achieved lower NF and higher or comparable SFDR when compared with previous 1-2GHz analog heterodyne FM [15] and AM [13], [14] links. This is due to a combination of having less non-linearity in the system, as well as having a balanced detector that remains linear up to 3dBm optical power. This allows us to operate at high optical powers without encountering a roll-off in noise performance due to phase-to-intensity noise [15].

A simple 5GHz optical heterodyne analog FM link operating at  $\lambda=1.55\mu\text{m}$  with pre-emphasis has been demonstrated. A monolithically integrated BPD was used to reduce the RIN of the local oscillator laser while a WIRNA receiver architecture was employed for phase noise cancellation. Use of an external phase modulator allows for high link linearity by eliminating the need for an amplitude limiter. The link was compared with those having direct detection and single photodiode. A directly modulated mixed AM/FM link employing a BPD is shown to have maximum gain and optimal noise performance with a SFDR =  $(102\pm 2)$  dB-Hz<sup>2/3</sup> and a noise figure =  $(20\pm 2)$  dB. The

limitation of the link frequency response and linearity due the square law device was also investigated.

#### ACKNOWLEDGEMENTS

The authors thank DARPA RFLICs program for funding, and we especially thank the late Dr. William Schneider for encouragement and support. We also thank Joseph DePhillipo, Nagul Sooriar, Dr. Dan Meerovich, Bill Mordarski and Dr. Millind Gokhale at ASIP Inc., Somerset, NJ, for packaging the BPD used in the link, as well as providing a packaged SPD.

## Captions

**Figure 1:** Block diagram of externally modulated analog heterodyne FM link with pre-emphasis.

**Figure 2:** (a) Input of the link in Fig. 1 through a 30dB attenuator (solid) has the same shape as the link output with LO on (dashed) showing phase noise cancellation. Output with LO off (dotted) has no discernable non-heterodyne term due small amplitude modulation efficiency of the phase modulator and a good CMRR of the BPD. (b) Bandpass IF amplifier output showing the IF peak at 14GHz and FM side lobes for 4GHz signal shown in (a).

**Figure 3:** DC responsivity curve of the BPD exhibits a responsivity of 0.34 A/W, linearity up to >3dBm optical power and balance (Inset) within 0.5dB. (Inset) Schematic of the monolithically integrated BPD with MMI device.

**Figure 4:** Frequency response of the BPD showing a bandwidth of 15GHz. (Inset) CMRR of the BPD is >34dB.

**Figure 5:** Link response for externally modulated BPD link (a), externally modulated SPD link (b) and directly modulated BPD link (c) at different frequencies. The solid lines are guides to the eye. Error of  $\pm 1$ dB in output power can be expected.

**Figure 6:** Measured noise figure (a) and SFDR (b) for directly modulated link with BPD as a function of LO power. Calculated noise figure (a) and SFDR (b) for directly and externally modulated links with BPD and externally modulated link with SPD neglect phase to intensity noise.

**Figure 7:** Link outputs with and without LO for externally/directly modulated with BPD/SPD exhibit RIN reduction by BPD and non-heterodyne term reduction by both BPD and external modulator.

**Figure 8:** Frequency response of the externally modulated link with BPD (a) limited by that of SLD (b). The solid lines are guides to the eye. Error of  $\pm 1$ dB in output power can be expected.

**Table 1:** Summary of performance achieved in optical analog links.

<b>Link Description</b>	<b>Frequency (GHz)</b>	<b>NF (dB)</b>	<b>SFDR (dB-Hz<sup>2/3</sup>)</b>
This Work	5	20	102
Direct Detection [7]	1	33	91
Direct Detection [9]	0.13	2.5	–
Heterodyne AM with SPD [13]	1	78	88
Heterodyne AM with Cascaded Modulator [14]	2	–	115
Heterodyne FM with Amplitude Limiter [15]	1	57	85

**Table 2:** Link parameters used for the NF and the SFDR calculations.

Parameter	Value
Signal Laser Power ( $P_S$ )	0dBm
$V_\pi$ of Phase Modulator	5.6V
Phase Modulator Input Resistance ( $R_{PM}$ )	$50\Omega$
Load Resistance ( $R_L$ )	$50\Omega$
BPD Fiber-to-Detector Responsivity ( $R_{BPD}$ )	0.34A/W
SPD Fiber-to-Detector Responsivity ( $R_{SPD}$ )	1A/W
Tx and LO Laser RIN	-140dB/Hz

## References

- [1] R. Taylor and S. R. Forrest, "Steering of an optically driven true-time delay phased-array antenna based on a broad-band coherent WDM architecture", *IEEE Photon. Technol. Lett.*, vol. 10, pp. 144-146, 1997.
- [2] P. M. Freitag and S. R. Forrest, "A coherent optically controlled phased array antenna system", *IEEE Microwave Guided Wave Lett.*, vol. 3, no. 9, pp. 293-295, 1993.
- [3] M. R. Surette, D. R. Hjelme, and A. R. Mickelson, "An optically driven phased array antenna utilizing heterodyne techniques", *J. of Lightwave Technol.*, vol. 11, pp. 1500-1509, 1995.
- [4] R. Olshansky, R. Gross, and M. Schimdt, "Subcarrier multiplexed coherent lightwave system for video distribution", *IEEE J. of Select. Areas Commun.*, vol. 8, no. 7, pp. 1268-1275, 1990.
- [5] O. Tonguz and H. Jung, "Personal communications access networks using sub-carrier multiplexed optical links", *J. of Lightwave Technol.*, vol. 14, pp. 1400-1408, 1996.
- [6] E. I. Ackerman and C. H. Cox, "RF fiber-optic link performance", *IEEE Microwave Magazine*, vol. 2, no. 4, pp. 50-58, 2001.
- [7] C. H. Cox, G. E. Betts and L. M. Johnson, "An analytic and experimental comparison of direct and external modulation in analog fiber-optic links", *IEEE Trans. Microwave Theory Tech.*, vol. 38, no. 5, pp. 501-509, 1990.
- [8] G. E. Betts, "Linearized modulator for suboctave bandpass optical analog links", *IEEE Trans. Microwave Theory Tech.*, vol. 42, no. 12, pp. 2642-2649, 1994.

- [9] E. I. Ackerman, C. Cox, G. Betts, et al, "Input impedance conditions for minimizing the noise figure of an analog optical link", *IEEE Trans. Microwave Theory Tech.*, vol. 46, no. 12, pp. 2025-2031, 1998.
- [10] *Fiber-Optic Communication Systems*, G. P. Agrawal, John Wiley and Sons, 3<sup>rd</sup> edition, 2002.
- [11] R. F. Kalman, J. C. Fan and L. G. Kazovsky, "Dynamic range of coherent analog fiber-optic links", *J. Lightwave Technol.*, vol. 12, no. 7, pp. 1263-1277, 1994.
- [12] R. F. Kalman, J. C. Fan and L. G. Kazovsky, "A novel analog optical link with high dynamic range", *IEEE Photon. Technol. Lett.*, vol. 5, no. 6, pp. 725-728, 1993.
- [13] D. J. Sabido, M. Tabara, T. Fong, R. F. Kalman and L. G. Kazovsky, "Experimental Linewidth-Insensitive Coherent Analog Optical Link", *J. Lightwave Technol.*, vol. 12, no. 11, pp. 1976-1985, 1994.
- [14] D. J. Sabido, M. Tabara, T. K. Fong, C. L. Lu and L. G. Kazovsky, "Improving the dynamic range of a coherent analog AM optical link using a cascaded linearized modulator", *IEEE Photon. Technol. Lett.*, vol. 7, no. 7, pp. 813 – 815, 1995.
- [15] R. Taylor and S. R. Forrest, "Optically coherent direct modulated FM analog link with phase noise canceling circuit", *J. Lightwave Technol.*, vol. 17, no. 4, pp. 556-563, 1999.
- [16] R. Bondurant, D. Welford, S. B. Alexander and V. W. S. Chan, "Frequency noise cancellation in semiconductor lasers by nonlinear heterodyne detection", *Opt. Lett.*, vol. 11, pp. 791-793, 1986.

- [17] R. Gross, R. Olshansky and M. Schmidt, "Coherent FM-SCM system using DFB lasers and a phase noise cancellation circuit", *IEEE Photon. Technol. Lett.*, vol. 2, pp. 66-68, 1990.
- [18] W. Kwong, P. Prucnal and M. Teich, "Coherent subcarrier fiber-optic communication systems with phase-noise cancellation", *IEEE Trans. Comm.*, vol. 42, no. 6, 1994.
- [19] R. Taylor, H. V. Poor and S. R. Forrest, "Phase noise in coherent analog AM-WIRNA optical links", *J. Lightwave Technol.*, vol. 15, no. 4, pp. 565-575, 1997.
- [20] B. P. Lathi, *Modern Digital and Analog Communication Systems*, Orlando: Hold, Rinehart and Winston, 2<sup>nd</sup> edition, 1989.
- [21] S. S. Agashe, S. Datta, F. Xia and S. R. Forrest, "Monolithically Integrated Balanced Photodiode using Asymmetric Twin-Waveguide Technology", *Proc. of the 15th Indium Phosphide and Related Materials Conf.*, 2003, pp. 513-515.
- [22] S. S. Agashe, S. Datta, F. Xia and S. R. Forrest, "A Monolithically Integrated Long-Wavelength Balanced Photodiode using Asymmetric Twin-Waveguide Technology", *IEEE Photon. Technol. Lett.*, accepted for Jan 2004.
- [23] F. Xia, J. K. Thomson, M. R. Gokhale, P. V. Studenkov, J. Wei, W. Lin and S. R. Forrest, "An asymmetric twin-waveguide high-bandwidth photodiode using a lateral taper coupler", *IEEE Photon. Technol. Lett.*, vol. 13, no. 8, pp. 845-847, Aug. 2001.

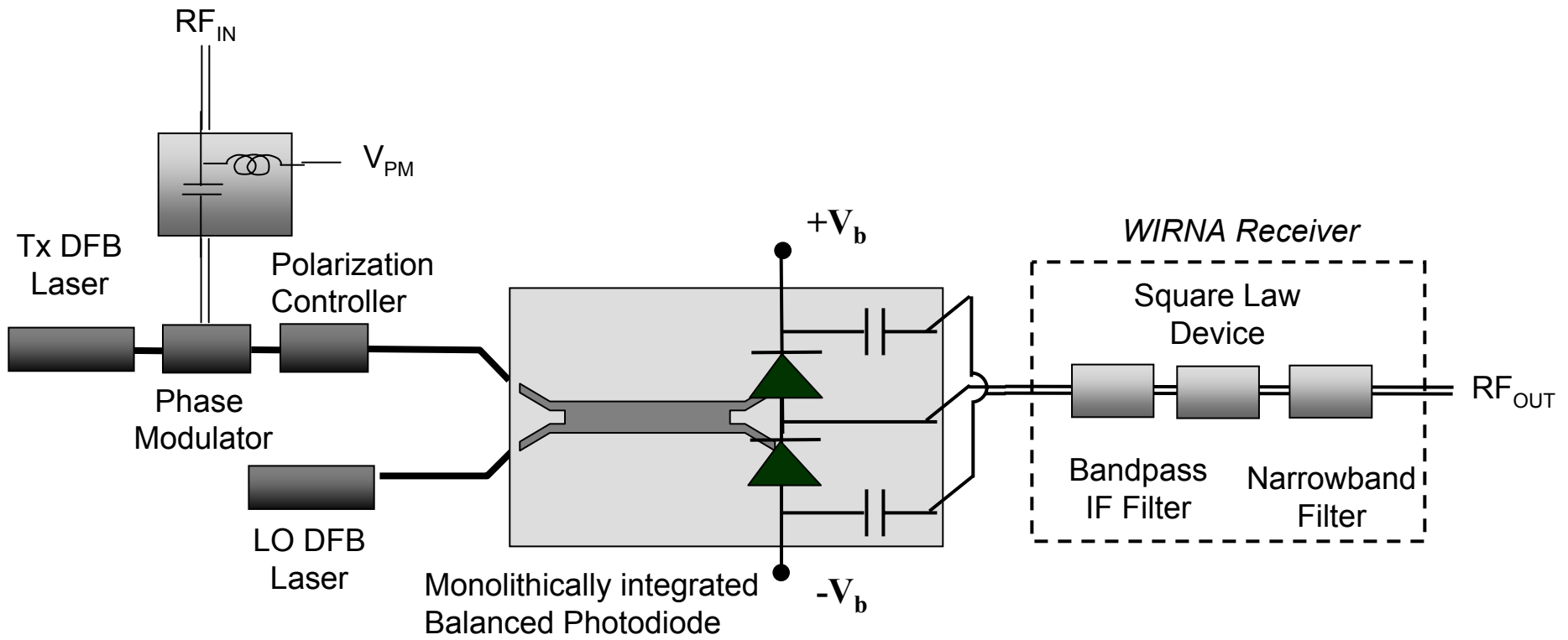


Fig. 1, Datta, et al.

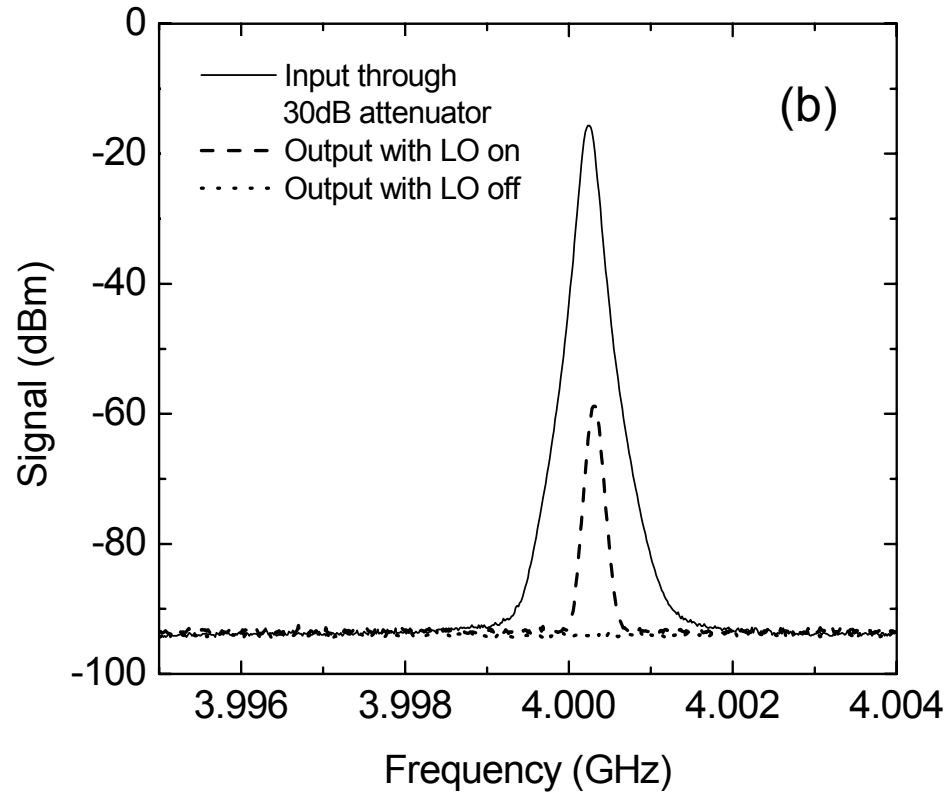
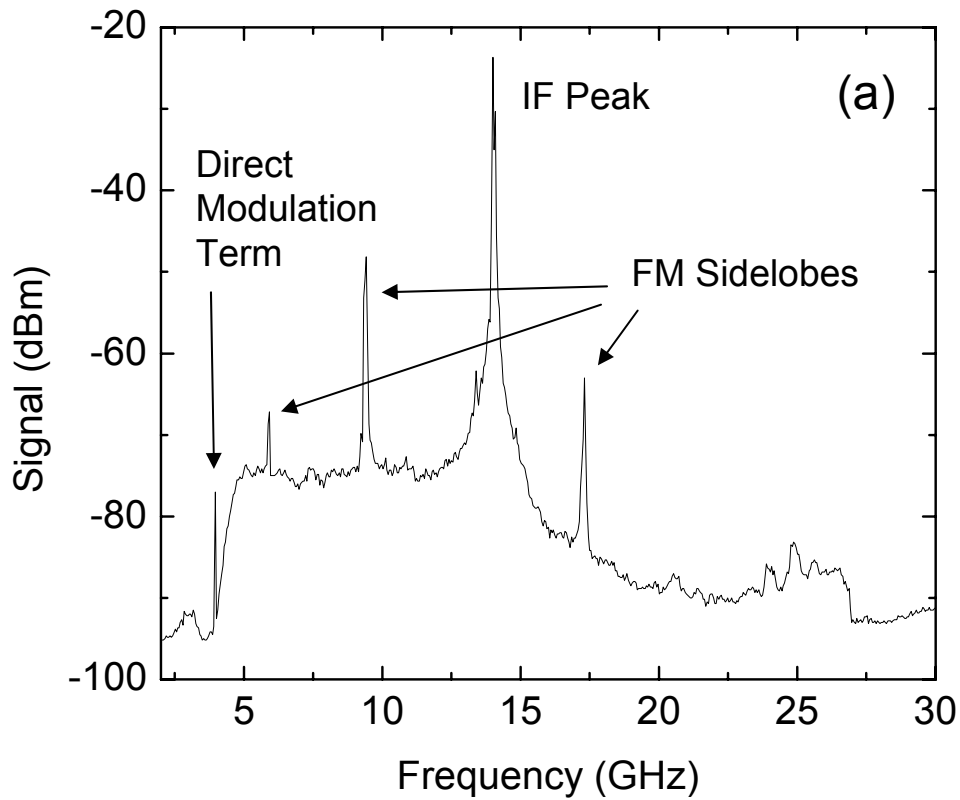


Fig. 2, Datta, et al.

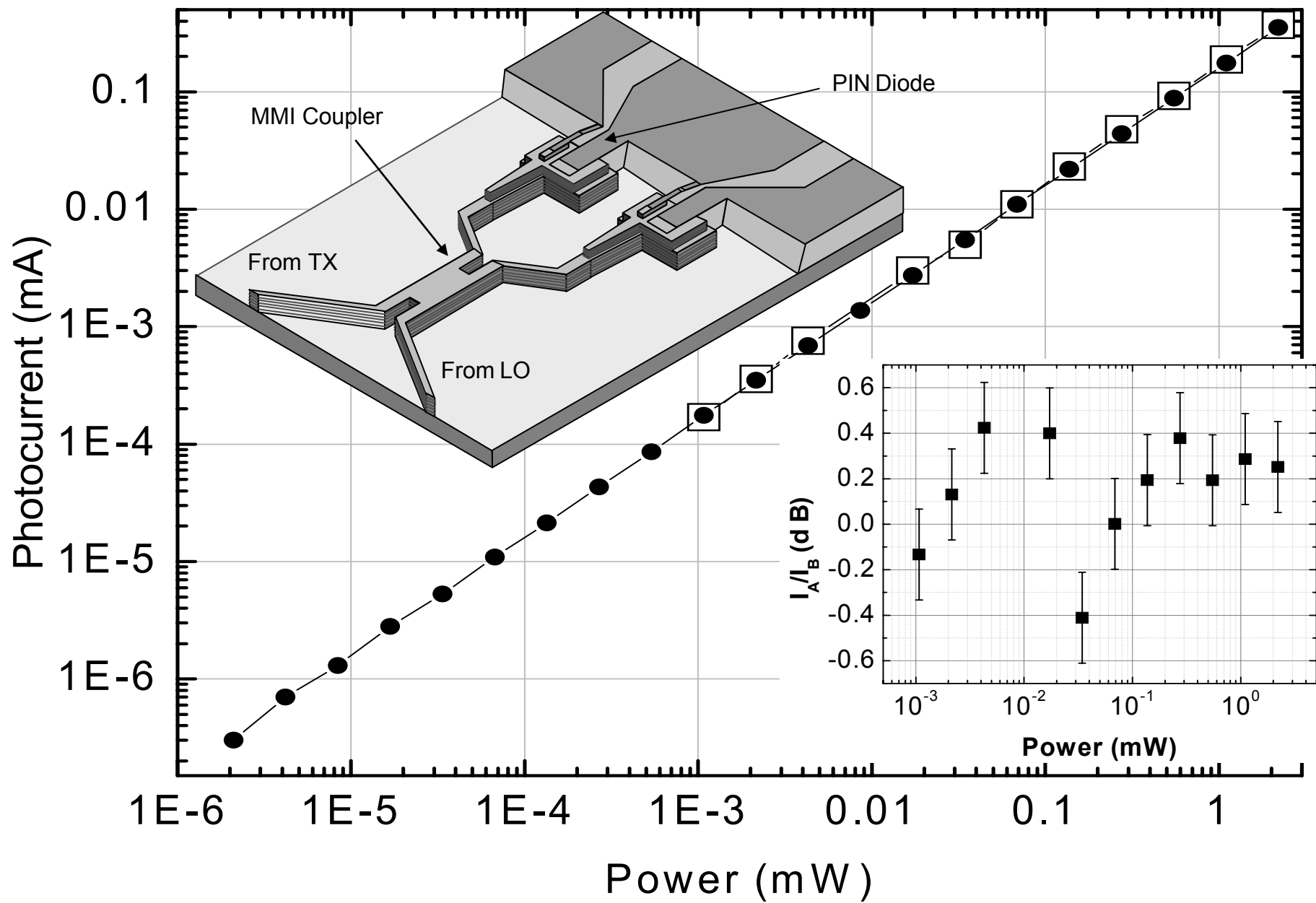


Fig. 3, Datta, et al.

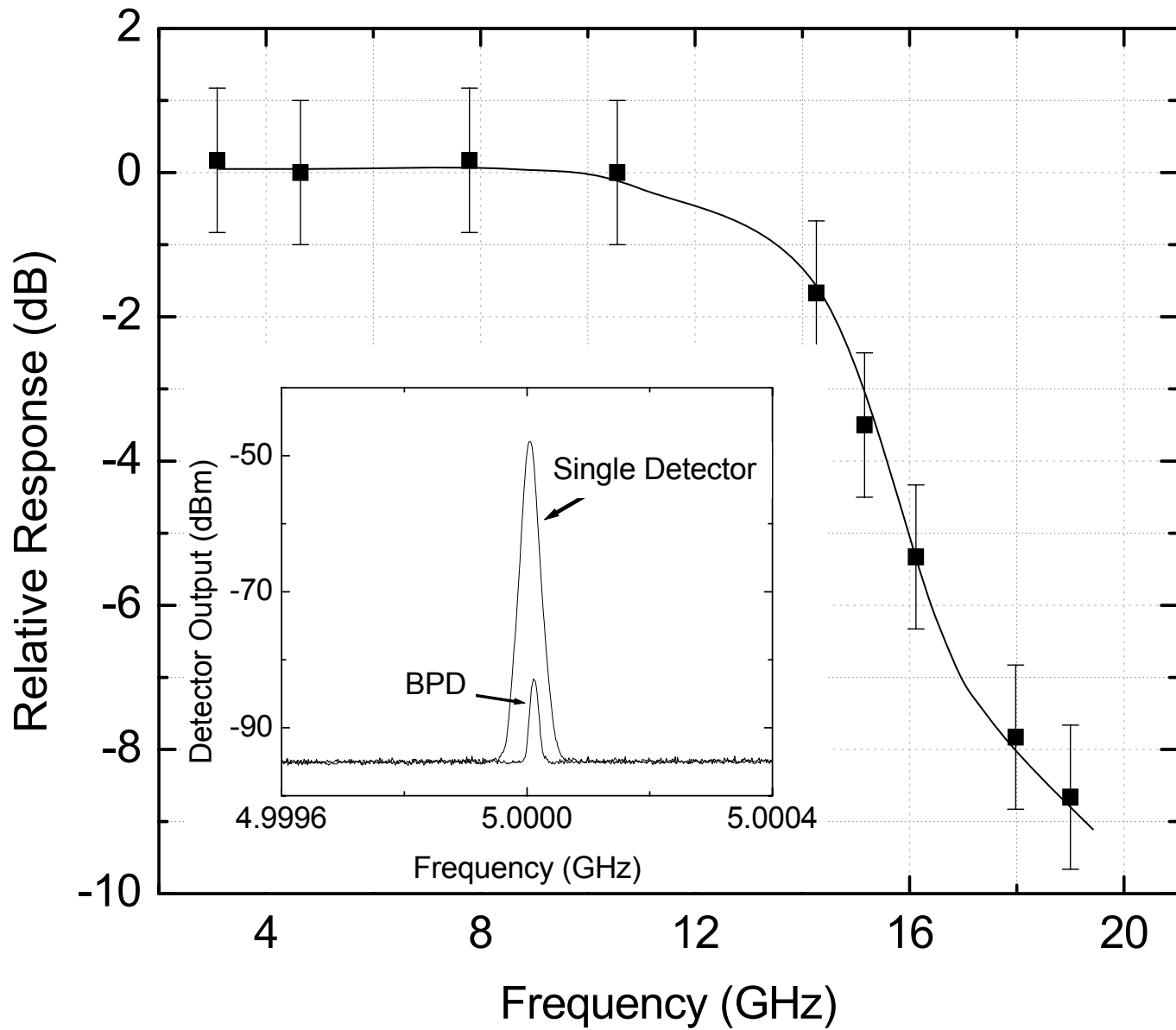


Fig. 4, Datta, et al.

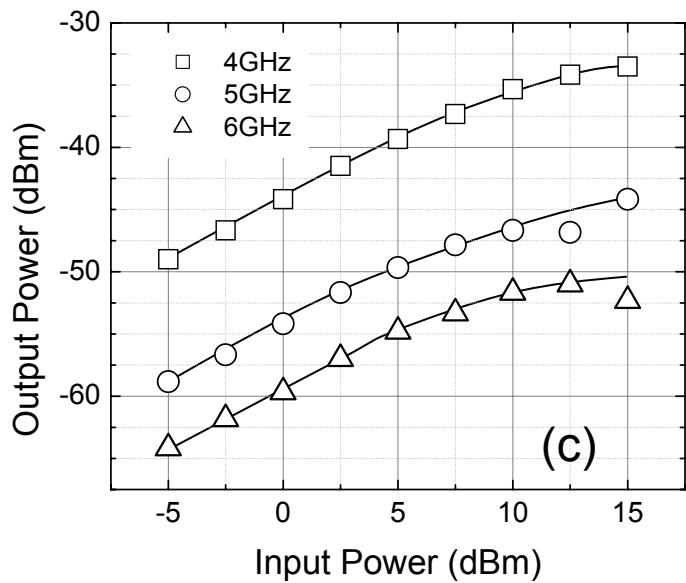
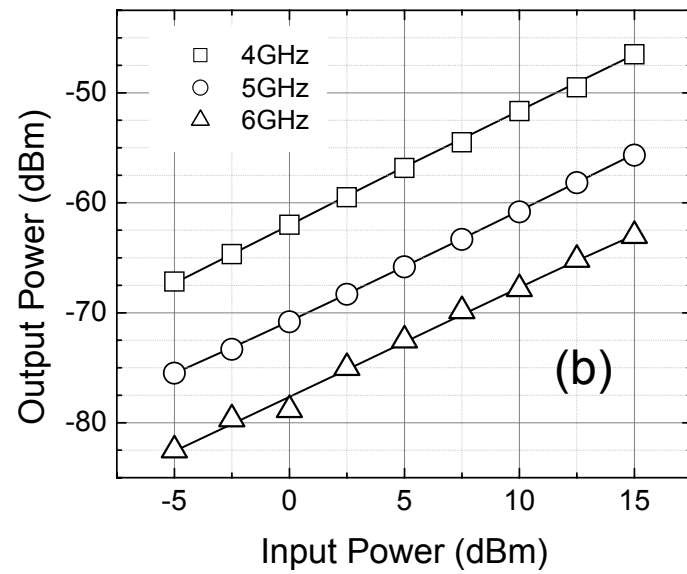
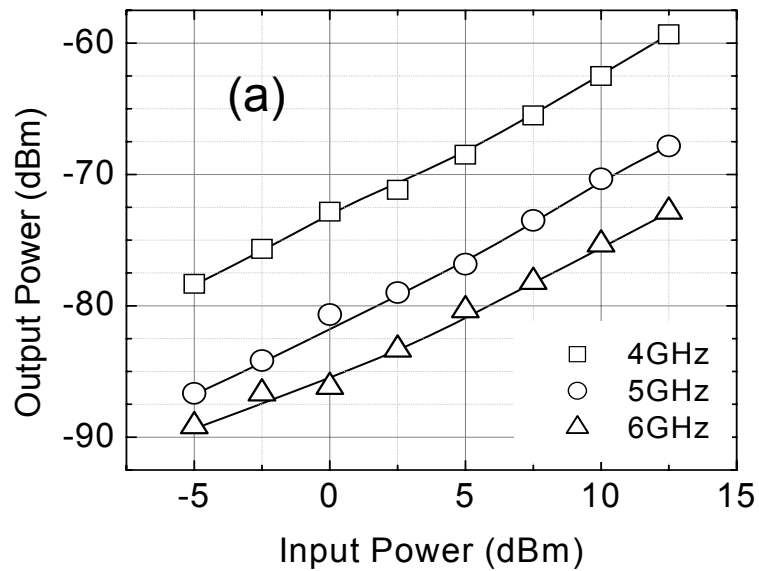


Fig. 5, Datta, et al.

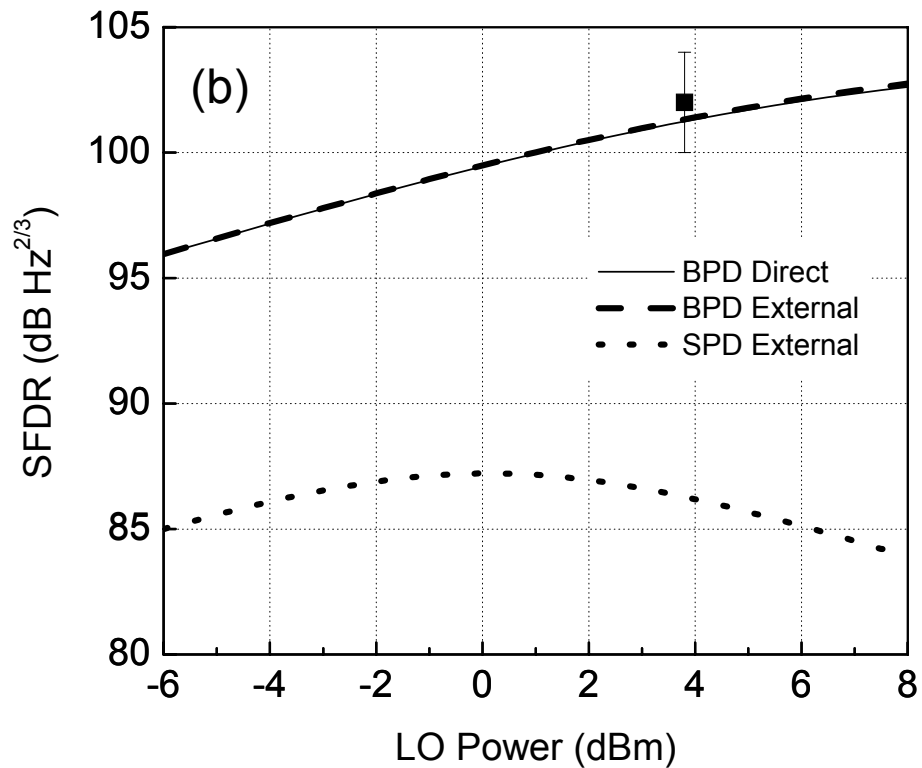
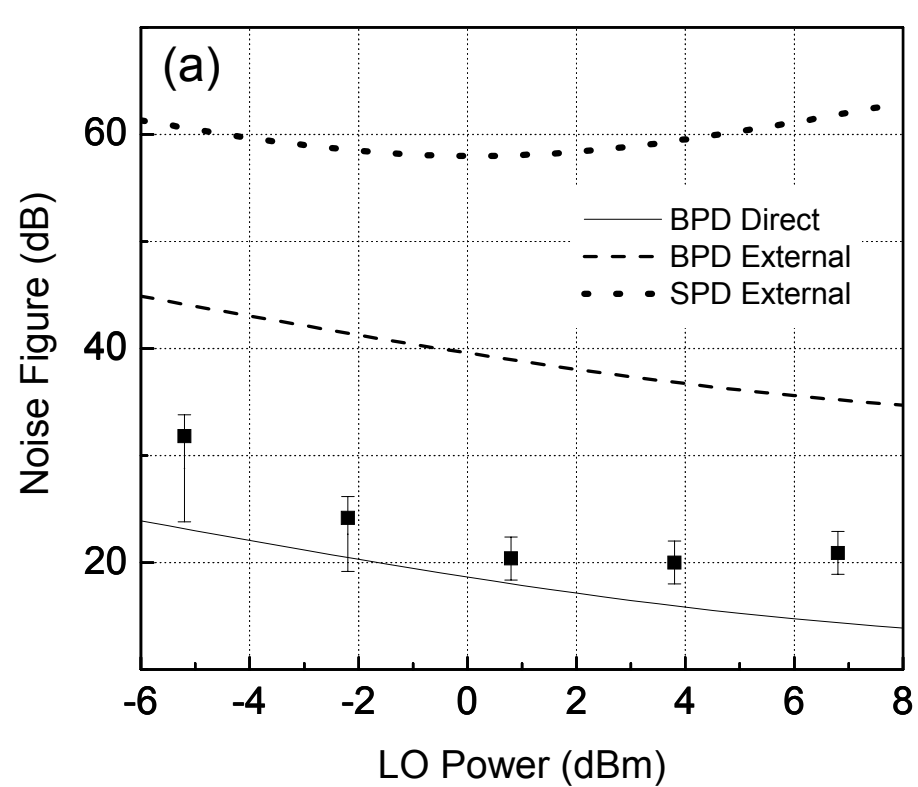


Fig. 6, Datta, et al.

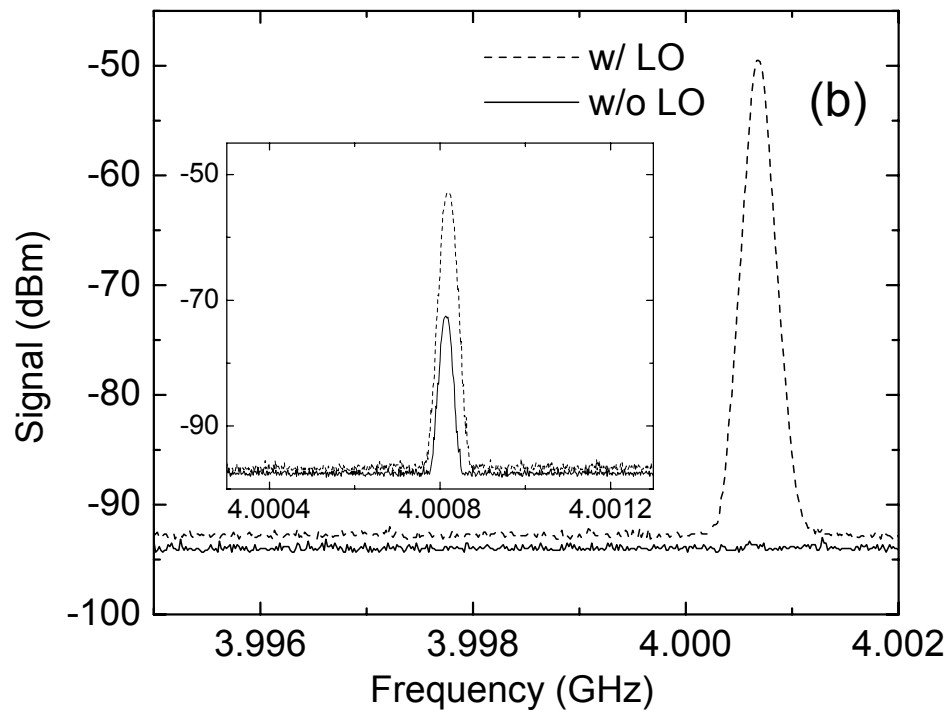
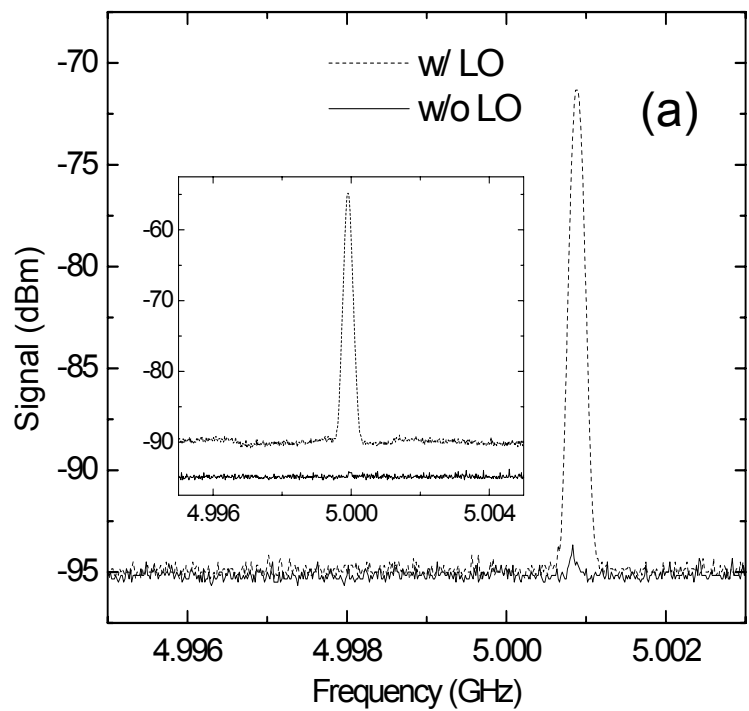


Fig. 7, Datta, et al.

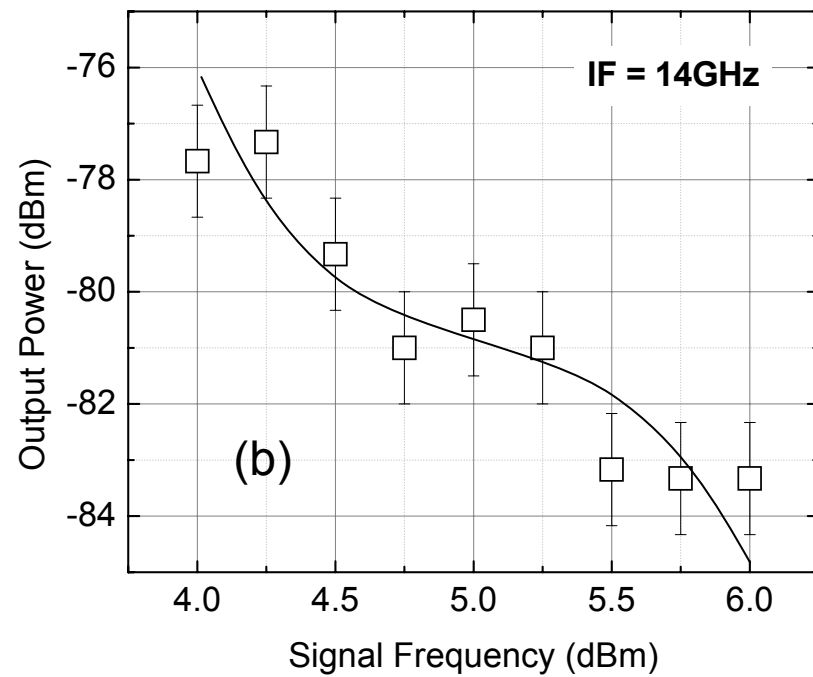
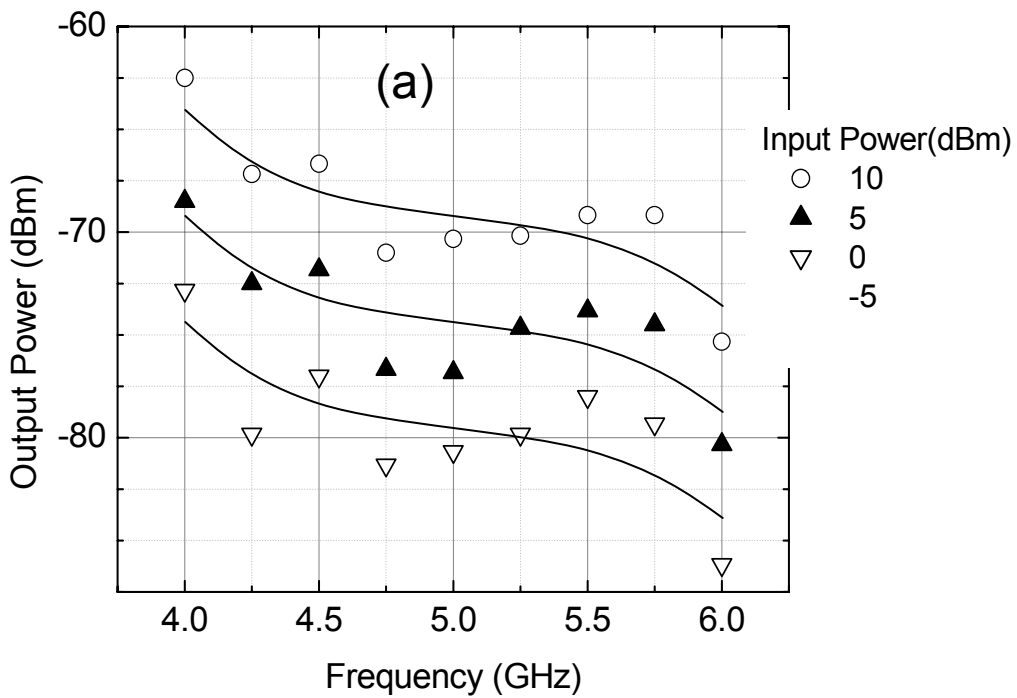


Fig. 8, Datta, et al.

# **A 16GHz Linear Analog Heterodyne RF Optical Link Employing a WIRNA Receiver**

S. Datta and S. R. Forrest

*Department of Electrical Engineering,*

*Princeton University,*

*Princeton, New Jersey, 08544, USA*

## **Abstract**

We demonstrate a 16 GHz analog heterodyne optical link operating at 1.55  $\mu\text{m}$  wavelength with a noise figure of  $(40\pm 1)$  dB and spurious-free dynamic range of  $(108\pm 2)$  dB-Hz<sup>2/3</sup>. The wideband rectifier narrowband amplifier (WIRNA) receiver architecture is employed with improvements over previous work to minimize the number of components in the link. The link performance is compared with that of an intensity modulated direct detection link. We show that further improvements in noise figure can be realized using balanced photodetector receivers. To our knowledge, this is the highest reported bandwidth of a broadband linear analog optical link reported to date, and shows the advantages of employing heterodyne versus direct detection for such applications.

Analog optical links are suitable for a range of applications such as optically controlled phased array antennas [1], cable television distribution [2], and wireless communication [3]. High performance links using intensity modulated direct detection (IMDD) systems have been demonstrated both with and without external modulation of the signal laser [4-8]. However, coherent heterodyne optical links are more suitable for dense wavelength division multiplexed applications where electronic RF filters can be used to replace optical filters for channel separation [2]. Moreover, IMDD links are limited by laser relative intensity noise (RIN) at high optical power levels. In contrast, balanced photodiodes (BPDs) used in coherent links can be used to substantially reduce, or even eliminate RIN [9]. Also, coherent links allow the signal to be carried by the optical phase, resulting in noise performance superior to their amplitude modulated counterparts [10-13].

Phase noise cancellation (PNC) schemes [14, 15] are necessary in FM systems to overcome the degradation due to laser phase noise. A wideband rectifier narrowband amplifier (WIRNA) receiver architecture [10, 14, 16, 17] is a simple and effective solution for achieving PNC. Previously, a 5GHz analog FM heterodyne link with  $NF = (20 \pm 1)$  dB and  $SFDR = (102 \pm 2)$  dB-Hz<sup>2/3</sup> was demonstrated using the WIRNA architecture, and was compared with previous achievements in IMDD and coherent systems [17]. However, there is a need for higher frequency RF links operating in the Ku-band (11 – 18GHz) for spectroscopy [18], satellite communication [19] and radar systems [20]. Optical links provide an alternative to conventional direct detection links in these applications [4] since they enable high bandwidth analog-to-digital conversion, along with fast signal processing.

An inherent limitation of high frequency optical links is the need for a square law device (SLD) that must operate at an intermediate frequency (IF) that is at least two to three times the operating frequency of the link. In this work, we propose and demonstrate a high frequency heterodyne link that eliminates the need for the SLD [17]. The 16GHz heterodyne link operating at 1.55  $\mu\text{m}$  wavelength has  $\text{NF} = (40 \pm 1)$  dB and  $\text{SFDR} = (108 \pm 2)$  dB-Hz<sup>2/3</sup>. Moreover, the link is externally modulated, which is essential for high frequency operation. A single photodiode is used in contrast to the link demonstrated in Ref. [17] that employed an integrated balanced photodiode [21]. Possible performance improvements with the use of a BPD are discussed. To our knowledge, this is the highest frequency analog optical link reported to date.

The FM-WIRNA link is shown schematically in Fig. 1(a). Two continuous wave (CW),  $\lambda=1.55\mu\text{m}$  distributed feedback (DFB) lasers, detuned by the intermediate frequency,  $f_{\text{IF}} = 40\text{GHz}$ , are used as the transmitter and the local oscillator (LO) sources. The laser modules exhibited a relative intensity noise of  $\text{RIN}=-140\text{dB/Hz}$ . The transmitter and LO were operated at 1.5mW and 4mW CW, respectively, unless otherwise noted. The transmitter output is externally modulated with the RF input using a 20GHz phase modulator with  $V_{\pi} = 6\text{V}$ . This configuration is similar to the FM system with pre-emphasis described in [17]. This configuration improves the noise performance of the FM link by moving the differentiating discriminator from the receiver output to the input as a pre-emphasis filter [22]. Normally, a FM link would require the RF input to pass through an integrator before being modulated on the optical phase. The integrator is cancelled by the differentiating pre-emphasis filter [17], thereby eliminating one potentially costly component. The transmitter and the LO outputs are fed into a

photodiode using a 3dB coupler. The photodiode is a commercially available (ASIP, Inc., Somerset, NJ) 40GHz detector based on asymmetric twin-guide technology [23]. It has a linear responsivity of 1A/W up to >10dBm optical power, and a dark current of 1μA at 2V reverse bias. The photodiode output is passed through a 20 GHz to 40 GHz bandpass amplifier that selects the IF peak and the first lower frequency side lobe. The bandpass amplifier is used in compression such that the nonlinearity allows it to simultaneously serve as the SLD. The SLD mixes the IF peak with the side lobe, generating a signal at the baseband frequency. In earlier work [17], a Schottky diode was used as the SLD, with the IF amplifier operating in its linear regime. The baseband signal is selected by a narrowband filter, thus producing the output signal. Figure 1(b) shows a 15 GHz input signal (solid line) along with the corresponding outputs, with the LO turned on (dashed line) and off (dotted line). The identical shapes of the input and the high fidelity output with the LO on is a result of phase noise cancellation (PNC) that occurs during mixing in the IF amplifier. Very low output signal power in the absence of the LO shows the lack of non-heterodyne terms. This is due to negligible amplitude modulation introduced by the external phase modulator. The frequency response of the link at 0dBm input RF power shows a 3dB bandwidth of 16GHz (Fig. 1(c)).

The time dependent current response of the detector,  $i_{DET}(t)$ , in the externally modulated FM link to a single tone message of amplitude,  $I_M$ , and frequency,  $f_M$ , is given by:

$$i_{DET}(t) = G_{INS} \Re_{DET} \sqrt{P_{LO} P_S r(t)} \cos \left( 2\pi f_{IF} t + \frac{\pi R_{PM}}{V_\pi} I_M \cos(2\pi f_M t) + \Phi(t) \right) \hat{s} \cdot \hat{i} + n(t) \quad (1)$$

where,  $r(t) = (1 + \xi_{RIN,S}(t))(1 + \xi_{RIN,LO}(t))$ ,  $P_S$  and  $P_{LO}$  are the transmitter and LO laser powers,  $\hat{s} \cdot \hat{l}$  is the dot product of the electric field polarization vectors of the two lasers,  $R_{PM}$  is the input impedance of the phase modulator,  $G_{INS}$  is the insertion loss in the various optical components including fiber-to-waveguide coupling losses,  $\mathfrak{R}_{DET}$  is the detector responsivity, and  $f_{IF}$  is the intermediate frequency of the link. Here,  $\Phi(t)$  is the combination of the transmitter and LO phase noises,  $\xi_{RIN,S}$  and  $\xi_{RIN,LO}$  are the RINs of the transmitter and LO lasers, and  $n(t)$  is the white noise current whose spectral density is given by:

$$N = eG_{INS}\mathfrak{R}_{DET}(P_{LO} + P_S) + \frac{4k_B T}{R_L} + G_{INS}^2 \mathfrak{R}_{DET}^2 \left( P_S^2 10^{RIN_S/10} + P_{LO}^2 10^{RIN_{LO}/10} \right), \quad (2)$$

where  $e$  is the electron charge,  $k_B$  is the Boltzman's constant,  $T$  is the absolute temperature, and  $R_L$  is the output load resistance. Following the analysis of the link as given in [14], the noise figure and the dynamic range of the link are given by:

$$NF = \frac{1}{2\beta^2 i_{LO} i_S} \left[ 1 + \frac{1}{2i_{LO} i_S} \left( \frac{G_{BPF}^{(1)}}{G_{BPF}^{(2)}} \right)^2 \right] \left[ 1 + \frac{eR_L}{2k_B T} (i_{LO} + i_S) + \frac{R_L}{k_B T} (i_{LO}^2 + i_S^2) 10^{RIN/10} \right] + 1 \quad (3)$$

$$\text{and} \quad SFDR = \left[ \frac{2k_B T}{R_L} \beta^2 NF \right]^{-2/3}, \quad (4)$$

where  $i_{LO} = G_{INS}\mathfrak{R}_{DET}P_{LO}$ ,  $i_S = G_{INS}\mathfrak{R}_{DET}P_S$ , and  $\beta = \frac{\pi R_{PM}}{V_\pi}$ . Here,  $G_{BPF}^{(1)}$  and  $G_{BPF}^{(2)}$  are the first and second order gain of the band pass IF amplifier operating in its non-linear regime.

An NF=(40±1) dB (Fig. 2) and an SFDR=(108±2) dB-Hz<sup>2/3</sup> (see Fig. 3, inset) were measured in a back-to-back configuration for the FM link, and are shown with

theoretical fits to Eqs. (1) – (4) (solid line). At high LO power, the roll off in the decrease in the measured noise figure is due to phase-to-intensity noise [14] which has not been taken into account in the calculations. As a result, the calculations predict a lower than observed NF at  $P_{LO} > 3\text{dBm}$ . The link response at 15GHz is linear up to  $P_S > 10\text{dBm}$ , as shown in Fig. 3. Noise performance of this link is also compared with an externally modulated FM link with a balanced photodiode with similar responsivity (Fig. 2 dashed line). The use of a balanced photodiode eliminates the laser RIN, and thus improves the noise performance of the link by up to 10dB at an LO power approaching 10dBm. This corresponds to a  $6.7\text{ dB-Hz}^{2/3}$  increase in SFDR (see Eq. 4).

For comparison, an intensity modulated direct detection (IMDD) link was made using the same components as those in the FM architecture. The phase modulator was sandwiched between two 3dB couplers to obtain a MZ modulator, and was used in a back-to-back configuration with the same photodiode used in the FM heterodyne link. At a transmitter laser power of 4mW, a noise figure of  $(59 \pm 1)\text{dB}$  was obtained. This is the reference (Fig. 2 dotted line) against which the heterodyne link can be compared. The IMDD link exhibits an increase of 18dB over the noise figure obtained for the FM heterodyne system operating at a similar laser power. An improved IMDD link would use a linear electro-absorption modulator; but suitable modulators for such applications at 15GHz are not yet available. A more detailed comparison of performance of high frequency links is given in Ref. [17].

In conclusion, a very high bandwidth (16GHz) optical heterodyne analog FM link operating at  $\lambda = 1.55\mu\text{m}$  with pre-emphasis has been demonstrated. The link has been simplified through reduction of the number of components required in the WIRNA

receiver [17] by combining the functionality of the IF amplifier and the SLD. This simplification allowed an operating bandwidth higher than previously achieved, with a SFDR =  $(108 \pm 2)$  dB-Hz<sup>2/3</sup> and NF =  $(40 \pm 1)$  dB. To our knowledge, this is the highest reported bandwidth of a broadband linear analog optical link reported to date, and shows the advantages of employing heterodyne versus direct detection for such applications.

In this work, we have shown that FM heterodyne links are an effective means for implementing high frequency analog signal transmission. FM systems, in general, have a superior noise performance than their AM counterparts [22], and heterodyning allows for boosting of the signal by increasing the LO power. Further improvements using a BPD to eliminate laser RIN have been noted. One disadvantage of an FM heterodyne link, however, is the need for laser wavelength stability and increased circuit complexity. Nevertheless, the WIRNA receiver allows for phase noise cancellation where stability requirements are significantly reduced [10, 14]. In this work we present a simple implementation of the receiver that involves only two components: an IF amplifier and a narrowband filter, thus significantly reducing the penalty of the increased circuit complexity as compared to previous efforts [14].

The authors thank DARPA (RFLICS Program) for partial financial support of this work.

## Captions

**Figure 1:** (a) Block diagram of the analog heterodyne FM link. (b) Input of the link (solid line) has the same shape as the link output with the LO laser on (dashed line), showing phase noise cancellation. The output signal with the LO off (dotted) is negligible due the small amplitude modulation index of the phase modulator. (c) Link response at 0dBm input RF power demonstrates a 3dB bandwidth of 16GHz. The solid line is a guide for the eye.

**Figure 2:** Measured (solid squares) and calculated (solid line) noise figures for the FM link with a single photodiode (SPD) as a function of local oscillator (LO) power. The transmitter laser was operating at 1.5mW CW power. Calculated (dashed line) noise figure for a link with a balanced photodiode (BPD) with a similar responsivity to the SPD is shown for comparison. A noise figure of 59 dB (dotted line) was obtained for an IMDD link at a laser power of 4mW using the same modulator and the detector as in the FM link experiments.

**Figure 3:** Link gain at 15GHz shows a linear responsivity up to >10dBm input RF power. Inset: Measured (data point with error bar) and calculated (solid line) spurious free dynamic range (SFDR) for the FM link with single photodiode (SPD) as a function of local oscillator (LO) power.

## References

- [1] R. Taylor and S. R. Forrest, "Steering of an optically driven true-time delay phased-array antenna based on a broad-band coherent WDM architecture", *IEEE Photon. Technol. Lett.*, vol. 10, pp. 144-146, 1997.
- [2] R. Olshansky, R. Gross, and M. Schimdt, "Subcarrier multiplexed coherent lightwave system for video distribution", *IEEE J. of Select. Areas Commun.*, vol. 8, no. 7, pp. 1268-1275, 1990.
- [3] O. Tonguz and H. Jung, "Personal communications access networks using sub-carrier multiplexed optical links", *J. of Lightwave Technol.*, vol. 14, pp. 1400-1408, 1996.
- [4] E. I. Ackerman and C. H. Cox, "RF fiber-optic link performance", *IEEE Microwave Magazine*, vol. 2, no. 4, pp. 50-58, 2001.
- [5] C. H. Cox, G. E. Betts and L. M. Johnson, "An analytic and experimental comparison of direct and external modulation in analog fiber-optic links", *IEEE Trans. Microwave Theory Tech.*, vol. 38, no. 5, pp. 501-509, 1990.
- [6] G. E. Betts, "Linearized modulator for suboctave bandpass optical analog links", *IEEE Trans. Microwave Theory Tech.*, vol. 42, no. 12, pp. 2642-2649, 1994.
- [7] E. I. Ackerman, C. Cox, G. Betts, et al, "Input impedance conditions for minimizing the noise figure of an analog optical link", *IEEE Trans. Microwave Theory Tech.*, vol. 46, no. 12, pp. 2025-2031, 1998.
- [8] R. Hekley, "Relative intensity noise cancellation in bandpass external modulation links", *IEEE Trans. Microwave Theory Tech.*, vol. 46, no. 12, pp. 2083-2091, 1998.

- [9] *Fiber-Optic Communication Systems*, G. P. Agrawal, John Wiley and Sons, 3<sup>rd</sup> edition, 2002.
- [10] R. F. Kalman, J. C. Fan and L. G. Kazovsky, “Dynamic range of coherent analog fiber-optic links”, *J. Lightwave Technol.*, vol. 12, no. 7, pp. 1263-1277, 1994.
- [11] R. F. Kalman, J. C. Fan and L. G. Kazovsky, “A novel analog optical link with high dynamic range”, *IEEE Photon. Technol. Lett.*, vol. 5, no. 6, pp. 725-728, 1993.
- [12] D. J. Sabido, M. Tabara, T. Fong, R. F. Kalman and L. G. Kazovsky, “Experimental Linewidth-Insensitive Coherent Analog Optical Link”, *J. Lightwave Technol.*, vol. 12, no. 11, pp. 1976-1985, 1994.
- [13] D. J. Sabido, M. Tabara, T. K. Fong, C. L. Lu and L. G. Kazovsky, “Improving the dynamic range of a coherent analog AM optical link using a cascaded linearized modulator”, *IEEE Photon. Technol. Lett.*, vol. 7, no. 7, pp. 813 – 815, 1995.
- [14] R. Taylor and S. R. Forrest, “Optically coherent direct modulated FM analog link with phase noise canceling circuit”, *J. Lightwave Technol.*, vol. 17, no. 4, pp. 556-563, 1999.
- [15] R. Bondurant, D. Welford, S. B. Alexander and V. W. S. Chan, “Frequency noise cancellation in semiconductor lasers by nonlinear heterodyne detection”, *Opt. Lett.*, vol. 11, pp. 791-793, 1986.
- [16] R. Taylor, H. V. Poor and S. R. Forrest, “Phase noise in coherent analog AM-WIRNA optical links”, *J. Lightwave Technol.*, vol. 15, no. 4, pp. 565-575, 1997.

- [17] S. Datta, S. Agashe and S. R. Forrest, "A high bandwidth analog optical heterodyne RF link with high dynamic range and low noise figure", *IEEE Photon. Technol. Lett.*, vol. 16, no. 7, pp. 1733-1735, 2004.
- [18] P. P. Borbat, R. H. Crepeau and J. H. Freed, "Multifrequency two-dimensional Fourier transform ESR: an X/Ku band spectrometer", *J. Magnetic Resonance*, vol. 127, no. 2, pp. 155-167, 1997.
- [19] A. Livne, "System design considerations in fiber-optic networks for active array satellite antenna", *19<sup>th</sup> European Microwave Conference*, pp. 951-958, 1989.
- [20] S. B. Kesler, J. Kesler and G. Levita, "Resolution of coherent radar targets in the near field of an array antenna", *ICASSP 86 Proc.*, vol. 3, pp. 1937-1940, 1986.
- [21] S. S. Agashe, S. Datta, F. Xia and S. R. Forrest, "A Monolithically Integrated Long-Wavelength Balanced Photodiode using Asymmetric Twin-Waveguide Technology", *IEEE Photon. Technol. Lett.*, vol. 16, no. 1, pp. 236-238, 2004.
- [22] *Communication Systems*, Simon Haykin, John Wiley and Sons, 3<sup>rd</sup> edition, 1995.
- [23] F. Xia, J. K. Thomson, M. R. Gokhale, P. V. Studenkov, J. Wei, W. Lin and S. R. Forrest, "An asymmetric twin-waveguide high-bandwidth photodiode using a lateral taper coupler", *IEEE Photon. Technol. Lett.*, vol. 13, no. 8, pp. 845-847, Aug. 2001.

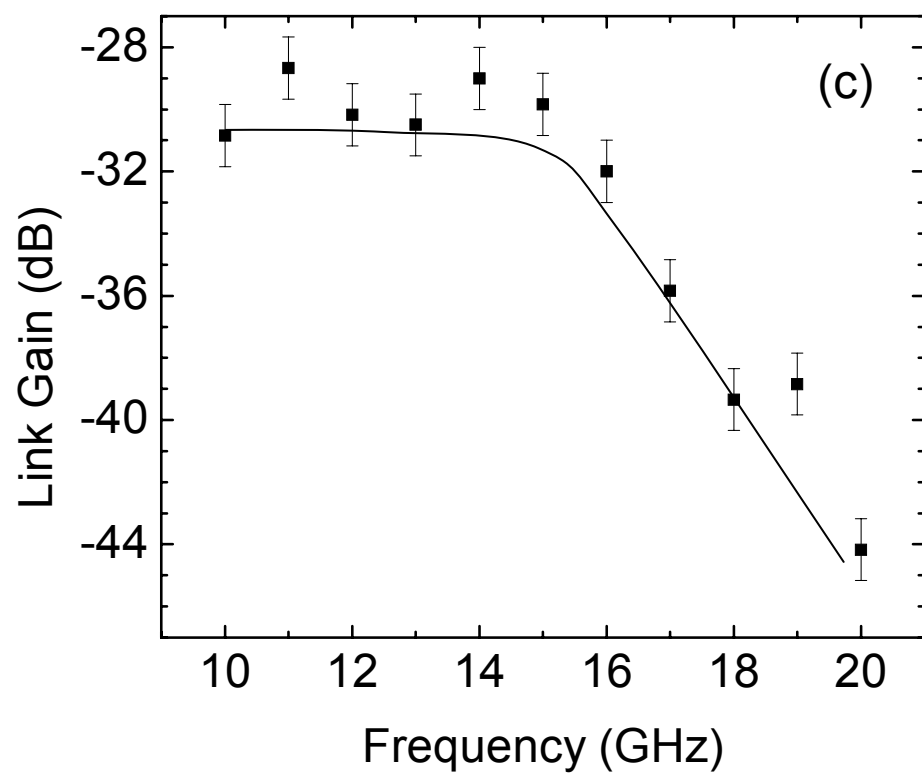
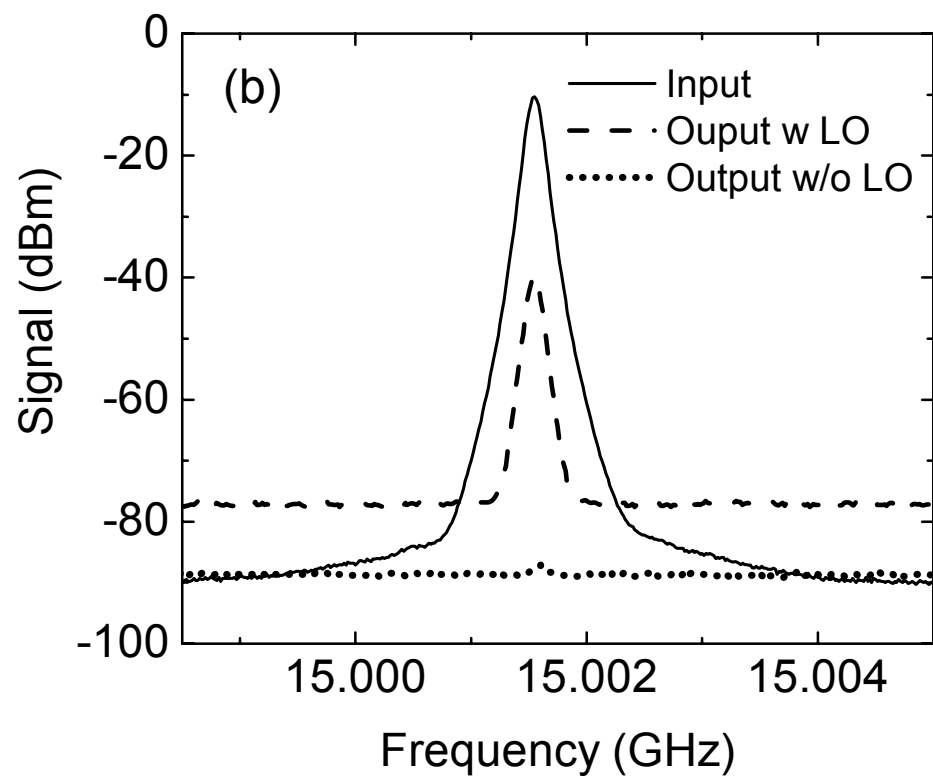
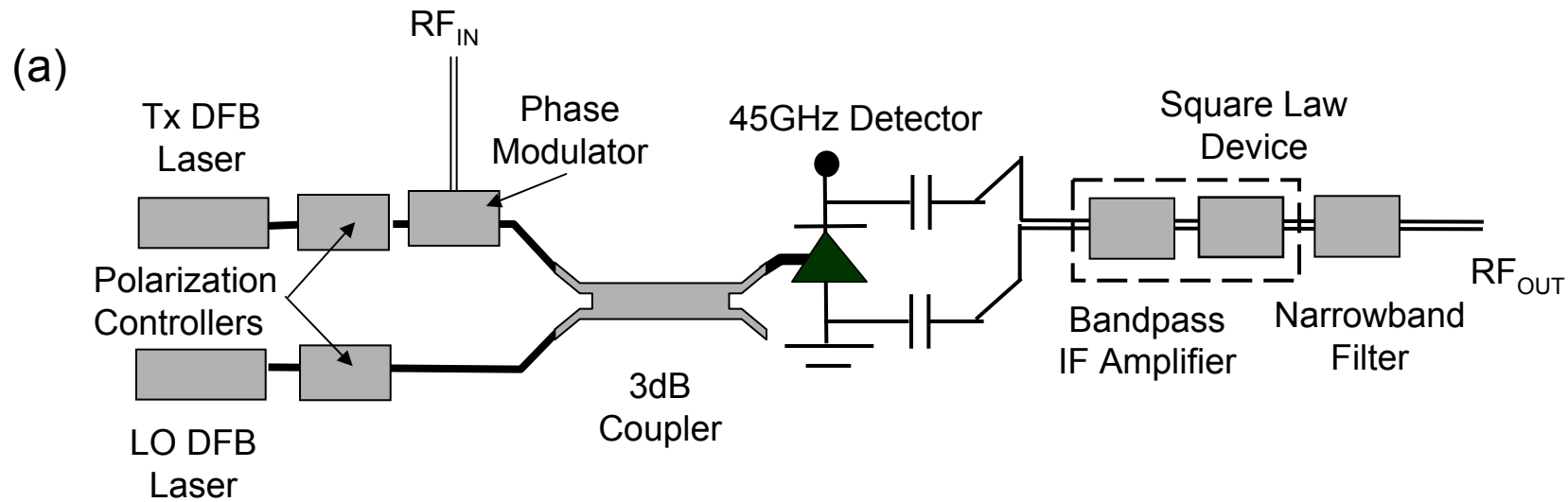


Fig. 1, Datta and Forrest

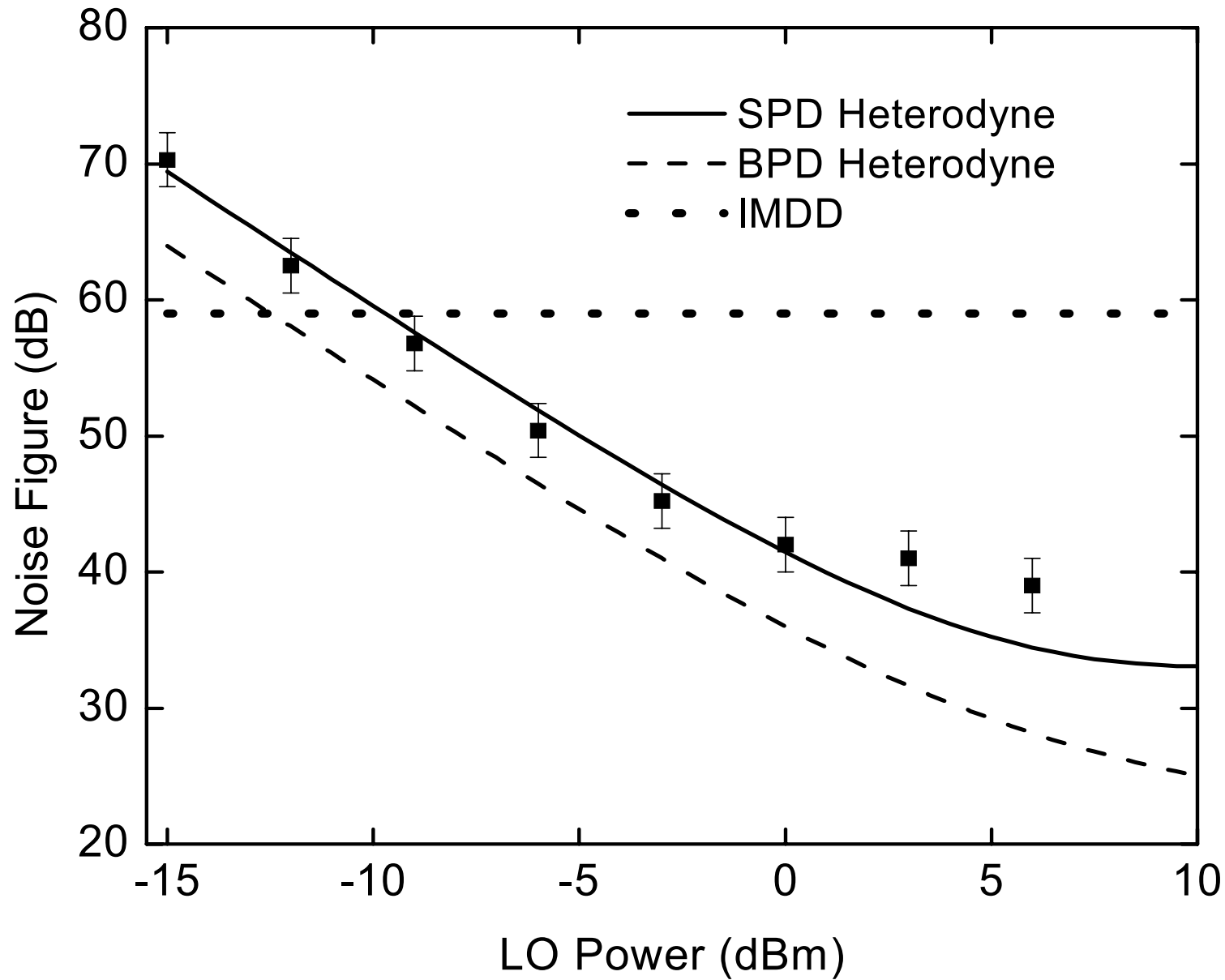


Fig. 2, Datta and Forrest

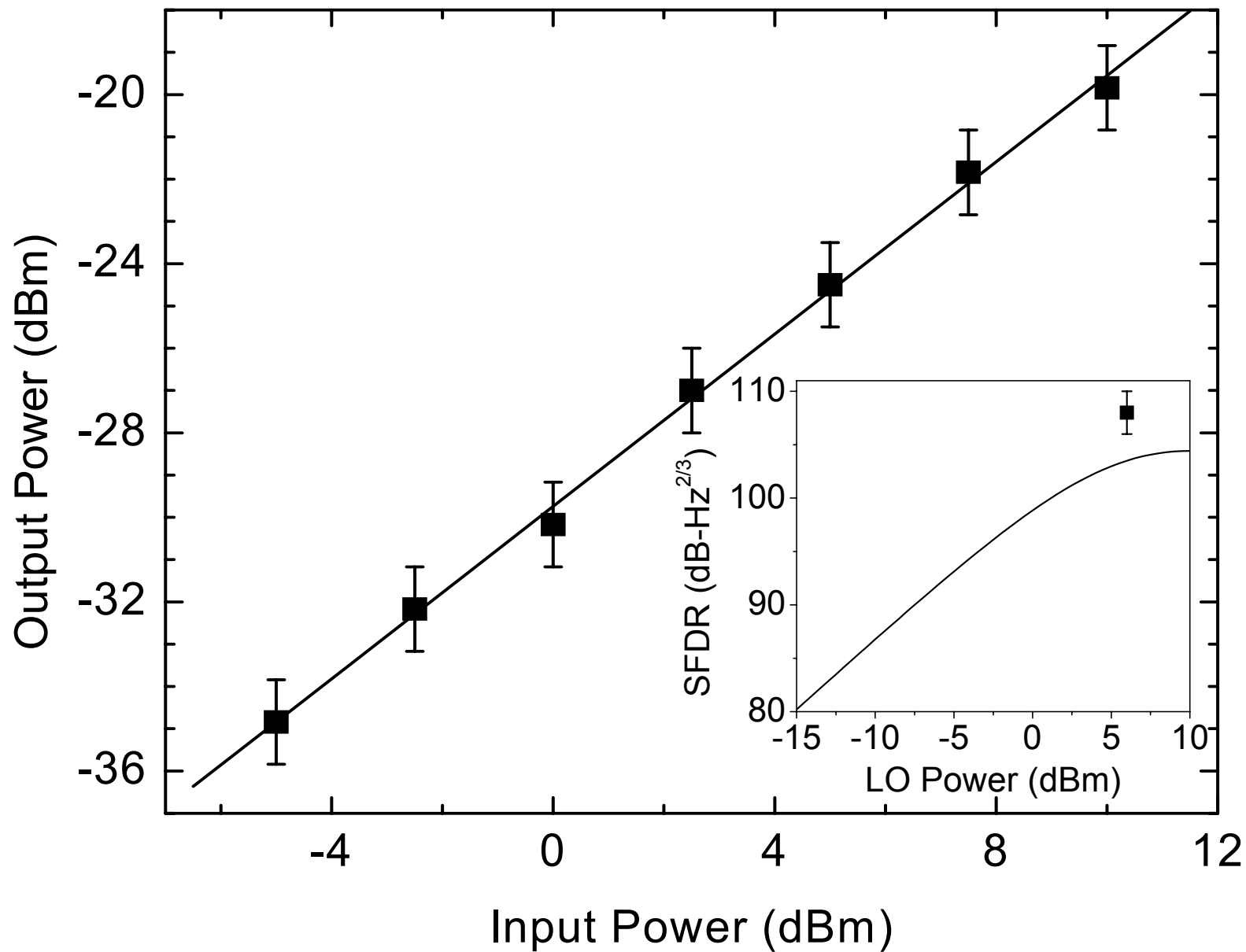


Fig. 3, Datta and Forrest

# **Photonic integration using asymmetric twin-waveguide (ATG) technology.**

## **I. Concepts and theory**

Fengnian Xia, Vinod M. Menon, and Stephen R. Forrest

Princeton Institute for the Science and Technology of Materials (PRISM)

Department of Electrical Engineering, Princeton University

Princeton, NJ 08544

**Abstract** -- We present a universal approach for simply realizing monolithic photonic integration based on asymmetric twin-waveguide (ATG) technology. The ATG structure consists of active and/or passive devices formed in separate, vertically displaced waveguides. Light is transferred between the waveguides via very low loss, lateral, adiabatic tapered mode transformers, allowing different optical functions to be realized in the different waveguides. The design of the adiabatic tapered mode transformer uses an algorithm based on perturbation theory, and show that the same designs can also be deduced from coupled local mode theory. Using our design algorithms, the taper coupler in a waveguide-coupled photodiode transfers >90% of the optical mode intensity from the fiber waveguide to the coupling waveguide, while the taper length is reduced by 35% compared to conventional, two-section linear taper couplers. The taper design algorithm is further optimized to make the adiabatic taper couplers tolerant to variations in incident light polarization, operation wavelength, and dimensional control during fabrication. Finally, we design a taper that adiabatically couples light from the fundamental to the

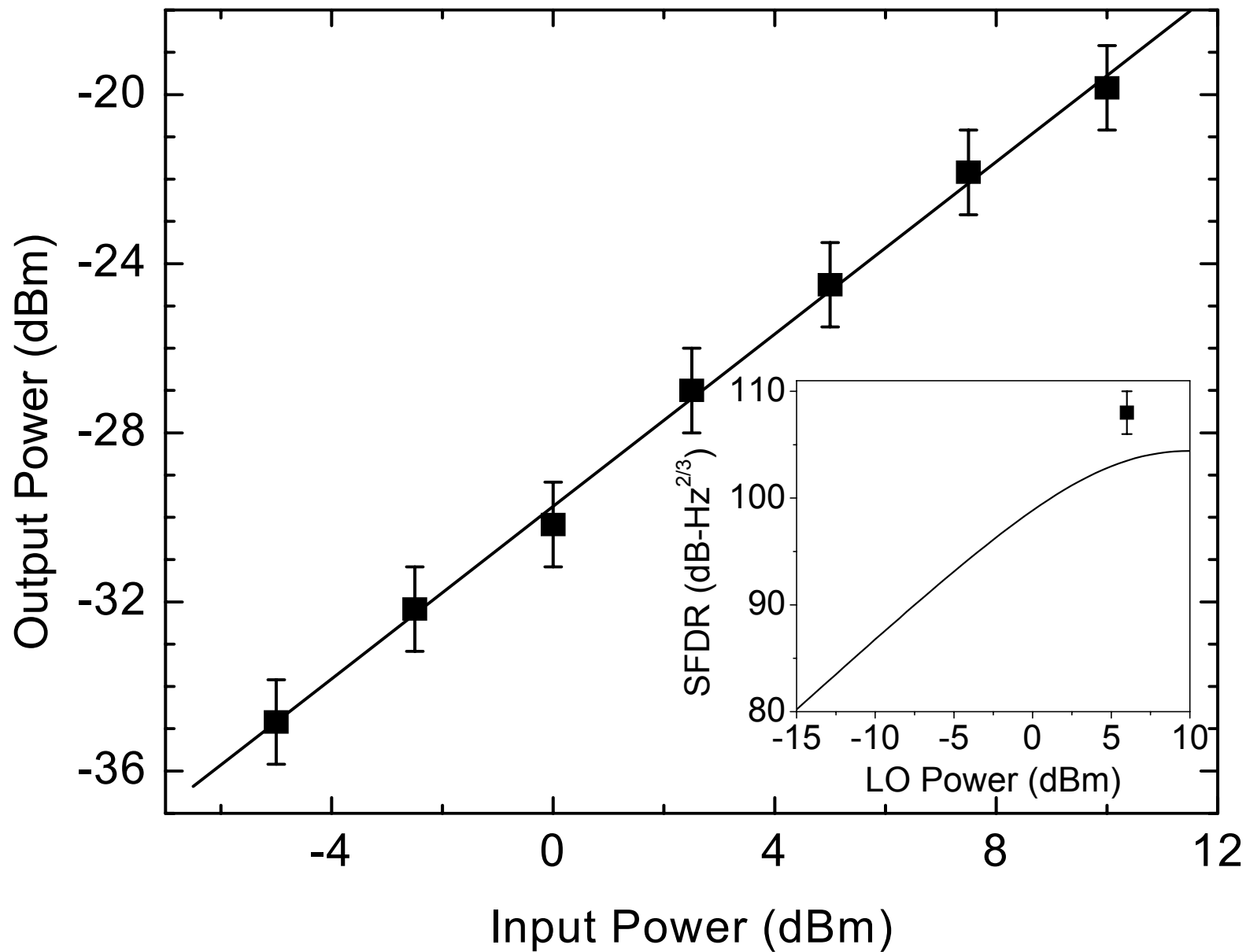


Fig. 3, Datta and Forrest

first order mode. Such a taper coupler is useful in an integrated semiconductor optical amplifier/p-i-n detector circuit. In the following paper (Paper II [V. M. Menon, *et al.*, IEEE J. Select. Topics Quantum Electron., “Photonic integration using asymmetric twin-waveguide (ATG) technology. II. Devices”, vol. , pp. xx-yy, 2005]), we discuss several archetype photonic integrated circuits based on these concepts, that exhibit high performance suitable for many advanced, low cost photonic system applications.

**Keywords** -- Photonic integration, adiabatic taper coupler, perturbation theory, coupled mode, semiconductor optical amplifier, p-i-n detector, receiver.

Email: [forrest@princeton.edu](mailto:forrest@princeton.edu)

## **I. Introduction**

An effective photonic integration technology must combine high performance devices with a low cost (and hence, high yield) fabrication process. Given the enormous diversity of device needs, the design cycle time must be short, such that new systems concepts can be rapidly tested and then deployed. Indeed, in an “ideal” world, a complete library of devices that can be combined in an arbitrary fashion should be readily available to the system designer to allow for the realization of customized, high level and high performance photonic functions. In effect, photonics is in need of a new paradigm where the system designer, not the device physicist, can determine the next generation of integrated components. This paradigm has proven to be enormously successful in the electronics world, where CMOS chip design is primarily driven by the systems needs rather than device limitations. The recently demonstrated asymmetric twin-waveguide (ATG) platform addresses just this problem: it provides a very high performance photonic integration technology platform where the system engineer can lay out a desired, perhaps very complex photonic chip by drawing on a standard library of component designs [2-4]. Then, using standardized epitaxial wafers and fabrication processes, these custom photonic integrated circuits (PICs) can be rapidly realized and readied for manufacture in large scale.

Unlike electronic integrated circuits where only a single active device type (the transistor) needs to be included, photonic integrated circuits require three basic optical

functions: (i) light generation and amplification, (ii) light guiding and coupling, and (iii) light detection. Integration of optical functions has long proven to be particularly difficult and costly to achieve [5, 6], mainly due to the following reasons. To optimize the performance of a device, we require different materials to be employed to achieve each optical function. For example, active regions of high performance light generation and amplification components such as lasers and amplifiers usually consist of strained quantum wells whose transition energies lie at the photon energy in order to achieve high optical gain [7]. Similarly, light guiding and coupling components need materials with a bandgap larger than the photon energy to minimize propagation losses. Materials used in these regions tend to be undoped, and may consist of multiple, interleaved layers, quantum wells [8], or simply a single layer of homogeneous composition surrounded by wide bandgap cladding layers. And finally, light detection components require undoped materials with a bandgap smaller than the photon energy to ensure efficient optical absorption. To maintain the high performance of the discrete components in an integration platform, efficient optical power transfer between these different optical functions must be realized, and parasitic reflections must be minimized since they can be detrimental to the operation of the high gain components such as lasers and semiconductor optical amplifiers (SOAs).

A number of integration techniques have been developed to allow for materials optimization suitable for each separate photonic function. Figure 1 shows some of the

more common techniques applied to the example of the integration of a laser with a waveguide. The first approach is material regrowth (Fig. 1(a)) where different functions are created by optimizing materials by sequential growth in different regions of the wafer [9-13]. Although regrowth provides freedom to optimize each required function, high coupling efficiency without reflections between different components is difficult to achieve [14, 15], and the device characteristics are strongly affected by the regrowth interface which is subject to possible contamination during wafer processing between the regrowth steps [16, 17]. Hence, material regrowth leading to complex, multifunction PICs remains a significant materials science challenge, and typically can result in low device yields and high costs.

Quantum well intermixing (QWI), as shown in Fig. 1(b), allows for the blue shift of the multiple quantum well (MQW) absorption edge after material growth. In this approach, light generation and amplification components are fabricated in the non-intermixed regions, and low loss light guiding components are realized in the intermixed regions. The integrated optical functions must share a similar material structure since growth occurs in only a single step. This primarily results in two constraints. First, efficient light detection components that require thick, undoped bulk materials with a bandgap smaller than the photon energy are difficult to realize using this method. Second, light guiding components must consist of multiple quantum wells similar to light generating devices. Hence it is difficult to optimize the light guiding

material for special device functions such as polarization insensitive waveguides [18] and waveguides with high coupling efficiencies to single-mode optical fibers [3], thereby inevitably leading to compromises in device performance. Several methods have been demonstrated to realize quantum well intermixing such as surface dopant diffusion [19], ion implantation [20], and photo-absorption induced local heating [21]. Surface dopant diffusion or ion implantation can introduce impurities into the multiple quantum well regions where they facilitate atomic inter-diffusion during annealing. The disadvantage is that introduction of impurities into the MQW region results in higher waveguide losses due to free carrier absorption, and may degrade the electrical properties of the integrated devices. In photo-absorption, intermixing is induced by local heating of the MQW active region through illumination by a laser [21]. In this method, the optical and electrical quality of the intermixed materials can be maintained. However, the nature of the thermal process limits the lateral resolution to 100-200 $\mu\text{m}$  [22]. Kowalski, *et al.* demonstrated a damage enhanced QWI technique [23], where a localized bandgap shift of 100meV was achieved by SiO<sub>2</sub> sputtering and subsequent high temperature annealing. Currently, the application of QWI to photonic integrated circuits is limited primarily to laser/waveguide and laser/modulator integration [24-27].

Another integration technique is selective-area growth (SAG) as shown in Fig. 1(c). Here, the substrate is pre-patterned with dielectric masks. By changing the width of the mask openings, the local material growth rate can be changed. Therefore, the thickness

and the transition energy of the quantum wells can be varied within a certain range. Aoki, *et al.* achieved a transition energy shift of up to 120nm in an InGaAsP MQW region [28]. Using this method, multiple quantum well tunable distributed Bragg reflector (DBR) lasers with integrated electro-absorption modulators [29-30] and bulk 2×2 optical switches [31] have been demonstrated. As in material regrowth, device characteristics can be affected by the surface conditions, since growth is performed on a substrate that is subject to processing and possible contamination. As in QWI, all integrated optical functions must share a similar material structure since growth occurs in only a single step, leading to compromises in integrated device performance [3, 18].

Suematsu, *et al.* proposed the twin-waveguide (TG) structure for laser-waveguide integration, which eliminates the need for material regrowth or any post-growth modification of the epitaxial structure [32-34]. In the TG structure, light generation and guiding functions were separated into two different, vertically displaced waveguides by a transparent, 0.3μm thick Al<sub>0.25</sub>Ga<sub>0.75</sub>As layer. In TG structures, the waveguide containing light generation or amplification layers is called the “active waveguide”, while the waveguide containing loss-free light guiding layers is called the “passive waveguide”. Integration is realized by selective removal of the upper, active waveguide while the lower, passive waveguide remains unaffected. The twin-waveguide architecture has the property of a “platform” technology since the different types of components are defined during post-growth processing. A universal epitaxial structure can be grown in advance

without having detailed information about the integrated optical components. A shortcoming of Suematsu, *et al.*'s structure is that the effective indices of both guides must be closely matched, forming a resonantly coupled vertical directional coupler. In this case, the coupling efficiency between the laser and waveguide sections is a sensitive function of layer thickness, refractive index, and device length. Small variations in growth and processing can considerably affect the coupling efficiency, and hence it is impractical to use such a structure to produce high volumes of low cost components.

In the following sections, we will review several modified TG structures that avoid the limitations of the simple structure of Suematsu, *et al.* These include twin-waveguides containing an optical loss layer [35], the asymmetric twin-waveguide (ATG) structure without taper couplers [36], and the asymmetric twin-waveguide (ATG) structure with taper couplers [2]. Indeed, all of these modified versions succeed in eliminating the uncontrolled coupling variations inherent in the structure of Suematsu, *et al.* [32], and thus serve as versatile and flexible integration platforms. However, only in the case of the asymmetric twin-waveguide (ATG) structure with taper couplers, almost loss-free power transfer along with a relaxed fabrication tolerance between different optical functions can be achieved. Numerous complex and high performance photonic integrated circuits consisting of all three optical functions, such as integrated SOA/p-i-n detector receivers [4], integrated twin-waveguide lasers [2], and integrated arrayed waveguide grating (AWG)/p-i-n detector receivers [18], have been realized using this structure. The

fabrication and performance of specific ATG based PICs are the subject of the subsequent paper (Paper II [1]). In this paper (Paper I), we discuss the operational principles and theory of the TG structure. This paper is organized as follows: in Sec. II, III and IV, we will review TG structure with an optical loss layer, an ATG structure without taper couplers, and an ATG structure with taper couplers, respectively. In Sec. V, the adiabatic taper coupler design algorithm is derived using both perturbation theory and coupled local mode theory. Also, we design an adiabatic taper for the example of an ATG waveguide coupled photodiode using this algorithm. After that, tolerant taper coupler and odd mode taper coupler design algorithms are proposed in Sec. VI and VII, respectively. In Sec. VIII, we summarize our findings.

## **II. Twin-waveguide (TG) structure with an optical loss layer**

The generic twin-waveguide (TG) structure introduced by Suematsu, *et al.* [32] is shown in Fig. 2(a). The layers are stacked in the epitaxial growth ( $x$ ) direction, while the guided waves propagate along  $z$ . A TG structure supports two normal eigenmodes [37]: one symmetric (even,  $\phi_e$ ) and one anti-symmetric (odd,  $\phi_o$ ), as shown in Fig. 2(b). The mode profiles at a wavelength of  $\lambda=1.55\mu\text{m}$  are generated by a 2-D beam propagation method (BPM) mode solver [38] for a TG structure grown on an InP substrate. This structure consists of a  $0.54\mu\text{m}$  thick InGaAsP layer (with a bandgap cutoff wavelength of

$\lambda_g=1.2\mu\text{m}$ ), a  $0.5\mu\text{m}$  thick InP separation layer, and a multi-quantum-well active waveguide. The MQW region is comprised of three,  $135\text{\AA}$  thick, 1% compressively strained InGaAsP ( $\lambda_g = 1.55\mu\text{m}$ ) quantum wells separated by  $230\text{\AA}$  thick InGaAsP ( $\lambda_g = 1.2\mu\text{m}$ ) barriers and sandwiched between two,  $113\text{nm}$  thick InGaAsP ( $\lambda_g = 1.2\mu\text{m}$ ) confinement layers. The effective indices of the even and odd eigenmodes in Fig. 2(b) are  $n_e=3.253$  and  $n_o=3.227$ , and the quantum well confinement factors (defined as the fraction of the total mode power residing within the quantum well layers) are  $\Gamma_{\text{QW}}(e)\cong\Gamma_{\text{QW}}(o)=0.039$ . A simple TG integrated device consisting of a Fabry-Perot laser coupled to a passive waveguide is shown in Fig. 3. The left facet is cleaved, and the right facet is a half-mirror etched only through the active waveguide. The lateral (y-direction in Fig. 3) confinement is provided by an etched ridge in the topmost layer. The cavity acts as a resonant coupler, since the even and odd modes have equal gain, resulting in equal distribution of optical power into both modes. As a result of interference effects arising from the different velocities of the two modes, power flows resonantly from one waveguide to the other over a characteristic length:

$$L_c = \frac{\lambda}{2(n_e - n_o)} \cong 30\mu\text{m} \quad (1)$$

Hence, the output transmission efficiency,  $T$ , and etched facet reflectivity,  $R$ , critically depend on the phase difference between these two modes at the etched facet. For a given cavity length, constructive interference occurs in the upper waveguide, resulting in a high

reflectivity, while minimizing the output coupling efficiency. For a different cavity length, constructive interference occurs in the lower waveguide, and the output coupling efficiency will be high. In this case, the facet reflectivity will be at a minimum, and the threshold current of the integrated laser will increase. A typical laser cavity with a length greater than  $500\mu\text{m}$  is many resonant coupling distances long. Hence, a small change in cavity length can strongly affect the laser threshold current and output coupling efficiency. Even if the laser cavity length can be precisely controlled by photolithography, the characteristic length,  $L_c$ , is a sensitive function of the active and passive waveguide layer compositions, thicknesses, and the lateral ridge waveguide width. Inevitable variations in growth and processing will therefore significantly change the characteristic length. Indeed, the maximum coupling between the laser and waveguide achieved by Suematsu, *et al.* [32-34] was only 13%. These possible variations make the simple TG structure impractical for large scale, low cost manufacturing.

The periodic power transfer in the TG structure can be suppressed by structural modifications that lead to discrimination between the even and odd modes. As shown in Fig. 2(b), the odd mode has a node at a point midway between the waveguides, while the even mode has significant intensity at that location. If a thin, narrow bandgap (e.g.  $\text{In}_{0.53}\text{Ga}_{0.47}\text{As}$ ) layer is added at the midpoint between the active and passive waveguide layers, the even mode will experience additional loss, while the odd mode will be largely unaffected. Hence, the odd mode will reach threshold first and dominate the laser

oscillation. Such a TG laser was demonstrated by Xu, *et al.* [35]. In this laser-waveguide PIC, a 10nm thick  $\text{In}_{0.53}\text{Ga}_{0.47}\text{As}$  loss layer was added into the InP separation layer in the structure shown in Fig. 2(b). Assuming an absorption coefficient of  $10^4\text{cm}^{-1}$  at  $\lambda=1.55\mu\text{m}$  in  $\text{In}_{0.53}\text{Ga}_{0.47}\text{As}$ , the calculated modal losses are  $30\text{cm}^{-1}$  and  $0.25\text{cm}^{-1}$  for the even and odd modes, respectively [35].

In twin-waveguide lasers containing a loss layer, when the injection current increases above threshold, the carrier density (and hence the optical gain) will be clamped at its threshold value. Hence, the even mode does not lase with the increased injection current. In semiconductor optical amplifiers (SOAs), gain clamping does not exist, and the modal gain in SOAs can be larger than  $100\text{cm}^{-1}$  [7], so additional loss introduced by a thin  $\text{In}_{0.53}\text{Ga}_{0.47}\text{As}$  layer is insufficient to remove the even mode. Another disadvantage of such an integrated device is its large threshold current. In the TG structure, the odd mode power is split equally between the active and passive waveguides; hence the confinement of the odd mode in the MQW gain region is approximately half that of conventional Fabry-Perot lasers, resulting in a large threshold current [35]. Therefore, the asymmetric twin-waveguide (ATG) structure was introduced to provide an alternative approach to mode selection [36].

### **III. Asymmetric twin-waveguide (ATG) structure without taper couplers**

Another mode selection mechanism employs the built-in gain difference between the even and odd modes, as proposed by Studenkov, *et al.* [36]. The asymmetric TG structure

is designed with different effective indices of the active and passive waveguides, resulting in an uneven power splitting between the two normal modes propagating in the parallel waveguides. Such an ATG structure, shown in Fig. 4 (a), consists of a 0.6 $\mu\text{m}$  thick InGaAsP ( $\lambda_g=1.2\mu\text{m}$ ) layer, a 0.6 $\mu\text{m}$  thick InP, transparent “separation layer”, and a MQW active waveguide comprised of six, 135 $\text{\AA}$  thick, 1% compressively strained InGaAsP ( $\lambda_g = 1.55\mu\text{m}$ ) quantum wells separated by 230 $\text{\AA}$  thick InGaAsP ( $\lambda_g = 1.2\mu\text{m}$ ) barriers and sandwiched between two, 80nm thick InGaAsP ( $\lambda_g = 1.2\mu\text{m}$ ) separate confinement layers. The effective index of the left (active) waveguide is smaller than that of the right (passive) waveguide. As a result, the even and odd modes are unequally split, with the odd mode primarily confined in the left waveguide, while the even mode is concentrated in the right waveguide. Hence, the confinement factor for the odd mode in the multiple quantum wells,  $\Gamma_{\text{QW(o)}}$ , is larger than that of the even mode,  $\Gamma_{\text{QW(e)}}$ . The reflectivity for the odd mode at the etched facet is larger than that of the even mode for the same reasons. Since the odd mode has larger modal gain and reflectivity, lasing will occur only in the odd mode,  $\phi_o$ .

When light is incident on the laser-passive waveguide facet, part of the power is coupled into the passive waveguide mode,  $\phi_p$ . If we assume that the optical fields are real and normalized, the amplitude coupling coefficients of the even and odd modes to the passive waveguide,  $C_e$  and  $C_o$ , are defined as follows:

$$C_e = \iint_A \phi_e \cdot \phi_p dx dy \quad (2)$$

$$C_o = \iint_A \phi_o \cdot \phi_p dx dy \quad (3)$$

In ATG-based lasers, the power coupling coefficient at the laser-passive waveguide facet is  $|C_o|^2$ . Typically, the coupling loss at this facet is approximately 6dB. Hence, the external quantum efficiency of such an ATG laser is approximately 6dB smaller than for a conventional semiconductor laser, which is unacceptable for most photonic system applications.

Nevertheless, a semiconductor optical amplifier can be simply integrated with an ATG laser by this means. As shown in Fig. 4(b), if we assume that the optical field in the passive waveguide incident on the amplifier is  $E_{in}$ , and the optical field in the passive waveguide at the output of the amplifier is  $E_{out}$ , the total input-to-output transmission ratio is [36]:

$$\frac{E_{out}}{E_{in}} = C_e^2 e^{\Gamma_{QW}(e)gL/2} + C_o^2 e^{\Gamma_{QW}(o)gL/2 + i\Delta k \cdot L}, \quad (4)$$

where  $g$  is the gain of the MQW region,  $\Gamma_{QW}$  is the quantum well confinement factor,  $L$  is the length of the amplifier section, and  $\Delta k \cdot L$  is the phase difference between the even and odd modes at the amplifier output facet. As long as the gain is sufficiently large, the odd mode contribution to the output field will dominate over the even mode, and the output-to-input power ratio is:

$$\frac{P_{out}}{P_{in}} \approx C_o^4 e^{\Gamma_{QW}(o)gL}. \quad (5)$$

Hence, the ATG structure uses gain instead of loss to select the desired mode, while simultaneously breaking the symmetry (and hence undesirable resonance) between the even and odd modes. There are two advantages of the ATG compared with the TG structure containing a loss layer. First, the ATG structure allows the integration of high performance semiconductor optical amplifiers, which are essential optical elements in advanced photonic integrated circuits. Second, the threshold current of the ATG laser is reduced compared to that of a TG laser with a loss layer, since the confinement factor  $\Gamma_{QW(o)}$  approaches that of a simple, ridge waveguide Fabry-Perot laser. On the other hand, the disadvantage of the ATG structure is the unavoidably high coupling loss at the laser-passive waveguide facet.

#### **IV. Asymmetric twin-waveguide (ATG) structure with adiabatic taper couplers**

Asymmetric twin-waveguide structures described in Sec. III offer an elegant means to integrate active and passive photonic devices without regrowth, using only simple etching techniques to define the various functional photonic circuit elements. However, a consequence of the asymmetric design is the poor coupling efficiency between the dominant ATG mode (which is mostly confined within the active guide) and the passive waveguide sections. Therefore, it is desirable to have a means for transferring light between the active and passive waveguides with minimum loss, while at the same time taking advantage of the high gain available in a strongly asymmetric TG structure. Both

of these goals can be achieved using a waveguide taper coupler, as demonstrated by Studenkov, *et al.* [2]. In this improved structure shown in Fig. 5, the untapered region is designed with the upper active waveguide having a higher effective index than the lower passive waveguide. Under this condition, the even mode (shown in the top right, Fig. 5) has a larger confinement factor in the active multiple quantum wells. The even mode experiences a larger gain during propagation, and hence is the dominant mode in the untapered region. In the tapered region, the width of the active waveguide narrows, and the power is transferred adiabatically to the passive waveguide. By this means, the approximately 6dB coupling loss in the ATG structure without a taper coupler is avoided.

In the twin-waveguide laser with taper couplers [2], approximately 85% of the even (fundamental) mode power resides in the upper active waveguide, while the remaining 15% resides in the lower waveguide, corresponding to the typical degree of asymmetry (an 85:15 asymmetry) in ATG structures. The confinement factor of the even (fundamental) mode in MQW region (and hence the modal gain) is therefore 85% as large as that of a conventional Fabry-Perot laser. An increased asymmetry is a desirable property since the interaction between the waveguides can be minimized, and the gain of the fundamental mode can reach that of the conventional laser. As shown in Sec. V.A, the taper coupler has to be longer and narrower to achieve high transfer efficiency in cases of large asymmetry. Hence, in most of our twin-waveguide structures, an asymmetry of 85:15 is used.

## **V. A. Design algorithm of adiabatic taper couplers**

Taper couplers have previously been used in integrated laser diodes with spot-size converters [39-41]. These taper couplers transform a highly compact mode to a large mode that allows for efficient, alignment-tolerant coupling between the output waveguide and an optical fiber. In the ATG structure, taper couplers serve as an optical “via”, allowing for efficient optical power transfer between the layered waveguides. For example, three taper couplers are used in an integrated SOA/p-i-n detector receiver [4], where the light is first transferred from a lower light guiding layer (fiber waveguide) to an amplification layer (the semiconductor optical amplifier). After amplification, power is transferred to the upper light guiding layer (coupling waveguide) by two consecutive taper couplers, and finally absorbed by the topmost photodiode layers. As in all ATG designs, the three optical functions are stacked to allow for power transfer from the lowest index, waveguide layer near the substrate, to the light amplification layers, to the highest index, absorption (light detection) layers. By this means all fundamental optical device functions can be integrated in a single epitaxial growth step. Due to the numerous power transfers incurred, designing taper couplers with high power transfer efficiency is essential.

In early work [2, 39, 40], the taper couplers were designed using 3-dimensional BPM simulations, and the underlying physics governing the power transfer was not described. Here, we define two types of optical couplers: resonant and adiabatic. All optimized taper

couplers used in ATG technology are adiabatic. Next, we derive the adiabatic taper coupler design algorithm using perturbation and coupled local mode theory [42]. Finally, a waveguide-coupled ATG photodiode [3] is designed by applying this algorithm.

In resonant couplers, optical power is split equally between both the even (fundamental) and odd (first order) modes, and beating between these two modes transfers the light from one waveguide to the other. The twin-waveguide laser of Suematsu, *et al.* [32-34] is an example of a vertical resonant coupler. As discussed in Sec. III, resonant couplers have been abandoned due to their high sensitivity to unavoidable variations in layer thickness and feature dimensions that result during material growth and device fabrication.

The schematic structure of an adiabatic taper coupler is shown in Fig. 5. Here, “adiabatic” suggests that the power is maintained in the fundamental mode, with negligible coupling into other higher order modes [43]. Let us assume the input optical field in Fig. 5 is the fundamental mode of the lower (passive) waveguide, and power transfer from lower to the upper (active) waveguide occurs via the taper coupler. Due to the adiabatic nature of the taper coupling, the tip width of the taper,  $W_i$ , should be sufficiently small such that the fundamental mode in the lower waveguide is not affected by this feature. On the other hand, the width at the base of the taper,  $W_f$ , should be sufficiently large such that most of the fundamental power at the base is in the upper waveguide. Our objective is to design the shortest taper coupler that minimizes the power scattering from the fundamental into other higher order modes during power transfer.

One solution to adiabatic transfer is to use a long and gentle taper. In this case, the width variation rate is sufficiently small such that the scattering of the optical power into high order modes is minimal [44]. However, to achieve compact devices required in high density PICs, keeping taper couplers as short as possible while maintaining high coupling efficiency is crucial. Here, we derive a design algorithm using perturbation theory that leads to short yet high transfer efficiency taper shapes.

In adiabatic taper couplers, the width variation is usually small, leading to a spatially dependent dielectric permittivity,  $\varepsilon_r(\vec{r})$ , at position  $\vec{r}$ . Hence, we can derive the time independent field  $\Psi=\Psi(\vec{r})$  from the unperturbed field  $\Psi^0(\vec{r})$ , and then add a perturbation to the permittivity  $\varepsilon_r^1(\vec{r})$ , viz:

$$\varepsilon_r(\vec{r}) = \varepsilon_r^0(\vec{r}) + \theta\varepsilon_r^1(\vec{r}), \quad (6)$$

where  $\theta=1$ . Using the wave equation for an unperturbed homogeneous medium, we have:

$$|\vec{k}\rangle = \Psi^0(\vec{r}) = \frac{1}{(2\pi)^{3/2}} \exp(i\vec{k} \cdot \vec{r}) \quad (7)$$

to describe a plane wave with wave-vector,  $\vec{k}$ . The Taylor series expansion of  $\Psi(\vec{r})$  in terms of  $\theta$  is expressed as:

$$\Psi(\vec{r}) = \Psi^0(\vec{r}) + \theta\Psi^1(\vec{r}) + O(\theta^n), \quad (8)$$

where  $O(\theta^n)$  represents all high order terms of  $\theta$  in the expansion. Then:

$$\left( \nabla^2 + \varepsilon_r^0 \frac{\omega^2}{c^2} \right) \theta\Psi^1 + \left( \theta\varepsilon_r^1 \frac{\omega^2}{c^2} \right) \Psi^0 = 0 + O(\theta^n). \quad (9)$$

Equation (9) can be solved by Fourier transformation:

$$\Psi^1(\vec{r}) \equiv \frac{1}{(2\pi)^{3/2}} \int_{\infty} \tilde{\Psi}^1(\vec{p}) e^{i\vec{p} \cdot \vec{r}} d\vec{p}^3, \quad (10)$$

where the field in real space is represented by the harmonics with different momenta,  $\vec{p}$ .

Substituting Eq. (10) into (9), we obtain:

$$\left( \frac{1}{(2\pi)^{3/2}} \int_{\infty} \tilde{\Psi}^1(\vec{p}) (\vec{k} \cdot \vec{k} - \vec{p} \cdot \vec{p}) e^{i\vec{p} \cdot \vec{r}} d\vec{p}^3 \right) + \left( \varepsilon_r^1 \frac{\omega^2}{c^2} \right) \left( \frac{1}{(2\pi)^{3/2}} \exp(i\vec{k} \cdot \vec{r}) \right) = 0. \quad (11)$$

Multiplying Eq. (11) by  $\exp(-i\vec{q} \cdot \vec{r})$ , and then integrating over space, we have

$$\tilde{\Psi}^1(\vec{q}) = \frac{\left\langle \vec{q} \left| \varepsilon_r^1 \frac{\omega^2}{c^2} \right| \vec{k} \right\rangle}{\vec{q} \cdot \vec{q} - \vec{k} \cdot \vec{k}}. \quad (12)$$

Here, Eq. (12) represents the scattering amplitude from  $|\vec{k}\rangle$  to  $|\vec{q}\rangle$  due to the perturbation of  $\varepsilon_r^1$ .

Now, let us consider a length of adiabatic taper coupler extending from  $z_1$  to  $z_2$ . The length is sufficiently small such that it can be described by  $\varepsilon_r^0$  perturbed by  $\varepsilon_r^1$ . The fundamental mode in this case is:

$$|0\rangle = \frac{1}{\sqrt{z_2 - z_1}} e^{ik_0 z} |m0\rangle, \quad (13)$$

while the first order mode is:

$$|1\rangle = \frac{1}{\sqrt{z_2 - z_1}} e^{ik_1 z} |m1\rangle. \quad (14)$$

In Eq's. (13) and (14),  $k_i$  is the wave vector of mode  $i$ ,  $|mi\rangle$  is the field distribution in the x-y plane of mode  $i$ , and  $\sqrt{z_2 - z_1}$  is a normalization factor. Here, only modes 0 and 1

are considered, and the scattering from mode 0 to other higher order modes is neglected.

Substituting Eq's. (13) and (14) into Eq. (12), we have:

$$\begin{aligned}
& \left| \frac{\left\langle 1 \left| \varepsilon_r^{-1} \frac{\omega^2}{c^2} \right| 0 \right\rangle}{k_0^2 - k_1^2} \right| \\
&= \left| \frac{\int_{z_1}^{z_2} \left( \frac{1}{\sqrt{z_2 - z_1}} \right)^2 e^{i(k_1 - k_0)z} \left\langle m1 \left| \varepsilon_r^{-1} \frac{\omega^2}{c^2} \right| m0 \right\rangle dz}{k_0^2 - k_1^2} \right| \\
&= \left| \frac{\left\langle m1 \left| \varepsilon_r^{-1} \frac{\omega^2}{c^2} \right| m0 \right\rangle}{k_0^2 - k_1^2} \right|. \tag{15}
\end{aligned}$$

The scattering rate per unit length, R, is then:

$$R = \frac{\left| \left\langle m1 \left| \varepsilon_r^{-1} \frac{\omega^2}{c^2} \right| m0 \right\rangle \right|}{(k_0^2 - k_1^2)(z_2 - z_1)}. \tag{16}$$

Love and Henry proposed the optimal adiabatic optical fiber taper design [45], in which the scattering loss, R, is uniformly distributed over the length of the taper. Originally, this idea appeared in the design of a “constant hyper-coupling coefficient” microwave velocity coupler [46]. Here, we apply the same rule to the adiabatic taper couplers in the ATG structure. Equation (16) can thus be modified to:

$$\Delta k_z(z_2 - z_1) = \frac{\omega^2 \left| \left\langle m1 \left[ \varepsilon_r(x, y; z_2) - \varepsilon_r(x, y; z_1) \right] m0 \right\rangle \right|}{R(k_0 + k_1)c^2}, \tag{17}$$

where  $\Delta k_z = k_0 - k_1$ . If we assume that  $k_0 + k_1$  is a constant along the entire taper, then in the

limit of  $z_2 \rightarrow z_1$ , we have:

$$1 = A \frac{|\langle m1 | d\varepsilon_r | m0 \rangle|}{\Delta k_z dz}, \quad (18)$$

where A is a constant. In terms of the change in width, w, per length of taper, Eq. (18)

becomes:

$$1 = A \frac{|\langle m1 | d\varepsilon_r | m0 \rangle|}{\Delta k_z dw} \cdot \frac{dw}{dz}. \quad (19)$$

This leads to the following taper design algorithm:

$$z = A \int_{w_i}^w \frac{|\langle m1 | d\varepsilon_r | m0 \rangle|}{\Delta k_z}. \quad (20)$$

To simplify the numerical calculation, we replace  $\langle m1 | d\varepsilon_r | m0 \rangle$  in Eq. (20) by  $d\langle m1 | \varepsilon_r | m0 \rangle$ . The validity of this transformation is shown as follows:

$$\begin{aligned} d\langle m1 | \varepsilon_r | m0 \rangle - \langle m1 | d\varepsilon_r | m0 \rangle &= (d\langle m1 |) \varepsilon_r | m0 \rangle + \langle m1 | \varepsilon_r (d\langle m0 |) \\ &\approx \varepsilon_r d\langle m1 | m0 \rangle = 0. \end{aligned} \quad (21)$$

In this derivation, we assume that the dielectric constant of any quaternary (InGaAsP) or ternary (InGaAs) material lattice-matched to InP can be approximated by that of InP. We also use the orthogonality condition between eigenmodes 0 and 1. Now, Eq. (20) can be modified to yield:

$$z = A \int_{w_i}^w \frac{|d\langle m1 | \varepsilon_r | m0 \rangle|}{\Delta k_z}. \quad (22)$$

Given the total taper length, tip width  $W_i$ , and base width  $W_f$ , the scale factor A can be found, thus determining the optimal taper shape.

A simplified taper design algorithm has also been described by Bakke, *et al.* [43] based on coupled local mode theory [42]. Indeed, an improved algorithm that gives the same result as Eq. (22) can also be derived using the method of local modes. In this approach, the coupling coefficient between mode 0 and 1,  $C_{01}(z)$ , is [42]:

$$C_{01}(z) = \frac{P}{\Delta k_z} \langle m1 | \frac{d\varepsilon_r}{dz} | m0 \rangle, \quad (23)$$

where P is a constant, and other notations have the same meanings as before. As shown in Eq. (21), Eq. (23) can be approximated by:

$$C_{01}(z) = \frac{P}{\Delta k_z} \frac{d \langle m1 | \varepsilon_r | m0 \rangle}{dz}. \quad (24)$$

Assuming a constant scattering rate, we have:

$$1 = P \frac{d \langle m1 | \varepsilon_r | m0 \rangle}{\Delta k_z dz}. \quad (25)$$

Equation (22) is then obtained.

Using the perturbation method, we derive the scattering intensity from plane wave  $|\vec{k}\rangle$  to  $|\vec{q}\rangle$  due to the perturbation of  $\varepsilon_r^1$  to obtain Eq. (22) for non-plane wave modes  $|0\rangle$  and  $|1\rangle$ . In coupled local mode theory proposed by Marcuse [42], the coupling coefficient, Eq. (23), is obtained by expanding the optical field using the “slowly varying” local mode profiles. Although different approximations are used in these two approaches, the same algorithm, Eq. (22), is finally obtained.

## V. B. Example design: A waveguide-coupled p-i-n photodiode

We now design an adiabatic taper for the example of an ATG waveguide-coupled photodiode [3]. The index profile and a 3-D schematic view of the photodiode are shown in Fig. 6. The  $5\mu\text{m}$  wide by  $3\mu\text{m}$  deep diluted fiber waveguide consists of 5 periods of  $500\text{\AA}$  thick  $\text{In}_{0.79}\text{Ga}_{0.21}\text{As}_{0.45}\text{P}_{0.55}$  ( $E_g = 1.03\text{eV}$ ) layers interspersed between  $0.55\mu\text{m}$  thick InP layers, forming a near circular mode that allows for low-loss and tolerant coupling to a lensed, single mode optical fiber with a lens diameter of  $22\mu\text{m}$ . The coupling guide consists of two,  $300\text{\AA}$  thick  $\text{In}_{0.79}\text{Ga}_{0.21}\text{As}_{0.45}\text{P}_{0.55}$  layers interspersed between  $900\text{\AA}$  thick InP layers on both sides of a central  $\text{In}_{0.79}\text{Ga}_{0.21}\text{As}_{0.45}\text{P}_{0.55}$  layer with a thickness of  $0.27\mu\text{m}$ . The light is finally absorbed in a  $0.525\mu\text{m}$  thick  $\text{In}_{0.53}\text{Ga}_{0.47}\text{As}$  layer on top of the coupling guide, passing through a  $0.15\mu\text{m}$  thick,  $\text{In}_{0.79}\text{Ga}_{0.21}\text{As}_{0.45}\text{P}_{0.55}$  index matching layer doped with Si at  $2 \times 10^{18}\text{cm}^{-3}$  positioned between the coupling guide and the absorption layer [3]. The tip and base widths of the tapered coupling guide are  $1\mu\text{m}$  and  $3\mu\text{m}$ , respectively. The coupling waveguide structure is designed to ensure that at the base of the tapered coupling waveguide, approximately 85% of the fundamental mode power is confined in the coupling waveguide, and 15% is within the fiber waveguide (corresponding to an 85:15 asymmetry). If more power is kept in the coupling waveguide at the base, the internal quantum efficiency of the photodiode can be enhanced since it is easier for the light in the coupling guide to be absorbed by the top photodiode. In this ATG structure, the large, nearly circular optical mode of the fiber waveguide ensures high

efficiency, position tolerant coupling to a single mode optical fiber, while the compact mode in the coupling waveguide allows for the efficient optical absorption in the uppermost p-i-n photodiode. The taper shape is designed using Eq. (22). First, the scattering matrix,  $S_{01}$ , is calculated from:

$$S_{01} = \frac{|\mathbf{d} \langle m1 | \epsilon_r | m0 \rangle|}{dw \bullet \Delta k_z} \quad (26)$$

at different taper widths from the tip,  $W_i$ , to the base,  $W_f$ . The scattering intensity is plotted for two different asymmetries in Fig. 7(a). Using Eq. (22), we obtain a relationship between  $z$  and  $w$ , with unknown constant,  $A$ . Figure 7(b) shows such a taper with arbitrary length  $L$ . Then for a taper length  $L$ ,  $A$  is determined.

Next, we calculate the transfer efficiency using 3-D BPM simulations as functions of the taper length,  $L$ , using the fundamental mode of the fiber waveguide as the input optical field. The transfer efficiency represents the value of the overlap integral between the calculated field and the fundamental eigenmode at the base of the taper coupler, as shown in Fig. 8. Here, the transfer efficiency as a function of  $L$  using a two section linear taper coupler [3] is also shown. Using the optimal taper shape, a transfer efficiency of 90% is achieved when the taper length reaches  $290\mu\text{m}$ . If the two section linear taper coupler [3] is used, the taper has to be longer than  $440\mu\text{m}$  to obtain the same high transfer efficiency. Hence, a length reduction of 35% is achieved using our optimizing algorithm.

Previously, it has been suggested that there is a resonant point along the taper coupler

around which the power transfer is maximized by beating between the odd and even modes [2, 39, 40]. This is in fact an inaccurate description of the power transfer process. As shown in Fig. 7(a), there is a scattering peak along the taper coupler at particular taper width corresponding to the resonant point [2, 39, 40]. However, the existence of such a peak does not mean that the coupling itself is, in fact, resonant. That is, modifying Eq. (22) to:

$$\frac{dz}{dw} = A \frac{|d \langle m1 | \varepsilon_r | m0 \rangle|}{dw \bullet \Delta k_z} = AS_{01}, \quad (27)$$

we find that around the resonant point, the scattering intensity,  $S_{01}$ , is significantly larger than elsewhere along the taper. According to Eq. (27), the taper width should be varied slowly in the region of the resonant point to minimize scattering losses. However, the taper width can be varied more rapidly at other points where it is difficult for the fundamental (even) mode power to be scattered into the first order mode (odd). Hence, excitation of the first order mode is minimized in adiabatic taper couplers, and beating between the fundamental and first order modes is very weak along the entire taper coupler length.

In Ref. [3], the two-section taper consists of a 400 $\mu\text{m}$ -long linear taper from 1 $\mu\text{m}$  to 2 $\mu\text{m}$ , followed by a 60 $\mu\text{m}$ -long linear taper from 2 $\mu\text{m}$  to 3 $\mu\text{m}$ . As shown in Fig. 7(a), the resonant point is at a taper width of approximately 1.8 $\mu\text{m}$ . Hence, the two-section linear taper is a two-step approximation to the optimized taper. The first section of the taper

contains the resonant point, so the taper width variation rate should be small to minimize scattering. In the second taper section, the scattering is weak so that the taper width variation rate can be large.

To enhance the internal quantum efficiency of the photodiode, the effective index of the tapered coupling waveguide should be increased so that more of the fundamental power at the taper base is within the coupling guide. Asymmetry between the fiber and coupling guides is increased by increasing the central InGaAsP layer thickness [3] in the coupling guide from  $0.27\mu\text{m}$  to  $0.35\mu\text{m}$ . With this modification, 95% of the fundamental mode power is in the coupling guide and 5% of the fundamental power is in the fiber waveguide at the taper base (corresponding to a 95:05 asymmetry). Then, optimization is obtained by iterating the taper design process. The scattering matrix versus taper width, taper shape, and transfer efficiency versus total length  $L$  are also shown in Fig. 7(a) and (b), and Fig. 8, respectively.

Comparing the scattering intensity for different degrees of asymmetry in Fig. 7(a), we notice two phenomena. First, the peak scattering intensity increases with asymmetry. Second, the taper width corresponding to the peak scattering intensity decreases. Increased scattering intensity results in larger optical loss since it is easier for the fundamental power to be scattered into the first order mode. As shown in Fig. 8, a longer taper is needed to achieve a high transfer efficiency. Also, the taper narrows as shown in Fig. 7(b). A large power splitting ratio is a desirable property in the ATG structure since it

reduces the interaction between different optical functions in the regions where more than a single waveguide layer exists. However, when designing the splitting ratio, one has to take the optimized taper length and shape into account. A long taper coupler requires more space, and may also introduce additional propagation losses. On the other hand, a narrow taper is difficult to fabricate using conventional contact photolithography and dry etching techniques.

## **VI. Design of fabrication-tolerant taper couplers**

In the previous section, we designed the taper coupler shape and length to achieve maximum power transfer efficiency. In practice, designing a taper coupler that is insensitive to unavoidable process variations is an important consideration leading to high manufacturing yields, and hence to low component cost. Additionally, polarization insensitivity is often required in waveguide-coupled photodiodes such as in Fig. 6 [3]. Finally, it may be useful for the taper coupler to allow for high transfer efficiency over a wide optical bandwidth, e.g., to serve in applications at both 1.3 and 1.55 $\mu\text{m}$  wavelengths. All of these properties should be maintained when the taper width is subject to unavoidable variations introduced in the fabrication process.

For polarization independence, power scattering from the fundamental mode into the first order mode for both TE and TM polarization must be simultaneously minimized.

According to Eq. (27), in this case the width variation rate should be kept small for both TE and TM resonant peaks. Hence, Eq. (27) is modified as follows:

$$\frac{dz}{dw} = A \max \left\{ \left[ \frac{|d \langle m1 | \varepsilon_r | m0 \rangle|}{dw \bullet \Delta k_z} \right]_{TE}, \left[ \frac{|d \langle m1 | \varepsilon_r | m0 \rangle|}{dw \bullet \Delta k_z} \right]_{TM} \right\}. \quad (28)$$

Then, the taper design algorithm Eq. (24) becomes:

$$z = A \int_{w_i}^W \max \left\{ \left[ \frac{|d \langle m1 | \varepsilon_r | m0 \rangle|}{\Delta k_z} \right]_{TE}, \left[ \frac{|d \langle m1 | \varepsilon_r | m0 \rangle|}{\Delta k_z} \right]_{TM} \right\}. \quad (29)$$

Using similar arguments, the taper coupler can be designed to be tolerant to both polarization and wavelength.

Taper couplers tolerant to fabrication variations can be obtained in an analogous manner. If we assume that the optimum taper width is  $W$ , and the designed fabrication tolerance is  $\Delta W_T$  (implying that changes in the transfer efficiency should remain acceptably small if the fabricated taper width varies within  $W \pm \Delta W_T/2$ ), the design algorithm of Eq. (24) can be modified to:

$$z = A \int_{w_i}^W \max \left\{ \frac{|d \langle m1 | \varepsilon_r | m0 \rangle|}{\Delta k_z} \right\}_{W \in W \pm \Delta W_T/2}. \quad (30)$$

Tolerant taper coupler design is similar to that described in Sec. V, except that the scattering matrix has to be calculated under different conditions until  $S_{01}$  is maximized. As shown by Eq's. (30) and (27), a tolerant taper coupler is no longer an optimal one [45] since the scattering intensity is no longer uniform along the taper length. The taper shape (and hence, the transfer efficiency) deviates more severely from an optimal one with increasing fabrication tolerance,  $\Delta W_T$ .

To illustrate this tradeoff, the ATG photodiode in Sec. V. B. is redesigned using the tolerant taper design algorithm. An asymmetry of 85:15 is chosen, and the taper length is fixed at  $400\mu\text{m}$ . Figure 9 shows the simulated transfer efficiency as a function of the taper width variation for different designed fabrication tolerances,  $\Delta W_T$ . Here, we assume the width variation is uniform along the entire taper length. The transfer efficiency approximately remains unchanged if the width variation is within  $W \pm \Delta W_T/2$ . The peak transfer efficiency decreases by approximately 9% if the designed fabrication tolerance increases from zero to  $0.4\mu\text{m}$ , an achievable value using conventional contact lithography.

Hence, the highest achievable transfer efficiency with a fixed taper length depends on the required fabrication tolerance. If the fabrication error can be minimized, a less tolerant taper shape can be used, and a higher transfer efficiency is achieved. On the other hand, if a large fabrication tolerance is needed, part of the transfer efficiency is sacrificed.

## **VII. The odd mode method: Extending the definition of the adiabatic taper coupler**

In the adiabatic taper couplers discussed up to this point, almost all of the optical power is maintained in the fundamental mode, with negligible coupling to higher order modes. Here, we extend the definition of an adiabatic taper coupler as follows: a taper coupler is considered to be adiabatic when the optical power is kept within a particular

mode, but not necessarily the fundamental mode, with negligible coupling to other modes along its length.

Figure 10(a) shows a 3-D perspective view of such a “higher order” taper, whose index profile is shown in Fig. 10(b). At the taper base, the fundamental mode (mode 0) power is concentrated in the uppermost passive waveguide, while the first order mode (mode 1) power is primarily in the middle active waveguide, since the material index of the passive guide is larger than that of the active guide. Since the objective is to transfer the power from the fiber guide to the active guide, the power should be kept in the first order mode (mode 1) during transfer, with negligible coupling to other modes. Such a taper coupler is useful in integrated SOA/p-i-n detector PICs [4] since the upper, passive guide serves as an intermediate layer between the underlying semiconductor optical amplifier [2] and the top photodiode [3].

Assume that the input optical field is propagating in the fundamental mode of the fiber guide, and the objective is to transfer the power into the active guide. When the optical field propagates along the fiber guide and is incident on the taper tip, the field must be almost identical to the first order mode at this point. If the tip is too small, the optical field will be almost identical to the fundamental mode at the taper tip. In this case, a significant amount of the power can be transferred into the passive guide as in conventional adiabatic taper couplers. On the other hand, for large  $W_i$ , most of the power will remain within the fiber guide.

The design of the taper coupler in this case is found using:

$$z = A \int_{W_i}^W \max \left\{ \frac{|d \langle m1 | \epsilon_r | m0 \rangle|}{\Delta k_{z,10}}, \frac{|d \langle m1 | \epsilon_r | m2 \rangle|}{\Delta k_{z,12}} \right\} \quad (31)$$

Here,  $\Delta k_{z,10}$  and  $\Delta k_{z,12}$  represent the propagation constant differences between mode 1 and mode 0, and mode 1 and mode 2, respectively. The optical power should be kept in the first order mode, hence the coupling between the first order and fundamental modes, and the coupling between the first and second order modes should both be considered. We call this method “the odd mode method”, since most of the power is maintained within the first order mode during the transfer, and the first order mode is an “odd mode” in conventional twin-waveguide structures [32].

## VIII. Conclusion

We have described the concepts and theory underlying asymmetric twin-waveguide (ATG) integration technology. The context and important developments that have led to the ATG technology have been reviewed. A simple and general taper design algorithm has been derived using perturbation theory. The same results are also deduced from coupled local mode theory. We have optimized the algorithm to lead to compact taper designs that are relatively insensitive to variations in incident light polarization, operational wavelength, and dimensional control during fabrication. The fabrication tolerance is, to some extent, achieved at the expense of the coupling efficiency for a fixed taper length.

For example, the peak transfer efficiency decreases by ~10% if the designed taper fabrication tolerance increases from zero to  $0.4\mu\text{m}$  for a typical fiber guide to photodiode coupler, assuming a 85:15 asymmetry. We have extended the definition of the adiabatic coupler to include higher order mode coupling schemes, and proposed design algorithms for such tapers. In Paper II [1], several photonic integrated circuits based on the ATG concept using the design algorithms are discussed.

The authors gratefully acknowledge DARPA for support of this work through the CS-WDM and RFLICs programs. We also thank Milind Gokhale, Jie Yao, and Pavel Studenkov of ASIP Inc., Somerset, NJ for helpful discussions.

## References

1. V. M. Menon, F. Xia, and S. R. Forrest, "Photonic integration using asymmetric twin-waveguide (ATG) technology. II. Devices", IEEE J. Select. Topics Quantum Electron. vol. , pp xx-yy, 2005.
2. P. V. Studenkov, M. R. Gokhale, and S. R. Forrest, "Efficient coupling in integrated twin-waveguide lasers using waveguide tapers," IEEE Photon. Technol. Lett., vol. 11,

- pp. 1096-1098, 1999.
3. F. Xia, J. K. Thomson, M. R. Gokhale, P. V. Studenkov, J. Wei, W. Lin, and S. R. Forrest, "An asymmetric twin-waveguide high-bandwidth photodiode using a lateral taper coupler," *IEEE Photon. Technol. Lett.*, vol. 13, pp. 845-847, 2001.
  4. F. Xia, J. Wei, V. M. Menon, and S. R. Forrest, "Monolithic integration of a semiconductor optical amplifier and a high bandwidth p-i-n photodiode using asymmetric twin-waveguide technology," *IEEE Photon. Technol. Lett.*, vol. 15, pp. 452-454, 2003.
  5. E. Pennings, G. Khoe, M. K. Smit, and T. Staring, "Integrated-optic versus microoptic devices for fiber-optic telecommunication systems: a comparison," *IEEE J. Select. Topics Quantum Electron.*, vol. 2, pp.151-164, 1996.
  6. B. Mersali, A. Ramdane, and A. Carencu, "Optical-mode transformer: A III-V circuit integration enabler," *IEEE J. Select. Topics Quantum Electron.*, vol. 3, pp.1321-1331, 1997.
  7. L. A. Coldren and S. W. Corzine, *Diode lasers and photonic integrated circuits*, Wiley-interscience Publication, New York, 1995.
  8. E. Bigan, A. Ougazzaden, F. Huet, M. Carre, A. Carencu, and A. Mircea, "Efficient electroabsorption in InGaAsP/InGaAsP MQW optical waveguide," *Electron. Lett.*, vol. 27, pp. 1607-1609, 1991.

9. C. E. Hurwitz, J. A. Rossi, J. J. Hsieh, and C. M. Wolfe, "Integrated GaAs/AlGaAs double hetero-structure laser," *Appl. Phys. Lett.*, vol. 27, no. 4, pp. 241-243, 1975.
10. P. J. Williams, P. M. Charles, I. Griffith, L. Considine, and A. C. Carter, "High performance buried ridge DFB lasers monolithically integrated with butt coupled strip loaded passive waveguides for OEIC," *Electron. Lett.*, vol. 26, pp. 142-143, 1990.
11. Y. J. Yan, M. L. Masanovic, E. J. Skogen, Z. Hu, D. J. Blumenthal, and L. A. Coldren, "Optical mode converter integration with InP/InGaAsP active and passive waveguide using a single regrowth process," *IEEE Photon. Technol. Lett.*, vol. 14, pp. 1249-1251, 2002.
12. M. L. Masanovic, V. Lai, J. S. Barton, E. J. Skogen, L. A. Coldren, and D. J. Blumenthal, "Monolithically integrated Mach-Zehnder interferometer wavelength converter and widely tunable laser in InP," *IEEE Photon. Technol. Lett.*, vol. 15, pp. 1117-1119, 2003.
13. H. Kunzel, S. Ebert, R. Gibis, R. Kaiser, H. Kizuki, S. Malchow, and G. Urmann, "Selective MOMBE growth of InP-based waveguide/laser butt-joints," *J. Crystal Growth*, vol. 198, pp. 52-56, 1998.
14. J. Wallin, G. Landgren, K. Streubel, S. Nilsson, and M. Oberg, "Selective area regrowth of butt-joint coupled waveguides in multi-section DBR lasers," *J. Crystal Growth*, vol. 124, pp. 741-746, 1992.

15. O. Kayser, B. Opitz, R. Westphalen, U. Niggebrugge, K. Schneider, and P. Balk, "Selective embedded growth of GaInAs by low pressure MOVPE," *J. Crystal Growth*, vol. 107, pp. 141-146, 1991.
16. K. Shimoyama, M. Katoh, M. Noguchi, Y. Inoue, H. Gotoh, Y. Suzuki, and T. Satoh, "Transverse junction buried hetero-structure (TJ-BH) laser diode grown by MOVPE," *J. Crystal Growth*, vol. 93, pp. 803-808, 1988.
17. K. Shimoyama, Y. Inoue, M. Katoh, H. Gotoh, Y. Suzuki, and H. Yajima, "A new selective MOVPE regrowth process utilizing in-situ vapor phase etching for optoelectronic integrated circuits," *J. Crystal Growth*, vol. 107, pp. 767-771, 1991.
18. W. Tong, V. Menon, F. Xia and S. R. Forrest, "An asymmetric twin-waveguide, 8 channel polarization independent arrayed waveguide grating with an integrated photodiode array," *IEEE Photon. Technol. Lett.*, Vol. 16, pp. 1070-1072, 2004.
19. R. L. Thornton, W. J. Mosby, and T. L. Paoli, "Monolithic waveguide coupled cavity lasers and modulators fabricated by impurity induced disordering," *IEEE J. Lightwave Technol.*, vol. 6, no. 6, pp. 786-792, 1988.
20. V. Aimez, J. Beauvais, J. Beerens, D. Morris, H. Lim, and B. Ooi, "Low-energy ion-implantation-induced quantum-well intermixing," *IEEE J. Select. Topics Quantum Electron.*, vol. 8, pp. 870-879, 2002.
21. J. Dubowski, Y. Feng, P. Poole, M. Buchanan, S. Poirier, J. Genest, and V. Aimez,

- “Monolithic multiple wavelength ridge waveguide laser array fabricated by Nd:YAG laser induced quantum well intermixing,” *J. Vac. Sci. Technol. A*, vol. 20, pp. 1426-1429, 2002.
22. A. McKee, C. J. Mclean, G. Lullo, A. C. Bryce, R. M. De La Rue, J. H. Marsh, and C. C. Button, “Monolithic integration in InGaAs/InGaAsP multiple-quantum-well structures using laser intermixing,” *IEEE J. Quantum Electron.*, vol. 33, pp. 45-55, 1997.
23. O. Kowalski, C. Hamilton, S. McDougall, J. Marsh, A. Bryce, R. De la Rue, B. Vogele, C. Stanley, C. Button, and J. Robert, “A universal damage induced technique for quantum well intermixing,” *Appl. Phys. Lett.*, vol. 72, pp. 581-583, 1998.
24. E. Skogen, J. Barton, S. DenBaars, and L. Coldren, “Tunable sampled-grating DBR lasers using quantum-well intermixing,” *IEEE Photon. Technol. Lett.*, vol. 14, pp. 1243-1245, 2002.
25. V. Aimez, J. Beauvais, J. Beerens, S. Ng, and B. Ooi, “Monolithic intra-cavity laser-modulator device fabrication using post growth processing of 1.55 $\mu$ m heterostructure,” *Appl. Phys. Lett.*, vol. 79, pp. 3582-3584, 2001.
26. D. Hofstetter, B. Maisenholder, and H. P. Zappe, “Quantum-well intermixing for fabrication of lasers and photonic integrated circuits,” *IEEE J. Select. Topics Quantum Electron.*, vol. 4, pp. 794-802, 1998.

27. N. Shimada, Y. Fukumoto, M. Uemukai, T. Suhara, H. Nishihara and A. Larsson, "Monolithic integration of laser and passive elements using selective QW disordering by RTA with SiO<sub>2</sub> caps of different thicknesses," IEEE J. Select. Topics Quantum Electron., vol. 7, pp. 350-354, 2001.
28. M. Aoki, H. Sano, M. Suzuki, M. Takahashi, U. Uomi and A. Takai, "Novel structure MQW electro-absorption modulator/DFB-laser integrated device fabricated by selective area MOCVD growth," Electron. Lett., vol. 27, no. 23, pp. 2138-2139, 1991.
29. D. Delprat, A. Ramdane, L. Silvestre, A. Ougazzaden, F. Delorme, and S. Slempek, "20-Gb/s integrated DBR laser-EA modulator by selective area growth for 1.55 $\mu$ m WDM applications," IEEE Photon. Technol. Lett., vol. 9, pp. 898-900, 1997.
30. T. Sasaki, M. Yamaguchi, and M. Kitamura, "Monolithically integrated multi-wavelength MQW-DBR laser diodes fabricated by selective metal-organic vapor phase epitaxy," J. Crystal Growth, vol. 145, pp. 846-851, 1994.
31. K. Hamamoto, and K. Homatsu, "Insertion-loss-free 2x2 InGaAsP/InP optical switch fabricated using bandgap energy controlled selective MOVPE," Electron. Lett., vol. 31, pp. 1179-80, 1995.
32. Y. Suematsu, M. Yamada, and K. Hayashi, "Integrated Twin-Guide AlGaAs laser with multi-heterostructures," IEEE J. Quantum Electron., vol. 11, pp. 457-460, 1975.

33. H. Kawanishi, Y. Suematsu, and K. Kishino, "Ga-Al<sub>x</sub>Ga<sub>1-x</sub>As integrated twin-guide lasers with distributed Bragg reflectors," *IEEE J. Quantum Electron.*, vol. 13, pp. 64-65, 1977.
34. T. Tanbunek, S. Arai, F. Koyama, K. Kishino, S. Yoshizawa, T. Watanabe, Y. Suematsu, "Low threshold current CW operation of GaInAsP/InP buried hetero-structure distributed Bragg-reflector integrated-twin-guide laser emitting at 1.5-1.6 $\mu$ m," *Electron. Lett.*, vol. 17, pp. 967-968, 1981.
35. L. Xu, M. R. Gokhale, P. V. Studenkov, J. C. Dries, C. -P. Chao, D. Garbuzov, and S. R. Forrest, "Monolithic integration of an InGaAsP-InP MQW laser/waveguide using a twin-guide structure with a mode selection layer," *IEEE Photon. Technol. Lett.*, vol. 9, pp. 569-571, 1997.
36. P. V. Studenkov, M. R. Gokhale, J. C. Dries, and S. R. Forrest, "Monolithic integration of a quantum well laser and an optical amplifier using an asymmetric twin-waveguide structure," *IEEE Photon. Technol. Lett.*, vol. 10, pp. 1088-1090, 1998.
37. A. Yariv, *Optical electronics in modern communications*, Oxford University Press, New York, 1997.
38. Rsoft Inc., Ossining, NY 10562.
39. V. Vusirikala, S. S. Saini, R. E. Bartolo, S. Agarwala, R. D. Whaley, F. G. Johnson, D.

- R. Stone, and M. Dagenais, "1.55 $\mu\text{m}$  InGaAsP-InP laser arrays with integrated-mode expanders fabricated using a single epitaxial growth," *IEEE J. Select. Topics Quantum Electron.*, vol. 3, pp. 1332-1343, 1997.
40. S. S. Saini, V. Vusirikala, R. D. Whaley, F. G. Johnson, D. R. Stone, and M. Dagenais, "Compact mode expanded lasers using resonant coupling between a 1.55 $\mu\text{m}$  InGaAsP tapered active region and a underlying coupling waveguide," *IEEE Photon. Technol. Lett.*, vol. 10, pp. 1232-1234, 1998.
41. K. Kawano, M. Kohtoku, M. Wada, H. Okamoto, Y. Itaya, and M. Naganuma, "Design of a spotsize-converter-integrated laser diode (SS-LD) with a lateral taper, thin film core and ridge in the 1.3 $\mu\text{m}$ -wavelength region based on the 3-D BPM," *IEEE J. Select. Topics Quantum Electron.*, vol. 2, pp. 348-354, 1996.
42. D. Marcuse, *Theory of dielectric optical waveguides*, Chapter 4, Academic Press, New York, 1974.
43. T. Bakke, C. T. Sullivan, and S. D. Mukherjee, "Polymeric optical spot-size transformer with vertical and lateral tapers," *J. Lightwave Technol.*, vol. 20, pp. 1188-1197, 2002.
44. G. A. Vawter, R. E. Smith, H. Hou, and J. R. Wendt, "Semiconductor laser with tapered-rib adiabatic-following fiber coupler for expanded output-mode diameter," *IEEE Photon. Technol. Lett.*, vol. 9, pp 425-427, 1997.

45. J. D. Love and W. M. Henry, "Quantifying loss minimization in single-mode fiber tapers," *Electron. Lett.*, vol. 22, pp. 912-914, 1986.
46. W. H. Louisell, "Analysis of the single tapered mode coupler," *Bell Syst. Tech. J.*, vol. 34, pp. 853-870, 1955.

### **Figure Captions**

Fig. 1: Techniques for monolithic integration illustrated by the example of laser/waveguide integration. (a) Material regrowth: different optical functions are created by sequential material removal and growth in different regions of the wafer. (b) Quantum well intermixing: blue shift the MQW region absorption edge by impurity or defect assisted atomic inter-diffusion between the wells and barriers at a high annealing

temperature. (c) Selective-area growth: varying the local material growth rates hence the transition energy of the MQWs by changing the width of the pre-patterned dielectric masks before material growth. (d) Twin-waveguide: different optical functions are separated into vertically displaced waveguides and the integration is realized by selective removal of the unwanted upper waveguides.

Fig. 2: (a) A generic twin waveguide structure and its waveguiding index profile. (b) Index and normal mode profiles of a nearly symmetric twin waveguide structure. Here,  $\phi_o/\phi_e$  is the odd/even mode profile of the twin waveguide structure.

Fig. 3: A basic symmetric twin waveguide integrated laser/waveguide device. R is the etched facet reflectivity and T is the output transmission efficiency.

Fig. 4: (a) Refractive index and mode profiles of an ATG structure without taper couplers.  $\Gamma_{QW(e)}/\Gamma_{QW(o)}$ : quantum well confinement factors of even/odd modes. (b) A generic structure of an ATG semiconductor optical amplifier (SOA).  $E_{in}/E_{out}$  is the input/output optical field of the ATG semiconductor optical amplifier. L is the length of the ATG semiconductor optical amplifier.

Fig. 5: Schematic structure of an ATG laser with taper coupler. Left: optical mode in passive waveguide. Right: optical mode in untapered twin-waveguide section. Here,  $W_i/W_f$  is the tip/base width of the taper coupler.  $L_{taper}$  is the length of the taper coupler.

Fig. 6: A three-dimensional schematic view of an ATG photodiode and its index profile of

the epitaxial structure.

Fig. 7: (a) Calculated scattering intensity versus taper coupler width in the ATG photodiode for different asymmetries (85:15 and 95:05) between fiber and coupling waveguide. (b) Taper shapes generated using the calculated intensity in (a).

Fig. 8: Power transfer efficiency from fiber to coupling waveguides versus the taper length for different asymmetries (85:15 and 95:05) and taper shapes (Optimized and two-section linear) in ATG photodiodes.

Fig. 9: Power transfer efficiency from the fiber to coupling waveguide versus the taper width variations for different designed fabrication tolerance.

Fig. 10: (a) 3-D perspective view of an odd mode taper coupler. (b) Refractive index profile of the odd mode taper coupler epitaxial structure.  $W_i/W_f$  is the tip/base width of the odd mode taper coupler.

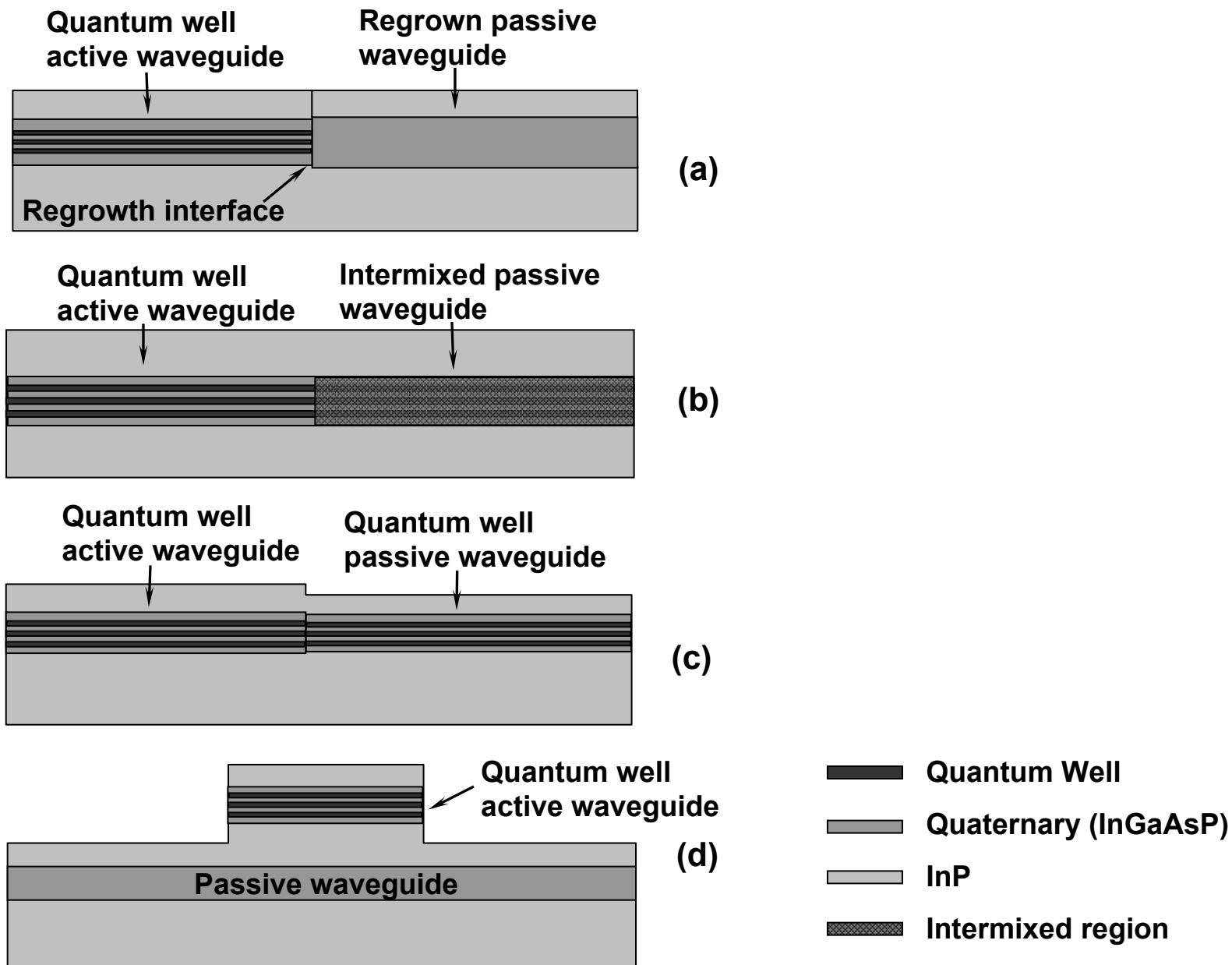


Fig. 1, XIA et al.

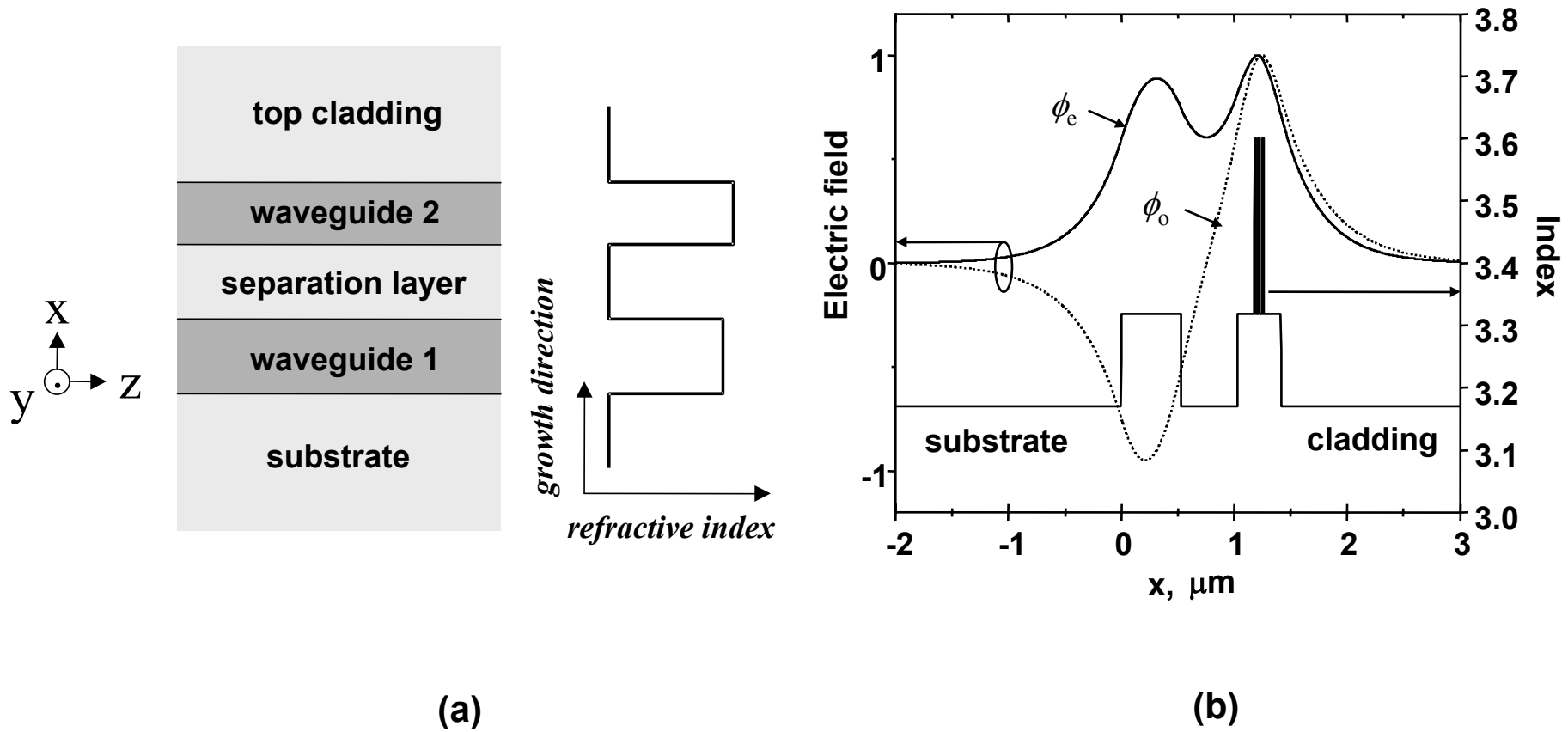


Fig. 2, XIA et al.

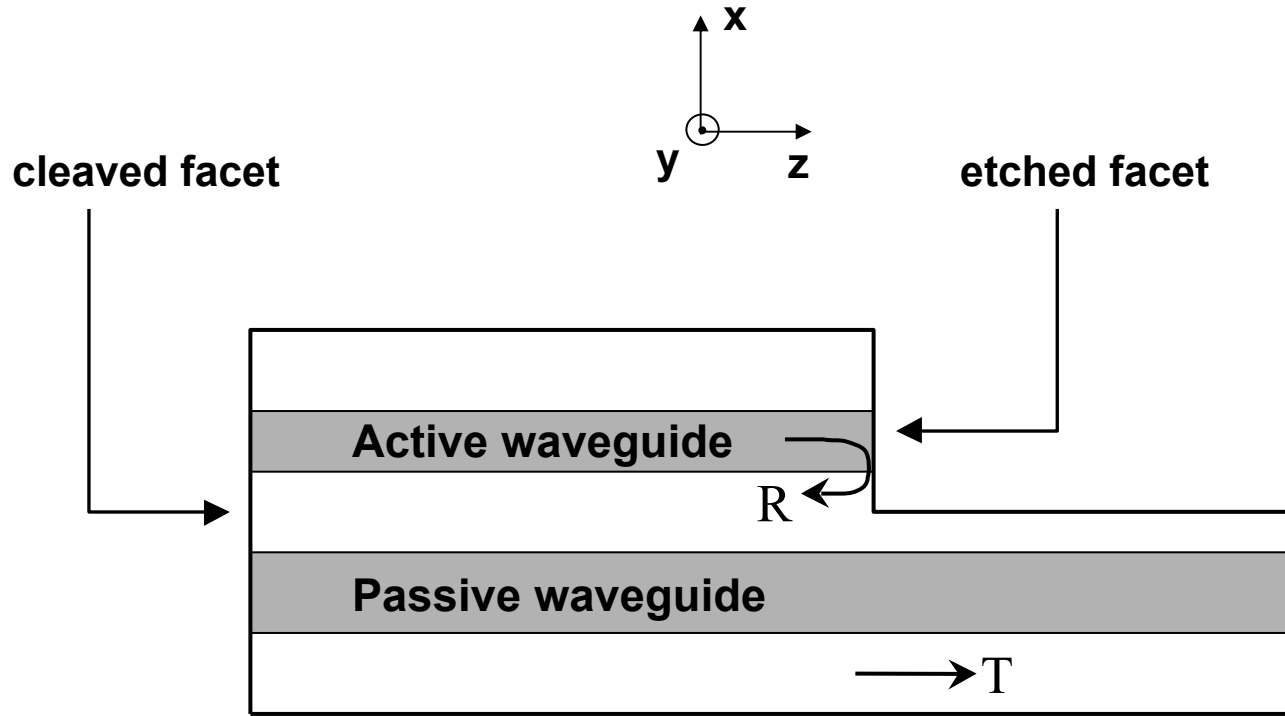
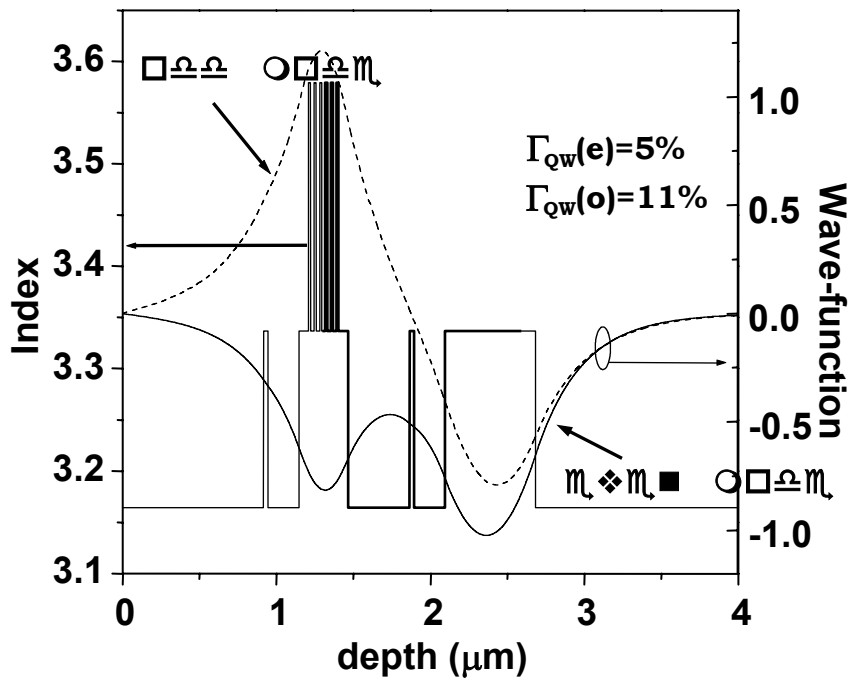
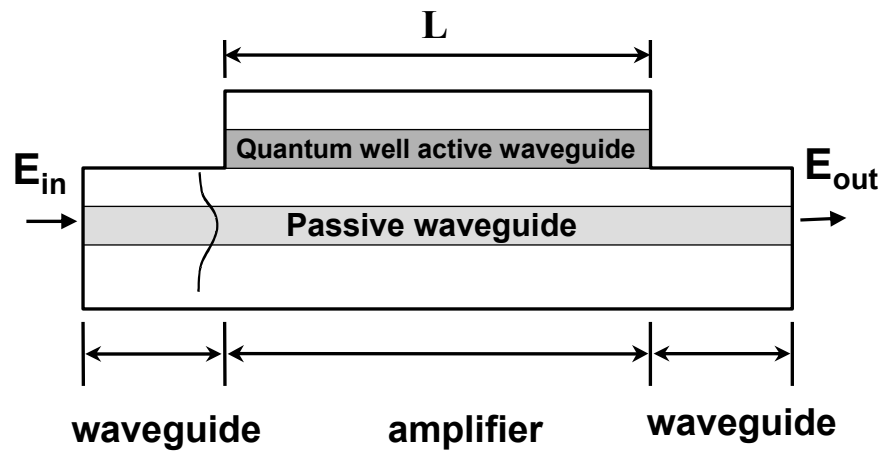


Fig. 3, XIA et al.



(a)



(b)

Fig. 4, XIA et al.

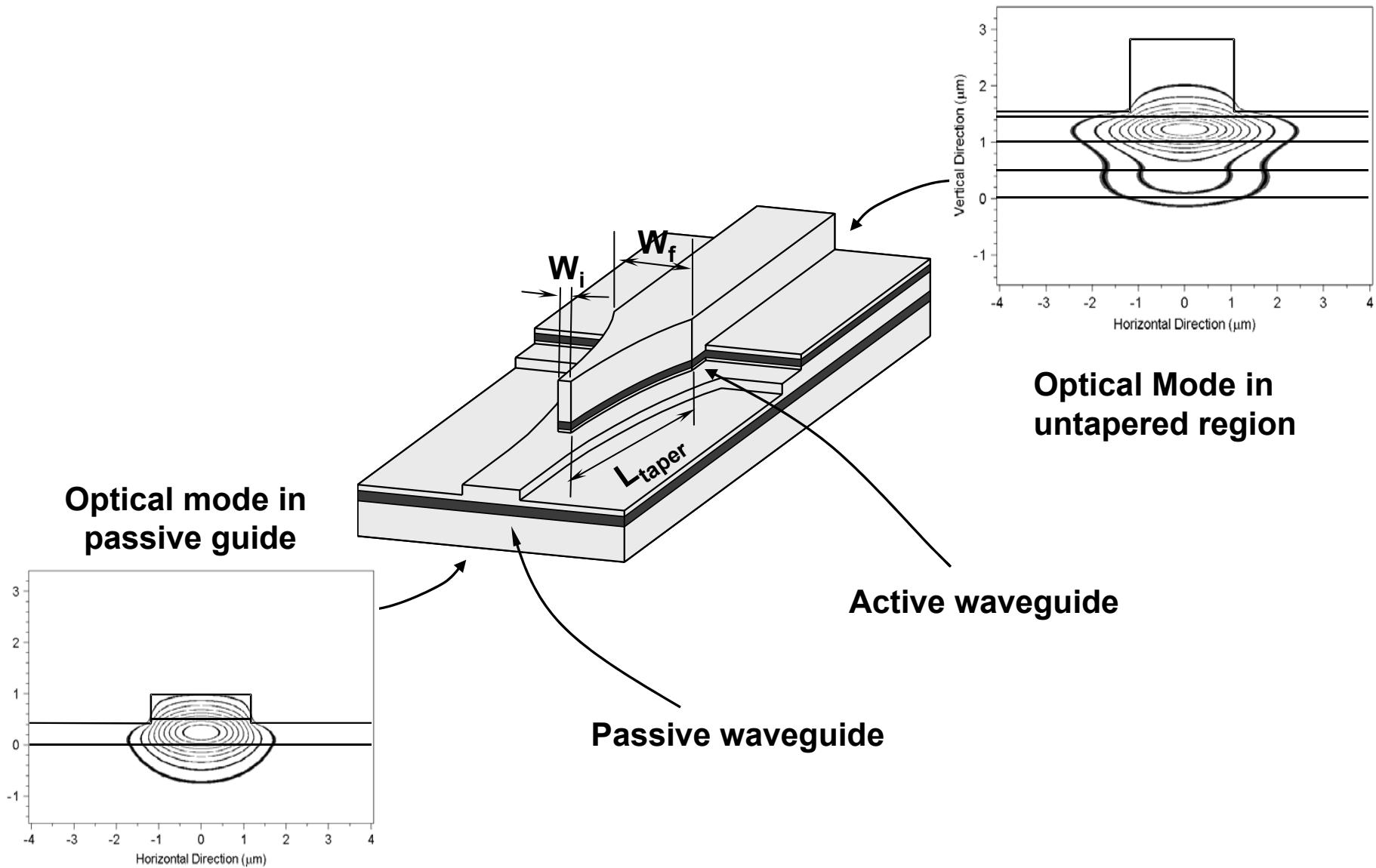


**Fig. 5, XIA et al.**

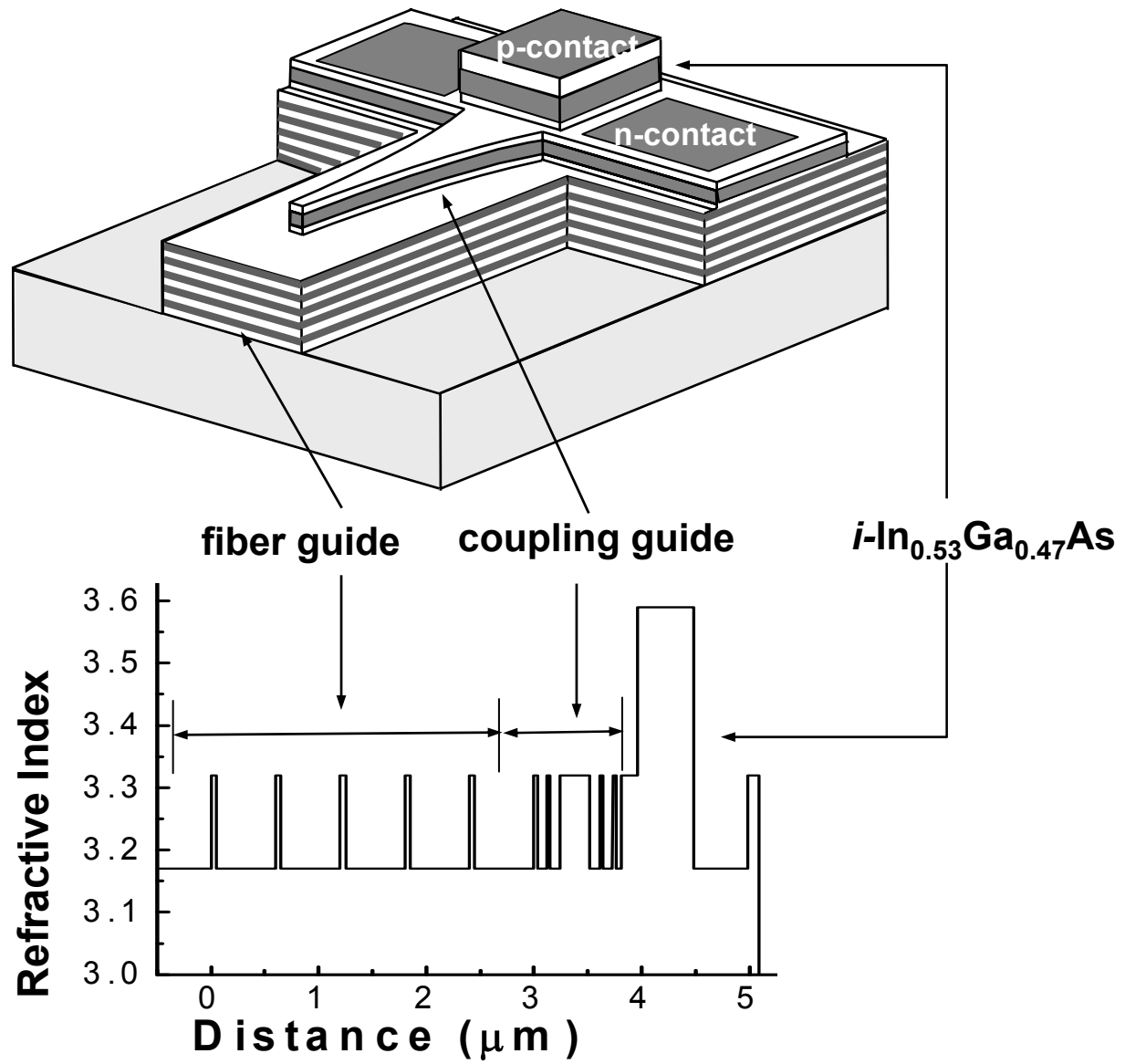
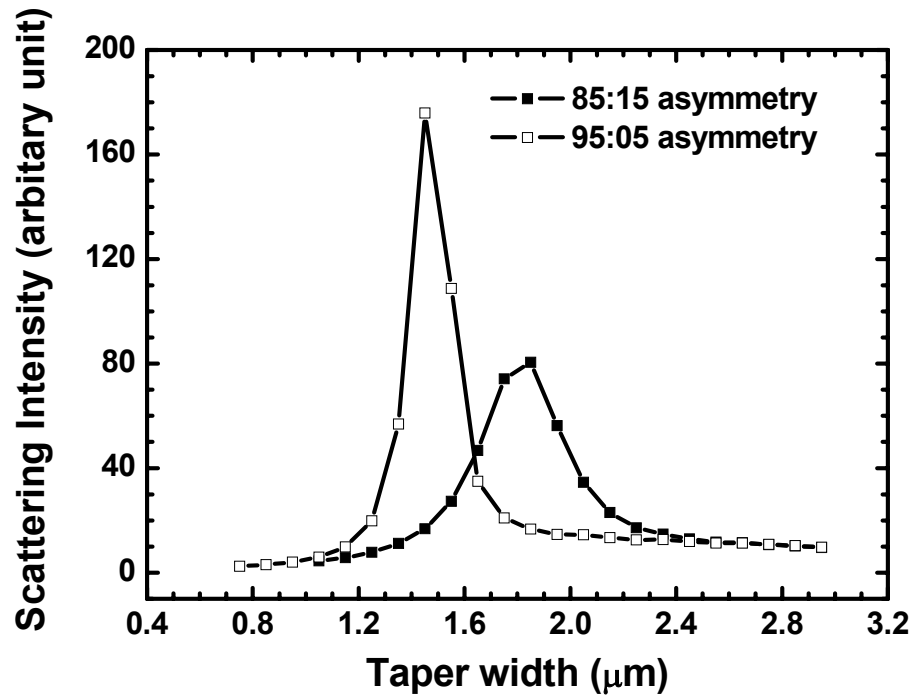
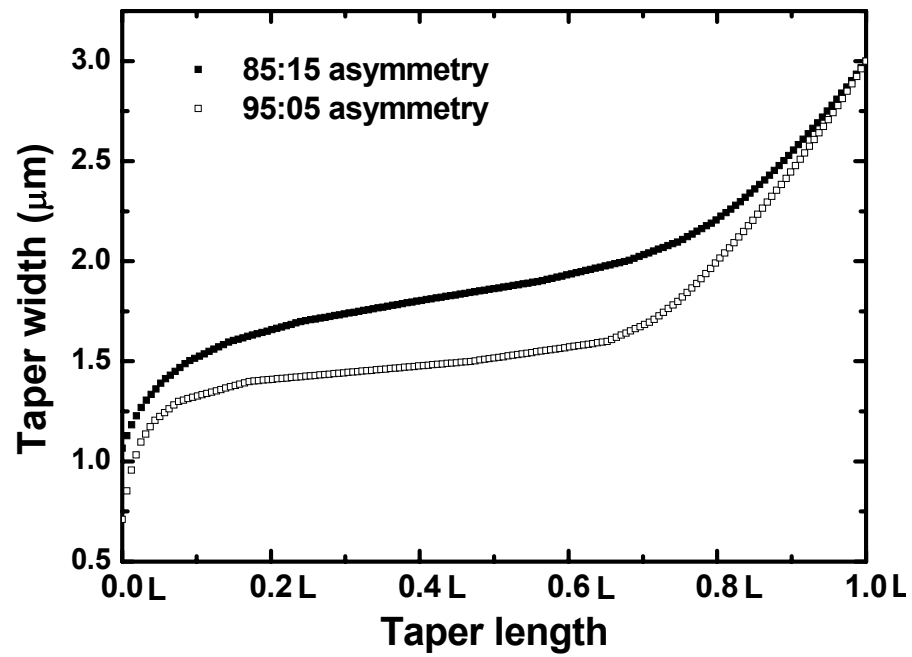


Fig. 6, XIA et al.



(a)



(b)

Fig. 7, XIA et al.

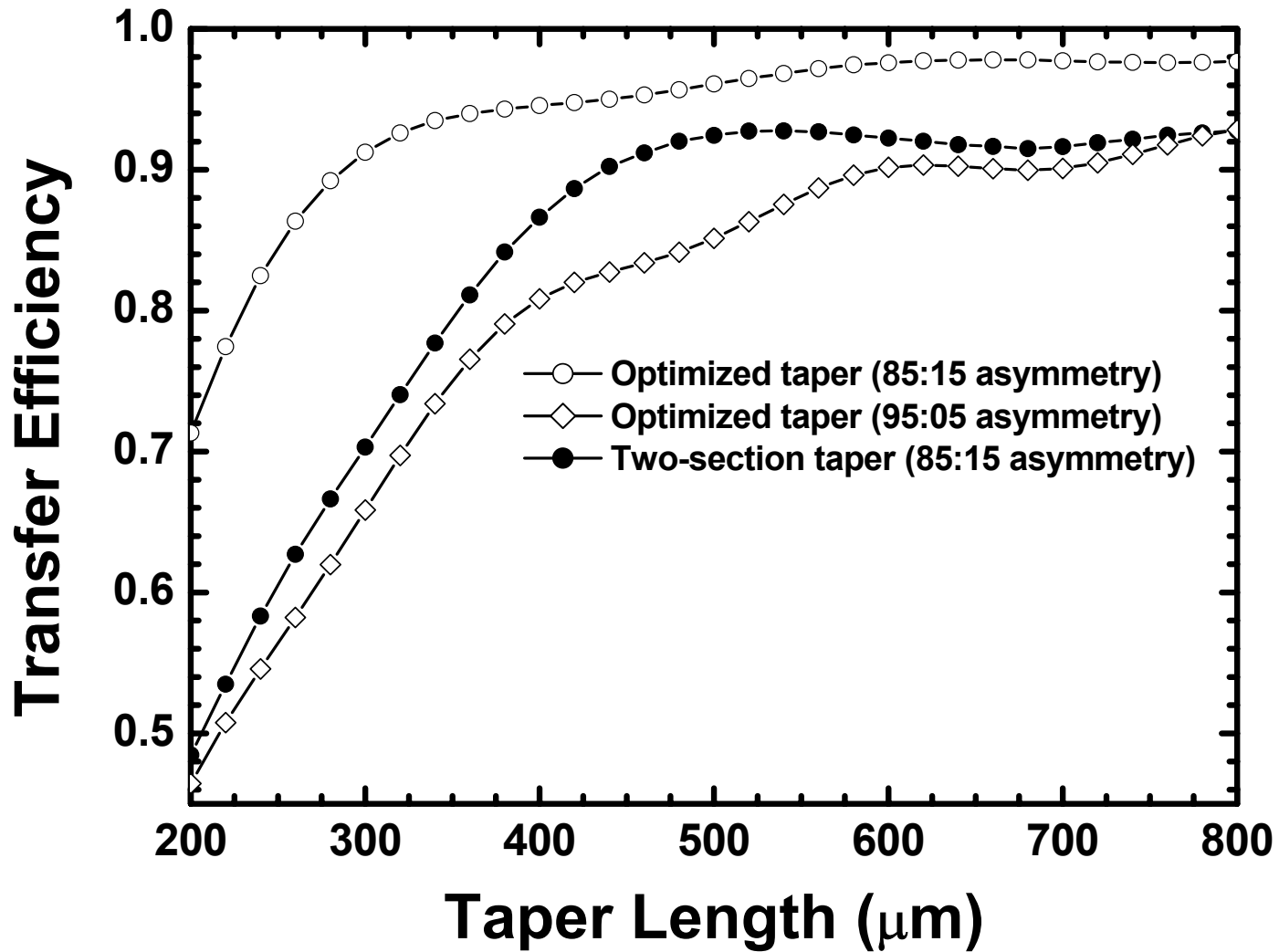


Fig. 8, XIA et al.

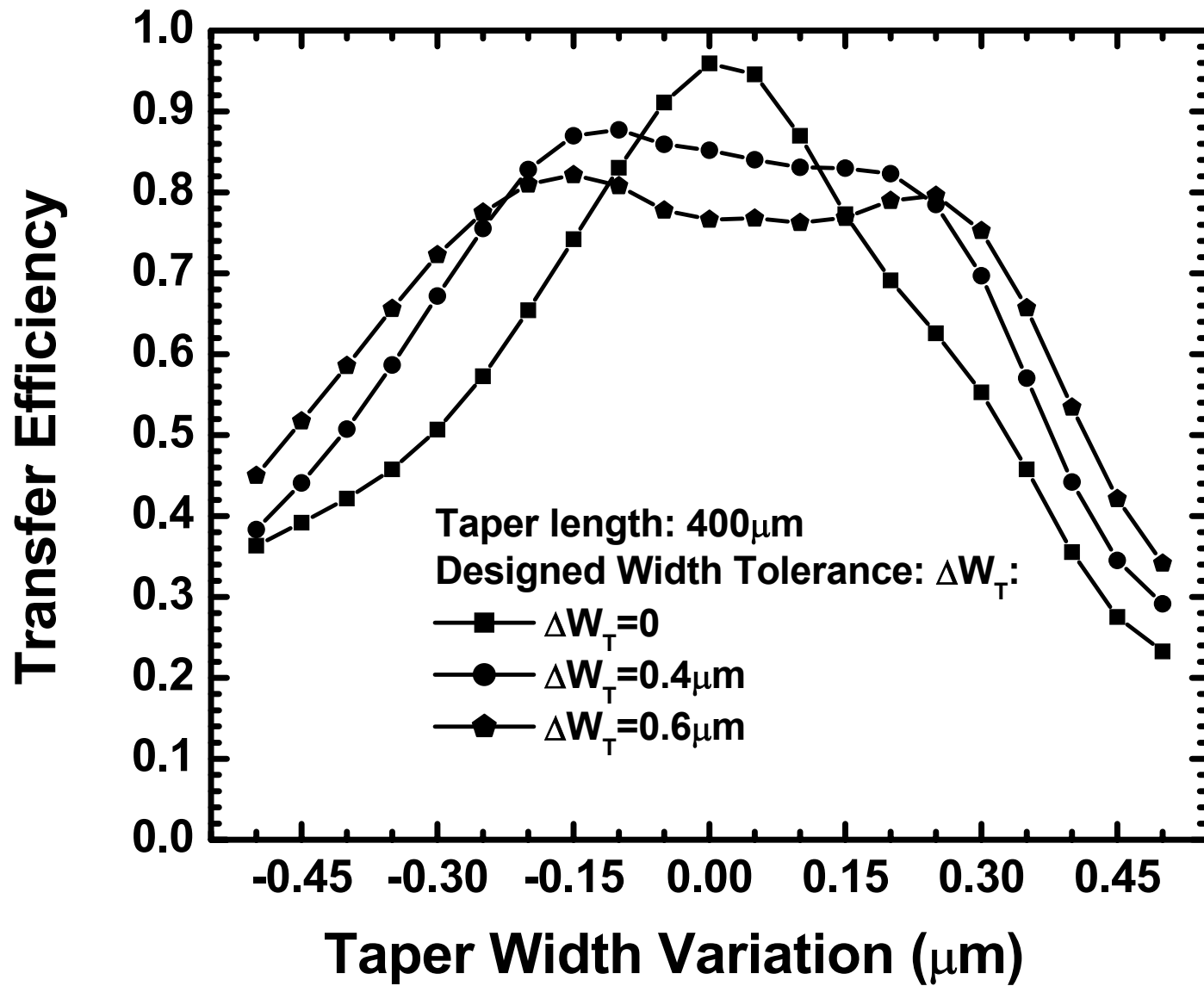
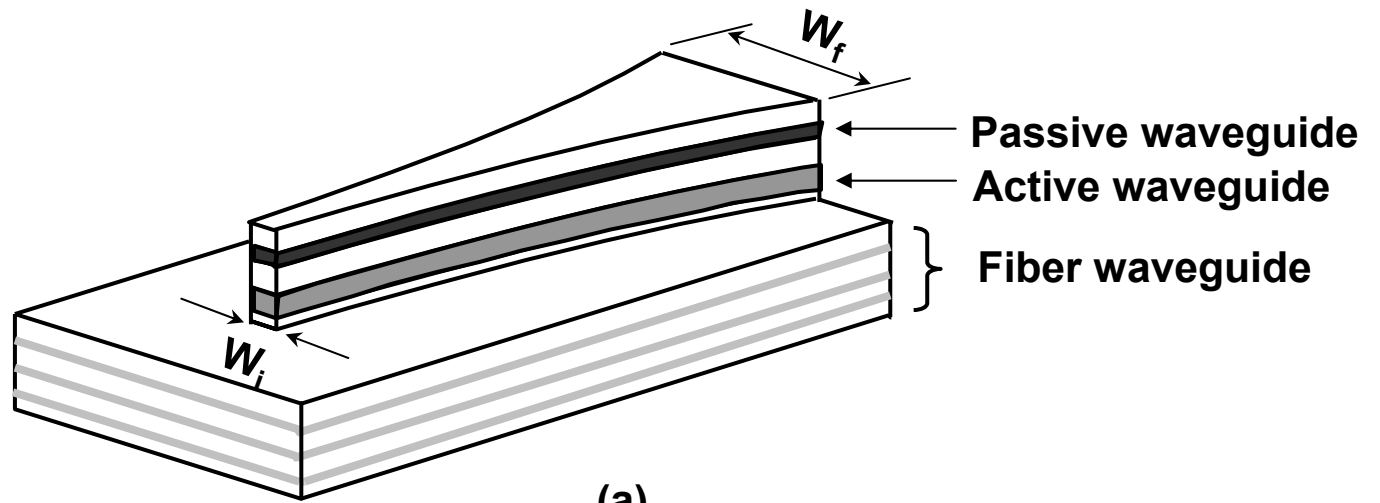
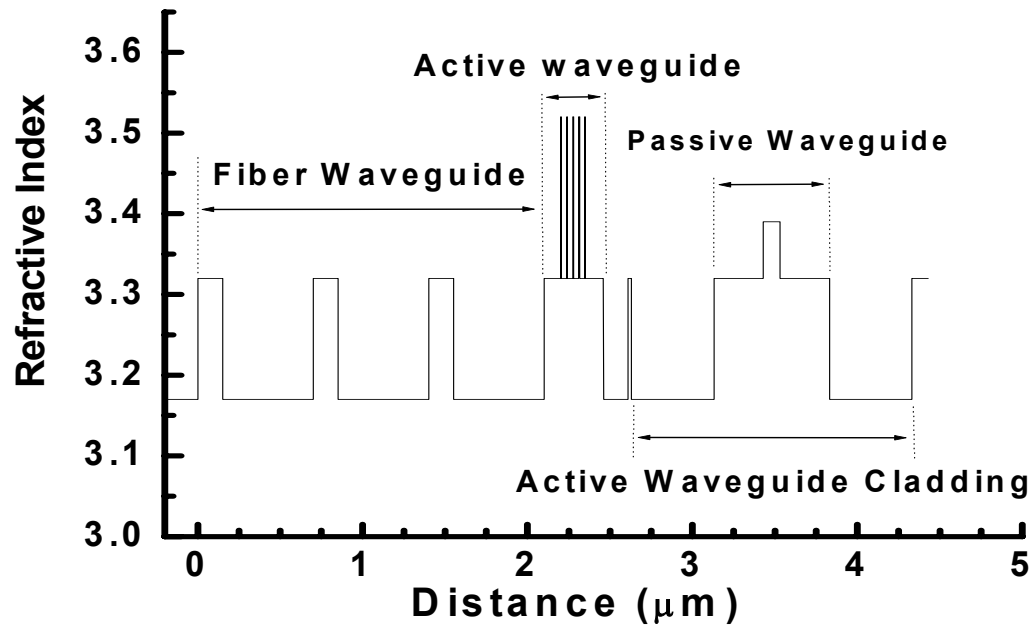


Fig. 9, XIA et al.



(a)



(b)

Fig. 10, XIA et al.

# **Photonic integration using asymmetric twin-waveguide (ATG) technology.**

## **II. Devices**

Vinod M. Menon, Fengnian Xia, and Stephen R. Forrest\*

Princeton Institute for the Science and Technology of Materials (PRISM)

Department of Electrical Engineering, Princeton University

Princeton, NJ 08544

**Abstract**---Asymmetric twin waveguide technology has been shown to be a versatile and high performance platform for the integration of a wide range of photonic integrated circuits. Following the conceptual and theoretical description in Paper I [F. Xia, et al, IEEE J Select. Topics Quantum Electron., vol. , pp. yy-zz, 2005], here we discuss several archetype asymmetric twin waveguide-based photonic integrated devices and circuits. We present results on the three basic device classes that span the entire range of photonic component needs: light emitters, detectors, and light transporting devices (e.g. waveguides) that have been realized using the twin waveguide platform. Specifically, we discuss Fabry-Perot and wavelength tunable lasers, high-bandwidth p-i-n photodiodes, a polarization insensitive arrayed waveguide grating receiver with integrated p-i-n photodiodes, as well as combinations of functions including integrated electro-absorption modulated lasers, and a semiconductor optical amplifier integrated with a p-i-n photodiode. Finally, we address potential integration challenges and novel applications of the asymmetric twin waveguide scheme, and avenues for improvement.

**Keywords:** photonic integrated circuit, laser, detector, waveguide, modulator, monolithic integration

---

\* Email: forrest@princeton.edu

## **I. Introduction**

As discussed in the previous paper (Paper I, [1]), chip-scale multifunctional photonic integrated circuits (PICs) are essential for reducing cost, and for realizing high component performance required in modern optical data transmission and telecommunication systems. Until recently, a major impediment to the rapid development of integrated photonic systems has been the difficulty of integrating multiple, high performance photonic functions on a chip at low cost. This has led to high chip costs and long design cycles, typically extending two years between device conception and realization. The situation has dramatically changed with the demonstration of asymmetric twin waveguide (ATG) photonic integration technology whose conceptual design principles were described in Paper I [1].

In an ATG structure, various photonic device functions are realized in vertically displaced waveguides that are separately optimized for light emission, light transport, or detection. The light is efficiently (in some cases >95%) coupled between the guide layers using lateral tapered mode transformers. The waveguide with the lowest effective refractive index forms the lowermost guide, and the one with the largest effective refractive index, the uppermost. The light path through the PIC is confined transverse to the propagation direction by a ridge waveguide, and in the vertical direction, by tapers. A scanning electron micrograph of a typical linear taper along with the calculated power transfer efficiency is shown in Fig. 1. Here, the fabrication tolerant taper design follows the method discussed in Ref. [1], and the calculation follows conventional beam propagation based simulations using a commercial package<sup>1</sup>.

---

<sup>1</sup> BeamPROP from Research Software (Rsoft) Inc., Ossining, NY 10562.

Due to their vertical displacement, the photolithographically defined active and passive devices residing in the separate waveguide regions can be independently optimized to achieve high performance for every component comprising the PIC. The post-growth fabrication steps determine the location and type of devices on the PIC. This is in contrast to the expensive and complicated processing and regrowth iterations currently used in conventional PIC fabrication [2-7]. Table 1 summarizes various devices and their performances that have been demonstrated to date based on ATG integration. The versatility and simplicity of this scheme is evident from the diversity of the devices that have already been realized, forming, for the first time, a fully compatible family of integrated components. Like CMOS integration of Si-based electronics, ATG opens up the possibility of designing PICs through a standardized library of components, all fabricated by a common process sequence using a standardized epitaxial structure.

Here, we discuss the fabrication and performance of a few example archetype ATG-based integrated devices. The paper is organized as follows: In Sec. II we discuss the growth and fabrication of ATG devices. Section III considers several light emitters, detectors, and waveguiding devices. In Sec. IV some archetype multifunctional PICs that have been demonstrated using the ATG scheme will be discussed. Finally, in Sec. V we address several of the challenges currently facing ATG-based integration, and consider future directions that the technology may take. Conclusions are found in Sec VI.

## **II. Growth and Fabrication of ATG structures**

Although not limited to any particular materials system, all ATG based devices demonstrated to date have been fabricated on InP substrates and are based on InGaAs(P)

epitaxial structures. The growth sequence of a typical ATG based laser/waveguide structure is as follows: First the passive waveguide, which has a low effective refractive index, is grown. Passive guides usually consist of thin InGaAsP (with a bandgap cutoff wavelength of  $\lambda_g < 1.3\mu\text{m}$ ) layers interspersed between InP layers. These dilute “fiber” waveguides are single mode despite their large cross section due to their low effective refractive index, and support an approximately circular mode that allows for low-loss, position-tolerant fiber coupling. The cross section of a typical fiber guide, along with its far field pattern, is shown in Fig. 2. Following the passive guide, a 0.5  $\mu\text{m}$  thick transparent InP spacer is followed by growth of the active guide. The active guide consists of multiple quantum wells or a single composition layer (InGaAsP,  $\lambda_g = 1.55\mu\text{m}$ ) that is used as an optical gain medium. For operation at a wavelength of  $\lambda = 1.55\mu\text{m}$ , the epitaxial layer structure of the active waveguide is typically comprised of compressively strained, 13.5nm thick InGaAsP ( $\lambda_g = 1.55\mu\text{m}$ ) quantum wells separated by 23nm thick InGaAsP ( $\lambda_g = 1.2\mu\text{m}$ ) barriers sandwiched between two, 120nm thick InGaAsP ( $\lambda_g = 1.2\mu\text{m}$ ) separate confinement layers. Finally, a 1 $\mu\text{m}$ -thick InP upper cladding layer is grown, followed by a 0.15 $\mu\text{m}$ -thick InGaAsP ( $\lambda_g = 1.2\mu\text{m}$ ) contact layer. The refractive index profile of a semiconductor optical amplifier (SOA) structure is shown in Fig. 3(a). Very thin ( $\sim 30\text{ nm}$ ) InGaAsP etch stop layers are inserted to achieve precise and controlled etch depths needed for high yield device processing. Figure 3(b) is a scanning electron micrograph showing the epitaxial layers of a typical ATG laser/SOA integrated with a fiber guide grown using gas source molecular beam epitaxy [8].

For structures containing optical detection functionality, a high refractive index coupling guide is grown onto the surface of the fiber guide. Again, a 0.5 $\mu\text{m}$  thick

transparent InP layer separates these two guides. The coupling guide consists of two thin (30 nm) InGaAsP ( $\lambda_g = 1.2\mu\text{m}$ ) layers interspersed with 90 nm-thick InP layers grown on both sides of a central InGaAsP ( $\lambda_g = 1.2\mu\text{m}$ ) layer with a thickness of  $0.28\mu\text{m}$ . After growing the coupling guide layers, an index matching layer followed by the undoped  $0.53\mu\text{m}$ -thick  $\text{In}_{0.53}\text{Ga}_{0.47}\text{As}$  absorption region are grown. The top  $0.3\mu\text{m}$  of the coupling guide is doped with Si to form the  $n$ -metal contact. A  $0.5\mu\text{m}$  thick InP cladding layer and a  $0.1\mu\text{m}$  thick InGaAsP ( $\lambda_g = 1.2\mu\text{m}$ ) contact layer, both doped with Be, cap the  $\text{In}_{0.53}\text{Ga}_{0.47}\text{As}$  absorption layer to make the  $p$ -ohmic contact.

It is possible to grow the detector layer on top of the laser structure, thereby having light emission, detection and transport all within the same structure. The ATG-based SOA/p-i-n structure that will be discussed in Sec. IV is one such device that includes all three of these photonic functionalities.

The epitaxial growth sequence for the various ATG structures is generic, and hence is suitable for scale-up in a standardized growth foundry. Analogous to electronic integration, the functionality desired of the PIC is then defined through post-growth processing and patterning. Indeed to maintain a high yield, equally standardized fabrication process, patterning occurs through a straightforward sequence of conventional dry and wet etching, metalization and lithographic steps.

For example, to fabricate a light emitter + waveguide structure, for example, the wafer undergoes the series of processing steps shown schematically in Fig. 4(a). The wafer is first coated with a thick layer ( $\sim 300\text{ nm}$ ) of  $\text{SiN}_x$  using plasma enhanced chemical vapor deposition. Following this, the shallow ridge is photolithographically defined and patterned using reactive ion etching (RIE) in  $\text{CH}_4:\text{H}_2$  (1:7) and subsequent

wet chemical etching in HCl:H<sub>3</sub>PO<sub>4</sub> (3:1) with SiN<sub>x</sub> as the mask. The next lithography step defines the deep-etched ridge, and finally the fiber waveguide is defined. The wafer is then planarized using silicon nitride (SiN<sub>x</sub>), and a short etch-back is performed to open up the active ridge and the taper. Ti/Ni/Au (300/500/1500Å) *p*-contacts and Ge/Au/Ni/Au (270/450/215/1200Å) *n*-contacts are deposited using electron-beam evaporation, followed by a lift-off process. The *p*-metal is annealed at 415<sup>0</sup>C for 30s, and the *n*-metal at 360<sup>0</sup>C for 90s in a rapid thermal annealer. The wafer is thinned by lapping to ~ 125 μm before depositing the *n*-metal.

In the case of detectors, the fabrication steps are shown in Fig. 4(b): first, a Au–Zn *p*-contact metal is deposited and patterned using photolithographic lift off. After annealing, the *p*-contact metal is used as a mask for dry etching in a CH<sub>4</sub>:H<sub>2</sub> (1:7) mixture to form the diode ridge. A 3000-Å-thick SiN<sub>x</sub> layer is then deposited, and the tapered coupling guide is defined by contact photolithography. Reactive ion etching using a 3000-Å-thick SiN<sub>x</sub> layer as a mask forms the tapered coupling guide. After etching, the SiN<sub>x</sub> is removed using a dilute solution of 1 HF:10 H<sub>2</sub>O, and a new 3000-Å thick-SiN<sub>x</sub> layer is deposited. The fiber guide is then similarly etched. After definition of the fiber guide, bis-benzocyclobutene (BCB) cured at 250<sup>0</sup>C for 60min is used for planarization. The BCB is dry etched for the *n*-contact metal (Ge–Au–Ni–Au). A final metallization forms the 50Ω coplanar transmission lines for high frequency coupling.

### **III. Archetype photonic building blocks**

A fully capable integration technology that can span the range of possible applications must allow for high performance devices to be monolithically integrated in all three fundamental photonic device functions: light emission, detection and waveguiding. The

ATG platform represents such a *complete* integration technology by implementing each generic function in vertically stacked and separately optimized material layers, with efficient optical coupling between the layers effected by lateral taper optical mode transformers. In this section, we describe device structures and typical performance parameters for each of these three “library” functions.

### **III.A. Light emitters**

Asymmetric twin waveguide laser structures have demonstrated rapid progress in performance since the first demonstration of a simple ATG Fabry-Perot (FP) laser [9]. More recently, ATG-based lasers with distributed Bragg reflector (DBR) mirrors [10], distributed feedback (DFB) lasers [11], electroabsorption modulated lasers (EML) [11], and tunable lasers [12] have also been demonstrated.

A schematic of an ATG FP laser is shown in lower right of Fig. 5. In the absence of significant taper losses, the laser cavity lies between the rear, cleaved facet, and the facet formed by cleaving the front face of the waveguide leading to the edge of the chip. The performance of taper couplers was thus evaluated by comparing the ATG lasers integrated with waveguide segments to FP lasers produced by cleaving off both the waveguides and tapers. Figure 5 shows the light output-versus-current (L-I) characteristics of two such devices before and after cleaving (upper left, Fig. 5). In both cases, the slope efficiency of the laser did not change, and there was only a small drop in the threshold current ( $\sim 5\%$ ) on cleaving. Assuming that the cleaved-facet reflectivities of the FP laser and the waveguide mirror are equal, we conclude that the additional loss in

the integrated device due to the taper coupler and waveguide propagation losses are negligible.

Shown in the inset in Fig 5 is an infrared image of the near field pattern at the output, with and without the taper. In the presence of the taper coupler, no significant light emission is observed at its tip, with the emission primarily emerging from the lower, passive waveguide. Integrated lasers with a length of 2.05mm produced output powers of ~35 mW, with 24% slope efficiency per facet. In these devices, the *p*-contact covers only the shallow ridge section of the laser waveguide without extending over the taper, resulting in absorption losses in the quantum wells in the unpumped taper region. Subsequently, it has been demonstrated that absorption losses in the taper can be eliminated by extending the *p*-contact metal over the taper [8], or by the use of quantum well intermixing (QWI) [13]. In this latter case, the absorption peak of the taper region is blue-shifted relative to the laser emission wavelength using QWI along the entire length of the taper.

Single frequency operation is achieved using distributed Bragg reflector (DBR) lasers, characterized by the physical separation of the gain and the grating feedback sections. Here, the Bragg gratings are formed on the surface of the passive waveguide section using either near-field holography with phase masks, or by electron beam lithography, and are optically coupled to the active layer by tapers [10]. Such devices have demonstrated a threshold current of 50 mA (2.65 mm gain region), 11 mW output power, > 40dB side-mode suppression ratio, and a slope efficiency of 0.11 W/A under pulsed operation [10].

A schematic of a wavelength tunable,  $\lambda=1.55\mu\text{m}$  DBR laser [12] is shown in Fig. 6. It consists of a  $\sim 1\text{mm}$  long, current-tunable grating section, a phase section to eliminate mode hops, two taper couplers on both ends of the active gain region, and a short, front facet-grating. Here, tuning occurs through the refractive index change induced by plasma loading in the presence of charge injection [14]. Helium ion-implantation provides electrical isolation between the tunable grating, phase, and active ridge sections. Using AZ4620 resist as an implantation mask, He ions with a total dose of  $9 \times 10^{13} \text{ cm}^{-2}$  are implanted at 28, 50, 75, and 120 keV to create a uniform ion distribution between the top of the passive shallow ridge and the undoped InGaAsP in the passive guide. The threshold current is 50mA, and the slope efficiency is  $(0.12 \pm 0.01) \text{ W/A}$  from the single cleaved facet. Like the fixed frequency DBR laser, the side mode suppression ratio (SMSR) is  $>36\text{dB}$  at an output power of 12.8mW [12]. A very narrow linewidth of  $<150\text{kHz}$  is observed at a grating tuning current equal to zero. This is due to the strong coupling constant ( $\kappa > 30\text{cm}^{-1}$ ) of the gratings along with their extended length along the waveguide surface.

The tuning characteristic of the ATG-DBR laser when both the grating and phase tuning sections are pumped is shown in Fig. 7a. Despite the presence of mode hopping along the contours indicated by solid white lines, the entire wavelength tuning range is accessible due to the gaps at the ends of hopping contours. Hence, tuning around these hops is effected by the appropriate choice of phase and grating section tuning currents.

Figure 7b shows the lasing spectra at different tuning currents, indicating a wavelength blue shift of  $\Delta\lambda=4.8\text{nm}$  (centered at  $\lambda=1.548\mu\text{m}$ ) at 310mA. A nearly 10-fold increase in tuning range is possible by replacing linear with sampled gratings [15]. The

relatively high tuning currents are due to the small overlap between the optical mode in the passive waveguide and the region subject to electrically induced index changes resulting from charge injection via the side-contacts. An alternate and more efficient approach for current injection is via direct, vertical pumping of the gratings. This can be achieved using a single, *blanket overgrowth* of the grating similar to that used to achieve DFB lasers [11] (see Sec. IV.C), resulting in a cladding layer thickness of  $\sim 1\mu\text{m}$  to ensure that the losses due to optical mode coupling to the metal contact are avoided.

Lateral current injection and direct pumping of the overgrown gratings are shown in Fig. 8. While the current densities and the absolute change in index are the same in both cases, the total current required for lateral pumping to achieve the same effective index change as in the direct pumping scheme is greater. This is due to the larger current spreading in the former case. Simulations of current spreading in the lateral pumping scheme indicates that the refractive index change occurs over an area three times larger than for direct pumping. Furthermore, in lateral pumping, there is minimal overlap between the region of high electron concentration and the optical mode (see Fig. 8). Hence, it is estimated that the current required to introduce the same amount of refractive index change decreases by a factor of at least 3 in the direct pumping scheme compared with the laterally pumped grating.

### **III. B. Detectors**

A second archetype function is the integrated photodetector. Two different types of high bandwidth, high responsivity photodiodes have been demonstrated using ATG technology: waveguide coupled p-i-n, and avalanche photodiodes [16,17]. In a p-i-n

photodiode, a single mode, dilute fiber waveguide is used to improve the coupling efficiency and increase the alignment tolerances to the input fiber, as shown in the inset in Fig. 9 [16]. The light in the fiber guide is transferred via the taper coupler into the coupling guide, where it is evanescently coupled into a thick  $\text{In}_{0.53}\text{Ga}_{0.47}\text{As}$  absorption layer grown on top of a thin,  $\text{InGaAsP}$  ( $\lambda_g = 1.2\mu\text{m}$ ) index matching layer.

The lateral p-i-n detector was first reported with a responsivity of  $(0.75\pm 0.03)$  A/W at  $\lambda=1.55\mu\text{m}$ , and a polarization sensitivity of  $\leq 0.4\text{dB}$  [16], with more recent devices showing responsivities of  $\sim 1\text{A/W}$ . The measured frequency response data are shown in Fig. 9, indicating an electrical bandwidth of  $\geq 40\text{GHz}$ . The device had  $< 1\text{dB}$  sensitivity penalty for a fiber-to-waveguide misalignment of  $< \pm 1.1\mu\text{m}$  in the vertical, and  $< \pm 1.3\mu\text{m}$  in the horizontal directions, thereby relaxing tight packaging tolerances typical of edge-couple photodetectors. The responsivity of the ATG p-i-n photodiode is comparable or superior to the best 40GHz waveguide p-i-n photodiodes reported to date [18], while the ATG design provides a simple means of fabrication with the possibility for monolithic integration of the photodiodes with other optical components. One such example is the balanced photodetector (BPD), where a multimode interference (MMI) coupler was integrated with two identical p-i-n photodiodes (see Sec. III.C) [19].

### III. C. Waveguiding Devices

The final basic photonic functionality is light transport. Couplers, splitters and modulators belong to this class of “passive” photonic devices, having a wide array of applications ranging from chip-scale interferometers, to wavelength division multiplexing

systems. Using the ATG integration platform, multimode interference couplers, star couplers, Y-splitters, and microrings have been integrated with p-i-n photodiodes and SOAs [19-22]. A SEM image of a 13.1  $\mu\text{m}$  wide by 750  $\mu\text{m}$  long, 2x2 multi-mode interference (MMI) coupler fabricated using a dilute waveguide integrated with two p-i-n photodiodes is shown in Fig. 10(a). Fig. 10(b) shows the photocurrent detected at both detectors as a function of input optical power, clearly indicating balance to within  $< 0.5$  dB between the two output arms of the MMI [19]. The MMI coupler showed an insertion loss of 2dB, due to scattering from surface roughness, reflection at the output ports, and absorption by free carriers in the case of n-doped waveguides.

More recently, we demonstrated an eight-channel WDM chip that combines an arrayed waveguide grating (AWG) demultiplexer with integrated, high-speed photodetectors at each of the output channels [20]. Given that this represents simply the integration of a detector array with a complex waveguide structure, its growth and fabrication is nearly identical to that used for the BPD+MMI circuit. However, in this case, the dilute AWG waveguide had lower refractive index InGaAsP ( $\lambda_g = 1.05 \mu\text{m}$ ) layers instead of the “conventional” InGaAsP ( $\lambda_g = 1.2 \mu\text{m}$ ) interspersed between the InP layers to minimize birefringence, thereby ensuring polarization independent operation. Figure 11(a) shows the spectral response of the device as measured using the integrated photodetector array. The total loss was 9 dB, comprised of the 5dB fiber-to-chip coupling loss, and 4 dB internal loss. The primary reason for the internal loss is the large spacing (1.05  $\mu\text{m}$ ) between the arrayed waveguides where they meet at the star coupler. Ideally, this spacing can be reduced to  $\sim 0.8 \mu\text{m}$ , which is the limit of resolution of the photomask used in the optical lithographic process employed in the fabrication sequence. But the

topography of the structure with vertically stacked waveguides adds an additional constraint on the maximum achievable resolution using contact lithography, especially in the lower-most waveguide, as is the case in the AWG. This limit can be reduced to 0.5-0.7 $\mu\text{m}$  by using a wafer stepper or electron beam lithography.

The  $\lambda=1.55\mu\text{m}$  wavelength AWG + p-i-n array showed an interchannel crosstalk of  $-16$  dB, a channel non-uniformity of 1.5 dB, a free spectral range of 12 nm, and a  $\Delta\lambda = 1.5$  nm channel wavelength spacing, consistent with the design parameters calculated by beam propagation routines. The device also showed a polarization sensitivity  $<0.5$  dB, accompanied by a 0.2 nm wavelength shift in the channel peak responsivity resulting from the small effective index mismatch between the TE and TM modes, as shown in Fig. 11(b). Also shown (inset, Fig. 11(b)) is the calculated birefringence as a function of width, with a fixed height of 2.7  $\mu\text{m}$  of the dilute waveguide. The width was chosen to optimize the trade-off between achieving a minimum birefringence, and a maximum fiber-to-chip coupling efficiency. Hence the minimum birefringence is expected at a waveguide width of 2.75  $\mu\text{m}$ , as shown in Fig. 11(b), inset. This results in a noncircular far-field pattern, thereby reducing the fiber-to-chip optical coupling efficiency. Hence, we chose a width (3  $\mu\text{m}$ ) with a slight index mismatch ( $\Delta n=2.5 \times 10^{-4}$ ) between the TE and TM modes to leave the coupling efficiency unaffected.

An essential feature of any integration technology is the portability of the design parameters from theory to experiment. That is, its success depends on the accuracy of the design models used. In Table II we provide the design values and the experimental outcome for the complex AWG structure. The experimentally observed device performance is close to the designed values in most cases, except for the interchannel

crosstalk, where a higher value was experimentally observed. This is caused by stray light not completely coupled into the AWG waveguide, but was instead incident on the detector surface due to input fiber misalignment [18]. The device performance of the ATG WDM receiver (loss, crosstalk, and polarization sensitivity) is comparable to, or better than similar devices demonstrated previously using complex regrowth and hybrid integration schemes [7, 23-25].

A final, important light transport component is the multiple quantum well waveguide modulator [11]. For example, a 250 $\mu\text{m}$  long modulator waveguide was comprised of InGaAlAs, compressively strained (+0.6%) quantum wells with tensile strained (-0.3%) barriers for operation at  $\lambda=1310$  nm. Here, InGaAlAs was used instead of InGaAsP for the quantum well material to achieve a larger range of operation temperature (0 $^{\circ}$  to 85 $^{\circ}$ C) when integrated with an ATG DFB laser (see Sec. IV.C). When using InGaAlAs quantum wells, the bandgap of the modulator quantum well absorption edge shifts by 0.4-0.5 nm/ $^{\circ}$ C, while the laser wavelength for a DFB laser shifts by only 0.1 nm/ $^{\circ}$ C. Thus, the effective wavelength detuning between laser and modulator decreases at 0.3-0.4 nm/ $^{\circ}$ C. By appropriately choosing the detuning ( $\sim 70$  nm at room 20 $^{\circ}$ C) between the laser wavelength and the absorption edge of the modulator, a high extinction ratio ( $> 6.5$  dB for a 2.5V swing) and low insertion loss ( $< 4$  dB) is maintained over the entire operating temperature range.

Figure 12 shows the experimental DC extinction curves at various temperatures. The shift to lower voltages at high temperatures is due to the reduced detuning between the laser and modulator wavelengths. The optimum modulator bias is chosen to be close to the midpoint of the extinction curve, ensuring a  $\sim 50\%$  duty cycle of the output eye.

The temperature-independent 3 dB modulation bandwidth is 10.5 GHz (inset, Fig. 12).

#### **IV. Photonic integrated circuits using combinations of ATG components**

The flexibility of ATG integration is illustrated by two archetype PICs with important systems applications: A high gain-bandwidth product SOA+p-i-n detector, and an electroabsorption modulated laser (EML). Several other integrated devices are listed in Table I for reference.

##### **IV. A. Semiconductor optical amplifier integrated with a p-i-n Photodiode**

A device that integrates all the fundamental photonic functions is a waveguide-coupled SOA/p-i-n receiver. Integrating an optical gain section with a p-i-n photodiode can significantly improve the receiver sensitivity at very high bandwidths (e.g. 40Gb/s). A monolithically integrated SOA/p-i-n receiver chip is shown in Fig. 13(a) [26].

While the fiber and active waveguides are similar to those in the emitter structure, a critical difference is that the cladding of the active guide consists of a second passive waveguide, as shown in Fig. 13(b). Using the odd mode method to design the tapers [1], most of the light from the *fundamental mode* of the fiber guide is transferred into the *first order mode* in the active waveguide, despite the presence of the higher index upper passive guide. Results of beam propagation calculations illustrating the coupling efficiencies of the different tapers are shown in Fig. 14. Incorporation of a passive waveguide into the active guide cladding results in a total cladding thickness  $>1\mu\text{m}$ , thereby minimizing absorption by the top metal contact, while a  $0.5\mu\text{m}$  thick InP spacer

placed between the active and passive waveguides enables efficient power transfer between them. After amplification in the gain section, the light is coupled to the passive guide taper. Subsequently, the light is transferred into the tapered coupling guide, and is evanescently absorbed in the uppermost  $\text{In}_{0.53}\text{Ga}_{0.47}\text{As}$  layer of the p-i-n diode.

A peak fiber-to-detector gain of  $9.5\pm 0.3$  dB is achieved at a drive current of 220mA, with a 3 dB optical bandwidth of  $\Delta\lambda = 30$  nm centered at  $\lambda=1.57\mu\text{m}$  (Fig. 15). The sensitivity vs. SOA-to-detector gain at 40Gb/s is then calculated [27] as shown in Fig. 16, inset. In this calculation, the receiver thermal noise is assumed to be  $18\text{pA}/\text{Hz}^{1/2}$ , corresponding to that from the  $50\Omega$  input impedance of the following voltage amplifier. The sensitivity improvement compared to an ATG p-i-n photodiode [16] is  $6.3\pm 0.3\text{dB}$  at a SOA-to-detector gain of 12.5dB, which is the highest gain measured for this component (assuming a propagation loss of 3dB). The sensitivity at this gain is -22dBm. A further increase of the SOA gain does not significantly improve sensitivity, since signal-spontaneous and spontaneous-spontaneous beat noise dominate, and increase in proportion to gain. Also shown in Fig. 16 is the frequency response of the device, where a 3dB bandwidth of  $(36\pm 2)$  GHz is observed, corresponding to a gain-bandwidth product of  $\sim 640\text{GHz}$ . The performance of this component represents a significant improvement over SOA/p-i-n detectors integrated using material regrowth [6]. These latter devices showed -17dBm sensitivity at 40Gb/s.

#### **IV.C Electroabsorption Modulated Laser (EML)**

ATG technology provides a simple scheme for integrating an EML, which is a key component in low cost, high bandwidth transmission systems such as 10 Gb/s Ethernets. The laser and the modulator sections form separate waveguides that are

stacked one on top of the other, and are separately optimized for operation over a wide temperature range (see Fig. 17). As discussed in Sec. III.C, the laser and the modulator both contain InGaAlAs compressively strained quantum wells (+1% for the laser, and +0.6% for the modulator sections), and tensile strained (-0.3%) barriers for operation at  $\lambda=1310\text{nm}$ . To avoid mode hops that occur in DBR lasers operated over a large temperature range such as 0-85°C operation required for uncooled 10Gb/s Ethernets, in this case the laser section is a shallow ridge, 3 $\mu\text{m}$  wide by 500 $\mu\text{m}$  long DFB structure optically coupled to the lower modulator waveguide through 180 $\mu\text{m}$  long tapers. The 250 $\mu\text{m}$  long modulator has a structure similar to the one discussed in Sec. III.C.

As in the case of vertically pumped wavelength tunable DBR gratings (Sec. III.A), the EMLs require *two* planar growth steps, the second being a full surface, or *blanket* overgrowth to define the upper cladding section above the distributed feedback (DFB) section. Here, the grating on top of the active region is defined either through electron beam lithography or holography followed by the metallorganic chemical vapor deposition blanket overgrowth of the InP/InGaAsP cladding and cap layers. Following these steps, fabrication of the device follows the standard processing sequence used for other ATG based lasers (see Fig. 3) [11]. The entire structure is passivated using SiN<sub>x</sub>. The modulator is electrically isolated from the laser using He<sup>+</sup> implantation similar to the tunable laser (see Sec. III.A). The rear facet is coated with a 90% reflective coating, and the front facet with an anti-reflection coating with a reflection coefficient  $<10^{-4}$ .

The laser is designed to provide high optical power (3 mW), while the modulator achieves a high extinction ratio ( $>6.5$  dB for a voltage swing of 2.5V) and low insertion losses ( $< 4\text{dB}$ ) over a wide range of temperatures. Figure 18a shows the light-current

characteristics for a typical device at different temperatures [11], and the lasing spectra are shown in the inset. Side mode suppression of  $> 40$  dB was observed over the temperature range from  $0^\circ$  to  $85^\circ\text{C}$ , with no power penalty incurred for transmission over 30 km of SMF-8 fiber. In Fig. 18b, we show the eye diagram for transmission using the EML at 10Gb/s bandwidth at several temperatures, showing large mask margins for this uncooled component over the full range of temperatures required for this application. Also shown in Fig. 18b is a photograph of a packaged EML in a low cost, miniature TO header, enabled by the fiber alignment-tolerant dilute passive waveguide. Hence, lasers, detectors and other ATG components using a common, simplified coupling scheme allows for the use of a similar, low-cost package for many applications – a key property of any ubiquitous integration technology.

## **V. Discussion**

From these archetype PIC demonstrations, the potential of ATG as a “platform” integration technology is evident. This technology shares several similarities with the electronic CMOS platform in that both schemes are based on a standard library of devices, computer aided design (CAD), and a common and tolerant package design for all devices. Like CMOS, ATG allows for the realization of a wide variety of PIC functionalities using universal epitaxial structures and standard processing steps by simply changing the photomask layout. For example, a universal wafer comprised of a sequence of a dilute fiber waveguide, an active light generating waveguide, and a detector layer can be commonly used for AWG-based WDM receivers [20], SOA+p-i-n receivers [26], DBR lasers [10] and chip-scale interferometer structures with integrated

SOAs for optical switching [21] or wavelength conversion [28].

Due to the progress in growth technologies, the quality and reproducibility of the epitaxial material can be maintained. Based on the desired functionality, a combination of “building blocks” from a standard library are chosen from the device family in Table I, and laid out using CAD tools. The different library building blocks have an associated set of transfer parameters such as the insertion loss, gain, spectral response, bandwidth, and bias requirements. Using these parameters, the power budget, and expected device performance of the PIC can be accurately estimated in advance. This allows for straightforward automation and optimization of the rapidly cycled design sequence, once the final performance specifications are established. This design cycle can then be taken to the next level where an automatic mask layout is defined based on the desired design parameters.

#### **IV.A. An example PIC design**

To substantiate the CAD-based design principle of the ATG scheme, we show a hypothetical PIC for a reconfigurable optical add-drop multiplexer (ROADM) in Fig. 19. Here, the first AWG demultiplexes the input signal into eight spatially separated channels. Each of these channels is then input into a 2x2 switch where the decision is made to either drop (detect) the signal, or pass it through to the second AWG which functions as a multiplexer recombining the eight channels. The channels that are to be dropped are then input to the p-i-n array. Simultaneously, channels can be added using a third demultiplexing AWG whose output waveguides serve as inputs to the 2x2 switch. Thus, when laid out in this format, the PIC performs all the ROADM functions.

To implement this circuit, the following building block components are required:

AWG demultiplexer/multiplexers, 2x2 crosspoints based on SOA interferometric structures [21], a tunable DBR laser, and a p-i-n detector array. Using these device “blocks”, the design cycle for the ROADM proceeds as follows: Firstly, each of the subcomponents are separately optimized with the standard epitaxial structure similar to the one used for the SOA/p-i-n module (see Sec. IV.A). The AWG is implemented in the lower fiber waveguide, and is coupled to the SOA at the input via tapers. The all-optical 2x2 switches employ a Mach-Zehnder configuration with SOAs as the nonlinear elements [21], or passive MMI or Y-branch switches [29,30]. Here, the interferometer consists of fiber waveguides for the arms of the interferometer and the couplers, while the SOA is integrated into the upper light emitting waveguide. The tunable DBR laser uses the fiber waveguide for the grating and phase-tuning sections, with the gain element consisting of the same active waveguide used for the SOA structure. The p-i-n receiver layer forms the upper-most waveguide, and is optically coupled to the fiber waveguide via a coupling guide and the SOA active guide. Having separately optimized the performance of each of these constituent components, the final CAD-based layout is completed.

Based on the performance of the individual components of the PIC, it is estimated that the approximately  $(1\text{cm})^2$  chip will have a total insertion loss of 8-9dB. This consists of the coupling losses (5dB per facet), AWG losses (4dB/AWG), switching loss (2dB), and waveguide losses (1dB) in combination with  $\sim 12$  dB gain provided by the SOA.

#### **IV.B. Potential shortcomings of ATG integration technology**

One drawback of ATG components is their large size resulting from the need for a  $\sim 200\mu\text{m}$  long tapers. However, all PICs are large owing to the large waveguide radii

needed to reduce bending losses, and the long active regions required to achieve sufficiently high gain lasers and SOAs. In these cases, the tapers are only a small fraction of the total device length. Furthermore, this apparent disadvantage is mitigated, to some extent, by the increased yield inherent in the relatively simple and controllable fabrication process of ATG devices, allowing for a larger number of acceptable devices to be obtained per wafer area. In particular, the elimination of complex and low yield processes associated with regrowth creates an opportunity to generate low-cost photonic components, such as the EML in Sec. IV.C. Furthermore, as the number of optical functions increases, the yield drops considerably for schemes requiring selective area growth or regrowth due to the several complex growth steps involved. On the contrary, due to the single growth needed for the ATG scheme, their complexity is greatly reduced, and the device performance in this case relies primarily on controllable and repeatable post growth processing steps.

Another concern is the absorption in the tapers leading to decreased gain in lasers and SOAs. There are two techniques that can be employed to overcome this problem. One is to pump the taper coupler along with the active ridge [8], and another is to use QWI to blue shift the absorption edge of the active material in the taper [13]. The latter scheme may also find application in devices where light is transported from a lower fiber waveguide, through an emitter active region, to a detector where losses during propagation through unpumped active region sections are significant. Electrically pumping the active region can overcome losses as the light propagates in the emitter region, although this introduces noise due to amplified spontaneous emission. However, the use of QWI allows for circumvention of this loss in PICs such as the ROADM.

A third problem arises from small parasitic reflections from the taper tips. Even extremely small reflections can cause spurious mode-coupling effects in lasers, leading to instabilities and increased relative intensity noise. Reflections are reduced by angling the taper tips. In our designs, the tapers are angled at  $7^\circ$  relative to the passive waveguide propagation axis. In addition, the tapers are designed such that the entire optical power transfer process from the active guide to the lower passive guide occurs within 75% of the taper length, thereby minimizing residual reflections from the tips.

## **VI. Summary and conclusions**

We have discussed developments on ATG-based photonic integrated devices that have recently been demonstrated by the Princeton University-ASIP, Inc. team. It is apparent that device performance is not adversely affected by the ATG integration scheme – indeed, complex PICs have been realized without sacrificing the performance of the individual (discrete) components comprising the integrated device function. Given the extraordinarily high demands on devices employed in modern optical data transmission and communication systems, this maintenance of high performance from the discrete through to the integrated chip levels is an essential feature of any successful photonic integration approach. Furthermore, the ease of manufacturability and resulting high fabrication yields of ATG-based devices has allowed for the commercialization of low cost components, such as  $\lambda=1.3\mu\text{m}$  uncooled EMLs for use in 10 Gb/s Ethernet applications[31]. Thus, for the first time, the ATG scheme enables the system designer, rather than the device physicist, to generate new photonic solutions, making the rapid design and fabrication of devices such as tunable EMLs, ROADMs, and all-optical logic

gates a straightforward matter of combining the established library of functions on a monolithic chip to serve the desired application need. This CAD design-based flexibility using standardized material structures, fabrication methods and packaging schemes has heretofore only been available to electronic system designers employing the CMOS technology base. With ATG, this flexibility has now been extended to the field of optics, and thus has the potential to lead to a rapid growth of the use of PICs enabling functions not possible until now.

### **Acknowledgements**

The authors thank Shubohashish Datta, Chunqiang Li, Yu Huang, Milind Gokhale, and Pavel Studenkov for many helpful discussions. We also thank ASIP, Inc. and DARPA for partial support of this work through the RFLICS, OptoCenter and CS-WDM programs.

## References

1. F. Xia, V. M. Menon, S. R. Forrest, "Photonic integration using asymmetric twin-waveguide (ATG) technology .I. Concepts and theory", IEEE J. Sel. Topics in Quantum Electron. vol. XX, pp-YY, 2004.
2. H. Takeuchi, K. Tsuzuki, K. Sato, M. Yamamoto, Y. Itaya, A. Sano, M. Yoneyama, and T. Otsuji, " Very high speed light source module up to 40Gb/s containing a MQW electroabsorption modulator integrated with a DFB laser," IEEE J. Sel. Topics in Quantum Electron. vol 3, pp.336-343, 1997.
3. T. L. Koch, U. Koren, R. P. Gnall, F. S. Choa, F. Hernandez-Gil, C. A. Burrus, M. G. Young, M. Oron, and B. I. Miller, " GaInAs/GaInAsP multiple quantum well integrated heterodyne receiver," Electron. Lett. vol. 25, pp.1621-1622, 1989.
4. R. L. Thornton, W. J. Mosby, and T. L. Paoli, " Monolithic waveguide coupled cavity lasers and modulators fabricated by impurity induced disordering," IEEE J. Lightwave Technol. vol. 6, pp.786-792, 1988.
5. Aoki, M.; Suzuki, M.; Sano, H.; Kawano, T.; Ido, T.; Taniwatari, T.; Uomi, K.; Takai, A, "InGaAs/InGaAsP MQW electroabsorption modulator integrated with a DFB laser fabricated by band-gap energy control selective area MOCVD," IEEE J. Quantum Electron. vol 29, pp. 2088-2096, 1993.
6. B. Mason, J. M. Geary, J. M. Freund, A. Ougazzaden, C. Lentz, K. Glogovsky, G. Przybylek, L. Peticolas, F. Walters, L. Reynolds, J. Boardman, T. Kercher, M. Rader, D. Monroe, L. Ketelsen, S. Chandrasekhar, and L. L. Buhl, "40 Gb/s photonic integrated receiver with -17 dBm sensitivity," in Tech. Dig. Opt. Fiber Commun. Conf., Anaheim, CA, 2002, Postdeadline Paper FB10.

7. T. Ohyama, Y. Akahori, T. Yamada, M. Ishii, S. Kamei, and Y. Sakai, "8-channel x 2.5 Gbit/s hybrid integrated multiwavelength photoreceiver module with arrayed-waveguide grating demultiplexer," *Electron Lett.*, vol. 38, no. 9, pp. 419–421, 2002.
8. P.V. Studenkov, "Photonic integration using asymmetric twin-waveguides," PhD Thesis, Princeton University, 2001.
9. P. V. Studenkov, M. R. Gokhale and S. R. Forrest, "Efficient coupling in integrated twin-waveguide lasers using waveguide tapers", *IEEE Photon. Technol. Lett.* vol. 11, pp. 1096-1098, 1999
10. P. V. Studenkov, F. Xia, M. R. Gokhale and S. R. Forrest, "Asymmetric twin-waveguide 1.55- $\mu\text{m}$  wavelength laser with a distributed Bragg reflector", *IEEE Photon. Technol. Lett.* vol. 12, no. 5, pp. 468-470, 2000.
11. M. R. Gokhale, P. V. Studenkov, J. U. McHale, J. Thomson, J. Yao, and J. V. Saders, "Uncooled, 10Gb/s 1310nm electroabsorption modulated laser", in *Optical Fiber Communication Conf. Proc.*, Atlanta, GA, 2003, Paper PD42.
12. H. Wang, C. Li, and S. R. Forrest, "A Fully Integratable 1.55- $\mu\text{m}$  Wavelength Continuously Tunable Asymmetric Twin-Waveguide Distributed Bragg Reflector Laser", *IEEE Photon. Technol. Lett.* vol. 15, no. 9, pp. 1189-1191, 2003.
13. Y. Huang, F. Xia, V. M. Menon, and S. R. Forrest, "Reduction of absorption loss in asymmetric twin waveguide laser tapers using argon plasma-enhanced quantum well intermixing," accepted, *IEEE Photon. Technol. Lett.*, 2005.
14. G. P. Agarwal, *Fiber-Optic Communication Systems*, 2nd ed. New York: Wiley, 1997.

15. V. Jayaraman, D. A. Cohen, and L. A. Coldren, "Demonstration of broadband tunability in a semiconductor laser using sampled gratings," *Appl. Phys. Lett.* vol. 60, pp. 2321-2323, 1992.
16. F. Xia, J. K. Thomson, M. R. Gokhale, P. V. Studenkov, J. Wei, W. Lin and S. R. Forrest, "An asymmetric twin-waveguide high-bandwidth photodiode using a lateral taper coupler," *IEEE Photon. Technol. Lett.*, vol. 13, pp. 845-847, 2001.
17. J. Wei, F. Xia, S. R. Forrest, "A high-responsivity high bandwidth asymmetric twin-waveguide coupled InGaAs-InP-InAlAs avalanche photodiode," *IEEE Photon. Technol. Lett.*, vol. 14, pp. 1590-1592, 2002.
18. M. Achouche, V. Magnin, J. Harari, F. Lelarge, E. Derouin, C. Jany, D. Carpentier, F. Blache, and D. Decoster, "High performance evanescent edge coupled waveguide unitraveling-carrier photodiodes for >40-Gb/s optical receivers," *IEEE Photon. Technol. Lett.* vol. 16, pp. 584-586, 2004.
19. S. Agashe, S. Datta, F. Xia, and S. R. Forrest, "A monolithically integrated long-wavelength balanced photodiode using asymmetric twin-waveguide technology," *IEEE Photon. Technol. Lett.* vol. 16, pp. 236-238, 2004.
20. W. Tong, V. M. Menon, F. Xia, S. R. Forrest, "An asymmetric twin waveguide, 8-channel polarization independent arrayed waveguide grating with an integrated photodiode array," *IEEE Photon. Technol. Lett.* vol. 16, pp. 1170-1172, 2004.
21. P. V. Studenkov, M. R. Gokhale, J. Wei, W. Lin, I. Glesk, P. R. Prucnal, and S. R. Forrest, "Monolithic integration of an all-optical Mach-Zehnder demultiplexer using asymmetric twin-waveguide structure," *IEEE Photon. Technol. Lett.* vol. 13, pp. 600-602, 2001.

22. V. M. Menon, W. Tong, and S. R. Forrest, "Control of quality factor and critical coupling in microring resonators through integration of a semiconductor optical amplifier," *IEEE Photon. Technol. Lett.* vol. 16, pp. 1343-1345, 2004.
23. S. Chadrasekhar, M. Zirni, A. G. Dentai, C. H. Joyner, F. Storz, C. Z. Burrus, and L. M. Lunardi, "Monolithic eight-wavelength demultiplexed receiver for dense WDM applications," *IEEE Photon. Technol. Lett.*, vol. 7, pp. 1342–1344, 1995.
24. M. R. Amersfoort, C. R. de Boer, B. H. Verbeek, P. Demeester, A. Looyen, and J. J. G. M. van der Tol, "Low-loss phased-array based 4-channel wavelength demultiplexer integrated with photodetectors," *IEEE Photon. Technol. Lett.*, vol. 6, pp. 62–64, 1994.
25. M. Kohtoku, H. Sanjoh, S. Oku, Y. Kadota, and Y. Yoshikuni, "Packaged polarization-insensitive WDM monitor with low loss (7.3 dB) and wide tuning range (4.5 nm)," *IEEE Photon. Technol. Lett.*, vol. 10, pp. 1614–1616, 1998.
26. F. Xia, J. Wei, V. Menon, and S. R. Forrest, "Monolithic integration of a semiconductor optical amplifier and a high bandwidth p-i-n photodiode using asymmetric twin-waveguide technology", *IEEE Photon. Technol. Lett.* vol. 15, pp-452-454, 2003.
27. N. A. Olsson, "Lightwave systems with optical amplifiers," *J. Lightwave Technol.*, vol. 7, pp. 1071-1082, 1989.
28. V. M. Menon, W. Tong, C. Li, F. Xia, I. Glesk, P. R. Prucnal, and S. R. Forrest, "All-optical wavelength conversion using a regrowth free monolithically integrated Sagnac interferometer," *IEEE Photon. Technol. Lett.* vol. 15, pp. 254-256, 2003.

29. S. S. Agashe, K. -T. Shiu and S. R. Forrest, "Compact high-contrast ratio low-loss polarization-insensitive wide wavelength range 2x2 optical switch", *IEEE Photon. Technol. Lett.*, submitted, 2004.
30. S. Abdalla, S. Ng, P. Barrios, D. Celo, A. Delage, S. El-Mougy, I. Golub, J. -J. He, S. Janz, R. McKinnon, P. Poole, S. Raymond, T. J. Smy and B. Syrett, "Carrier injection-based digital optical switch with reconfigurable output waveguide arms", *IEEE Photonics Technology Letters*, vol. 16, pp. 1038-1040, 2004.
31. ASIP, Inc., 25 Worlds Fair Drive, Somerset, NJ, 08873 [www.asipinc.com](http://www.asipinc.com)

## Figure Captions:

- [1] (a) Scanning electron micrograph of an adiabatic taper coupler with a lower passive waveguide, and (b) simulation of light propagation from a passive, to an active, and back to a passive waveguide with a total loss  $<0.5$  dB. Here,  $Z$  corresponds to the propagation direction, and  $Y$  to the height of the waveguide. The monitor values correspond to the optical power in a mode in a given region. The optical power in the passive waveguide mode drops while that in the active waveguide increases as the light propagates through the first taper coupler ( $Z = 0 - 175 \mu\text{m}$ ) and opposite in the case of the second taper ( $Z = 600 - 675 \mu\text{m}$ ).
- [2] (a) Cross section of a dilute fiber waveguide showing the high refractive index InGaAsP ( $\lambda_g = 1.05 \mu\text{m}$ ) layers (dark) interspersed between InP layers (light) and (b) simulated far-field pattern of the dilute fiber waveguide showing a nearly circular mode profile to be matched to a lensed optical fiber.
- [3] (a) Refractive index profile of an ATG SOA/laser epitaxial structure, and (b) scanning electron micrograph of the epitaxial structure grown by gas source molecular beam epitaxy showing the passive and active waveguides [8].
- [4] Schematic of the post-growth processing steps for fabricating ATG (a) lasers/SOAs and (b) photodetectors. A full description of the process is given in the text.

- [5] Light output power vs current characteristics of two ATG Fabry-Perot lasers before and after removal (by cleaving) of taper couplers. Solid circles: laser A with two tapers (first taper length/cavity length/second taper length  $L = 0.77/2.05/0.56$  mm); dashed line- the same laser with one taper cleaved off ( $L = 0/2.0/0.56$ mm). Open circles: Laser B with one taper and one cleaved mirror ( $L=0/1.95/0.59$  mm). Solid line: Same laser with taper cleaved off ( $L=0/1.90/0$  mm). Inset: Infrared images of the near field patterns for lasers with and without taper coupler.
- [6] Schematic of the wavelength tunable ATG-DBR laser. The rear grating and phase section are used for tuning the wavelength of the laser without mode hops by plasma-loading. Upper-left inset: Refractive index profile and doping scheme of the tunable ATG DBR laser. The active waveguide and the central section of the passive waveguide are undoped. Lower-right inset: Scanning electron micrograph of the tunable grating. The section shown is approximately  $1.5\mu\text{m}$  long.
- [7] (a) Contour plot of the wavelength change as a function of the current in the grating tuning and phase tuning sections. Mode hops occur when tuning/phase currents cross the mode hopping contours (bold lines). The gaps at the ends of these mode-hopping contours indicate the possibility of accessing all wavelengths without mode hops through an appropriate combination of grating tuning and phase currents. (b) Emission spectra of the tunable ATG-DBR laser at various grating tuning currents.

- [8] Schematic of current injection schemes for tuning the grating resonant wavelength in an ATG laser. (a) Lateral pumping scheme used in the laser in Fig. 7 indicating very small overlap of the current path with the optical mode, and (b) vertical pumping scheme using a single blanket overgrowth for the upper cladding layer. Calculations indicate that in this latter case, the total current required to attain the same amount of refractive index change is reduced by one third in comparison to the lateral pumping scheme.
- [9] Measured frequency response of the ATG p-i-n detector at  $-3$  V bias using a 50 GHz optical network analyzer indicating a 3dB bandwidth of 36GHz. Inset: Schematic of an ATG based waveguide photodiode.
- [10] (a) Scanning electron micrograph of the multimode interference coupler with integrated balanced waveguide photodiodes. (b) Measured photocurrents of the two p-i-n detectors as functions of the input optical power incident on one waveguide at the right of the MMI coupler in (a), indicating balance of  $<0.5$  dB.
- [11] (a) Spectral response of the eight channel arrayed waveguide grating measured using the integrated p-i-n detector array. A tunable laser with  $-2$ dBm output power was used as the input. (b) Measured polarization dependent response for TE and TM input light showing 0.5dB polarization sensitivity in peak channel photocurrent, and 0.2 nm shift in peak wavelength. Inset: Calculated difference in effective refractive indices for TE and TM fundamental optical modes in the

dilute waveguide as a function of the waveguide width. The dashed line indicates the waveguide width of the fabricated device and the expected birefringence.

- [12] Normalized DC extinction curves for the waveguide modulator at different temperatures. As temperature increases, the extinction curves shift to lower voltages due to reduced detuning between the modulator and laser wavelengths. Inset: Small signal bandwidth of the modulator with integrated laser on a submount at different temperatures, showing a bandwidth of 10GHz.
  
- [13] (a) Schematic of an ATG SOA/p-i-n module. (b) Refractive index profile of the SOA/p-i-n epitaxial structure. Here, the fiber and active guides are similar to those in ATG-based SOA devices, and the coupling guide and p-i-n photodiode are similar to that used for ATG-based photodiodes.
  
- [14] Simulation of light propagation through the SOA/p-i-n module. Here, Y corresponds to the height of the waveguide, taper 1 corresponds to the coupler from the fiber waveguide to the active SOA waveguide, and taper 2 corresponds to the coupler between the SOA waveguide and the coupling guide. The power transfer efficiency at various stages in the module is shown in the bottom plot, indicating a total loss  $< 1$ dB.

- [15] Fiber-to-detector TE-mode gain versus SOA injection current at a peak gain wavelength of  $\lambda=1.57\mu\text{m}$ . Inset: Fiber-to-detector TE-mode gain versus wavelength of the incident light, indicating a gain bandwidth of 30nm.
- [16] Frequency response of the p-i-n detector in the SOA/p-i-n module at  $-3\text{ V}$  bias showing a bandwidth of 35GHz. Inset: Calculated receiver sensitivity (at a bit error rate of  $10^{-9}$ ) at 40 Gb/s versus SOA-to-detector gain. Here,  $\eta_{in}$  is the amplifier input coupling efficiency,  $\eta_{det}$  is the ATG p-i-n detector quantum efficiency, and  $r$  is the ratio of the power in bit “0” to that in bit “1.” The horizontal line corresponds to the sensitivity of an ATG p-i-n detector coupled directly to a  $50\text{-}\Omega$  impedance receiver.
- [17] Schematic of the ATG-based distributed feedback (DFB) laser with integrated electroabsorption modulator. The laser and the modulator waveguides consist of InGaAlAs quantum wells in a *p-i-n-i-p* epitaxial structure that allows for independent bias of the laser and modulator sections. The DFB structure is formed using two growth steps, the first to grow the base layers, and the second blanket overgrowth covers the pre-etched grating with the InP/InGaAsP cladding and cap layers. From Ref. [11].
- [18] (a) The peak fiber-coupled output power versus laser current of the integrated laser+modulator. Inset: Output spectra of the electroabsorption modulated laser (EML) at different temperatures. (b) Left: Optical eye diagrams for ASIP’s

uncooled,  $\lambda=1310\text{nm}$  EML at 10 Gbps over temperature. From Ref. [11].. Right: Low-cost TO-can based TOSA package containing the uncooled EML. Courtesy, ASIP, Inc.

- [19] Schematic of a hypothetical photonic integrated circuit for a reconfigurable optical add-drop multiplexer (ROADM) that can be developed using the ATG-library of photonic devices. The various building blocks that have been discussed in previous sections are shown as blocks in the diagram. The multiple wavelength input signal is fed into the AWG I where it is demultiplexed and input into the 2x2 switches. The signal is multiplexed at AWG II for output into the output fiber. Wavelengths to be added are injected from a tunable laser to AWG III, which spatially separates the different wavelengths to be fed to the 2x2 switches.

**Table I:** Asymmetric Twin Waveguide Library of Photonic Devices<sup>(a)</sup>

	Device	Function	Performance Characteristics	Ref.
1	Fabry Perot laser	Emitter	$I_{th} = 70\text{mA}$ , 35mW output power, slope efficiency = 0.08 W/A	[9]
2	Distributed Bragg Reflecting laser	Emitter	$I_{th} = 35\text{mA}$ , 11mW, slope efficiency = 0.09 W/A, SMSR > 40dB	[10]
3	Distributed Bragg Reflecting-Tunable laser	Emitter	$I_{th} = 50\text{mA}$ , 13 mW output power, slope efficiency = 0.12 W/A, SMSR > 36 dB, tuning range = 4.8 nm	[12]
4	p-i-n photodiode	Detector	$R = 0.75 \text{ A/W}$ , 3dB electrical bandwidth $\geq 40\text{GHz}$ , alignment tolerance $>\pm 1.1 \mu\text{m}$	[16]
5	Avalanche Photodiode	Detector	$R \sim 10 \text{ A/W}$ , ext. quantum efficiency = 48%, 3dB bandwidth = 31.5GHz, gain-bandwidth product=150 GHz	[17]
6	Balanced Photodiode	Detector	$R = 0.32 \text{ A/W}$ , 3dB electrical bandwidth = 15GHz, Imbalance < 0.5dB, CMRR = 34 dB	[19]
7	MMI Coupler	Guiding	Imbalance < 0.5dB, 3db spectral bandwidth $\sim 25\text{nm}$	[19]
8	Arrayed Waveguide Grating + p-i-n detector array	Guiding	Channel spacing = 1.5nm, 8 Channels, crosstalk = -14dB, channel non-uniformity=1.5dB, FSR = 12 nm, Pol. sensitivity < 0.5dB, 3dB electrical	[20]
9	Waveguide Modulator	Guiding	Extinction ratio >6.5 dB at 2.5 V, insertion loss <4 dB at 20 – 80 <sup>0</sup> C, bandwidth=10.5GHz.	[11]
10	Microring resonator + SOA	Guiding	Extinction ratio = 10dB, $Q = 2.2 \times 10^4$ , FSR = 0.25 nm, control of critical coupling and loss compensation	[22]
11	Semiconductor optical amplifier + p-i-n photodiode	PIC	Gain = 9.5 dB at 220 mA SOA current, 3dB electrical bandwidth: 36 GHz, gain-bandwidth product: 640 GHz	[26]
12	All optical demultiplexer	PIC	Switching window = 28 ps, extinction ratio = 13 dB	[21]
13	Wavelength Converter	PIC	10 Gb/s, extinction ratio $\sim 6\text{dB}$ , conversion over 30nm	[28]
14	Electroabsorption Modulated Laser	PIC	10Gb/s, $I_{th} = 35\text{mA}$ , 2-4mW, uncooled op. from 10 <sup>0</sup> C-85 <sup>0</sup> C, extinction ratio > 6.5 dB, $\lambda = 1.31 \mu\text{m}$	[11]

<sup>(a)</sup> Operating wavelength of all devices is  $\lambda=1.55\mu\text{m}$  unless otherwise noted.

**Table II:** Comparison between design parameters and experimental outcome of arrayed waveguides with integrated p-i-n photodiodes.

<b>Parameter</b>	<b>Design value</b>	<b>Experimental outcome</b>
Channel Spacing	1.6 nm	1.5nm
AWG loss	3.0 dB	4.0 dB
Crosstalk	-22 dB	-16 dB
Channel non-uniformity	< 1dB	<1.5dB
Polarization sensitivity	< 0.5 dB, $\Delta\lambda < 0.2$ nm	< 0.5dB, $\Delta\lambda = 0.2$ nm

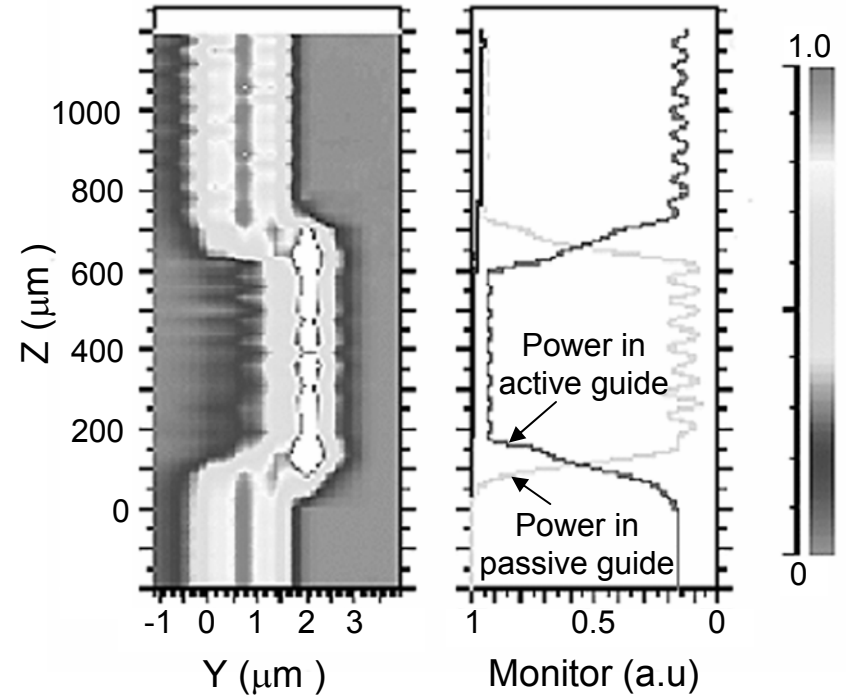
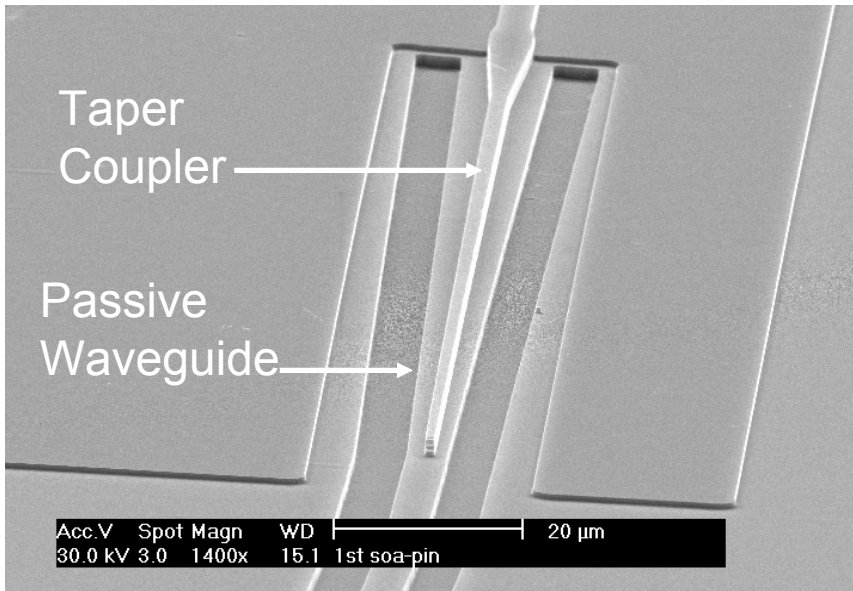


**Fig. 1**

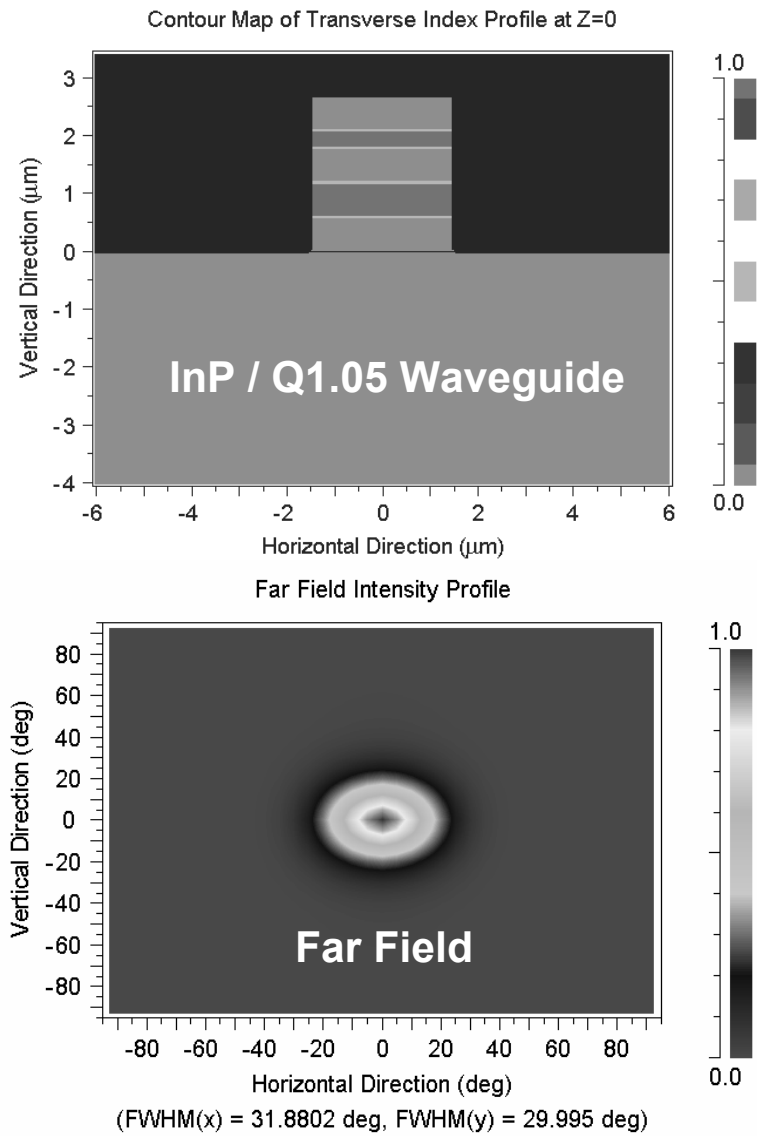


**Fig. 2**

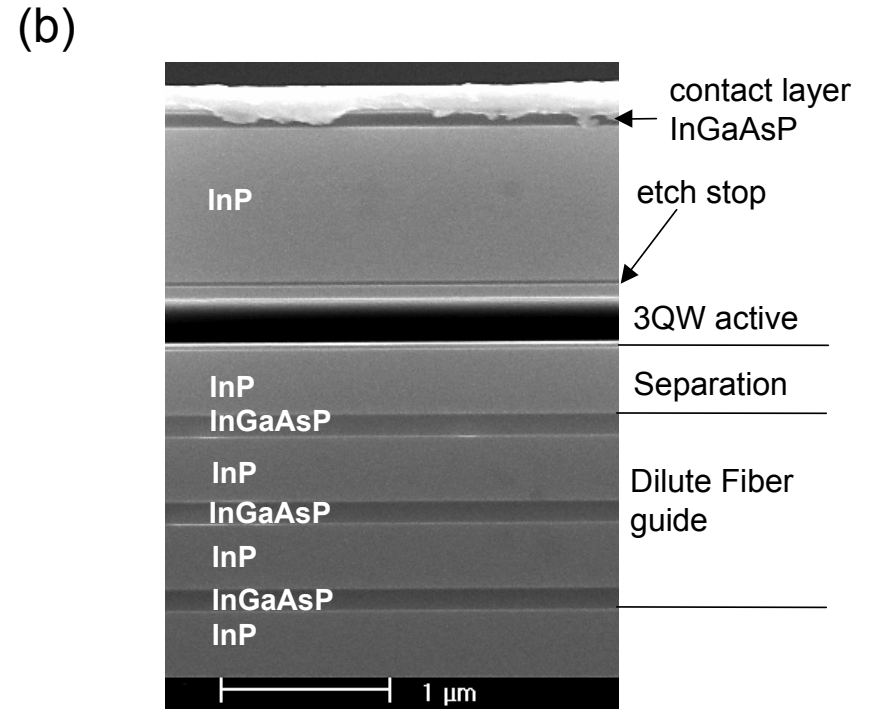
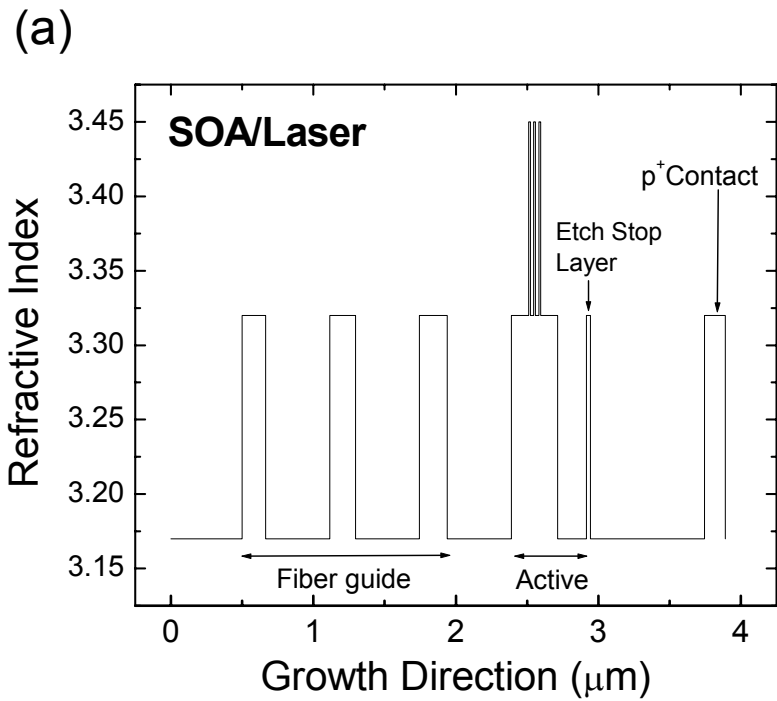


**Fig. 3**

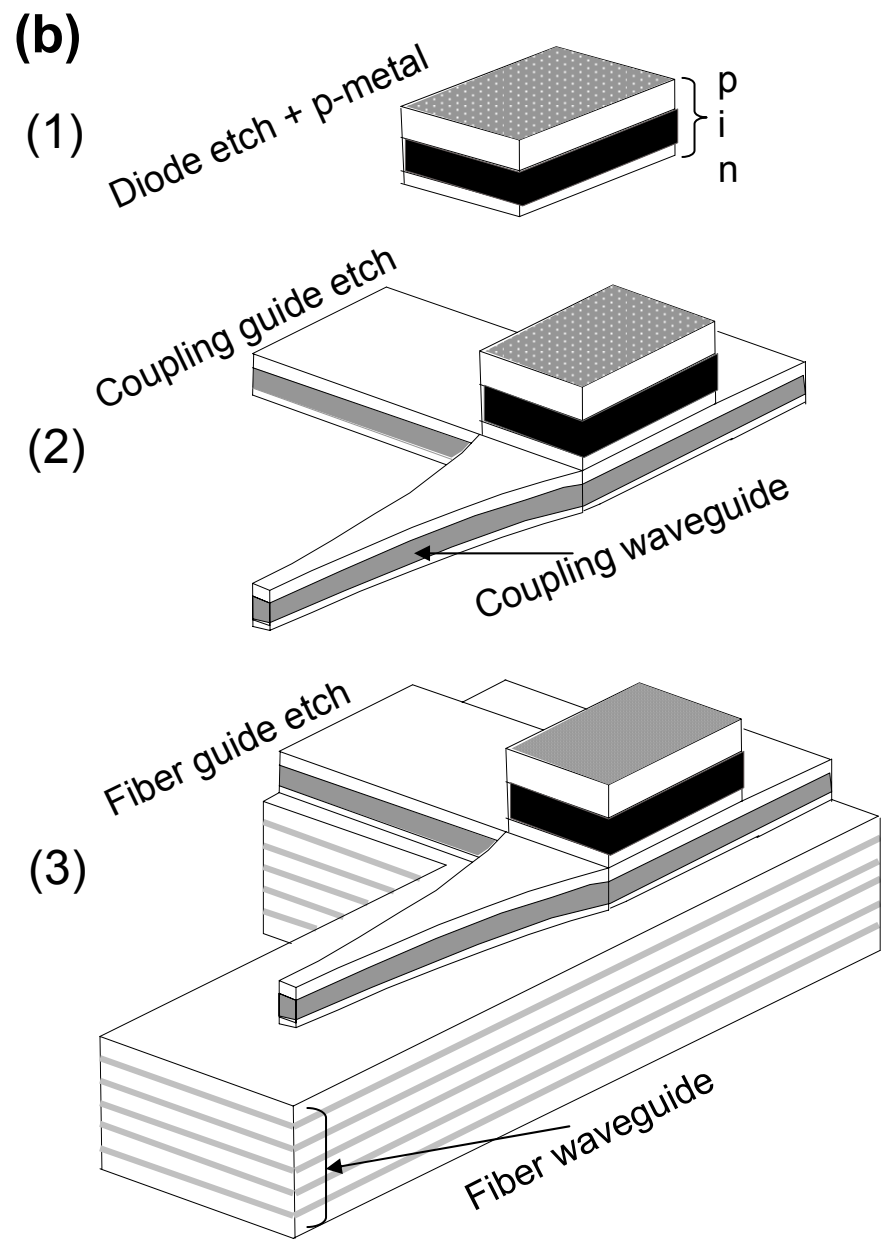
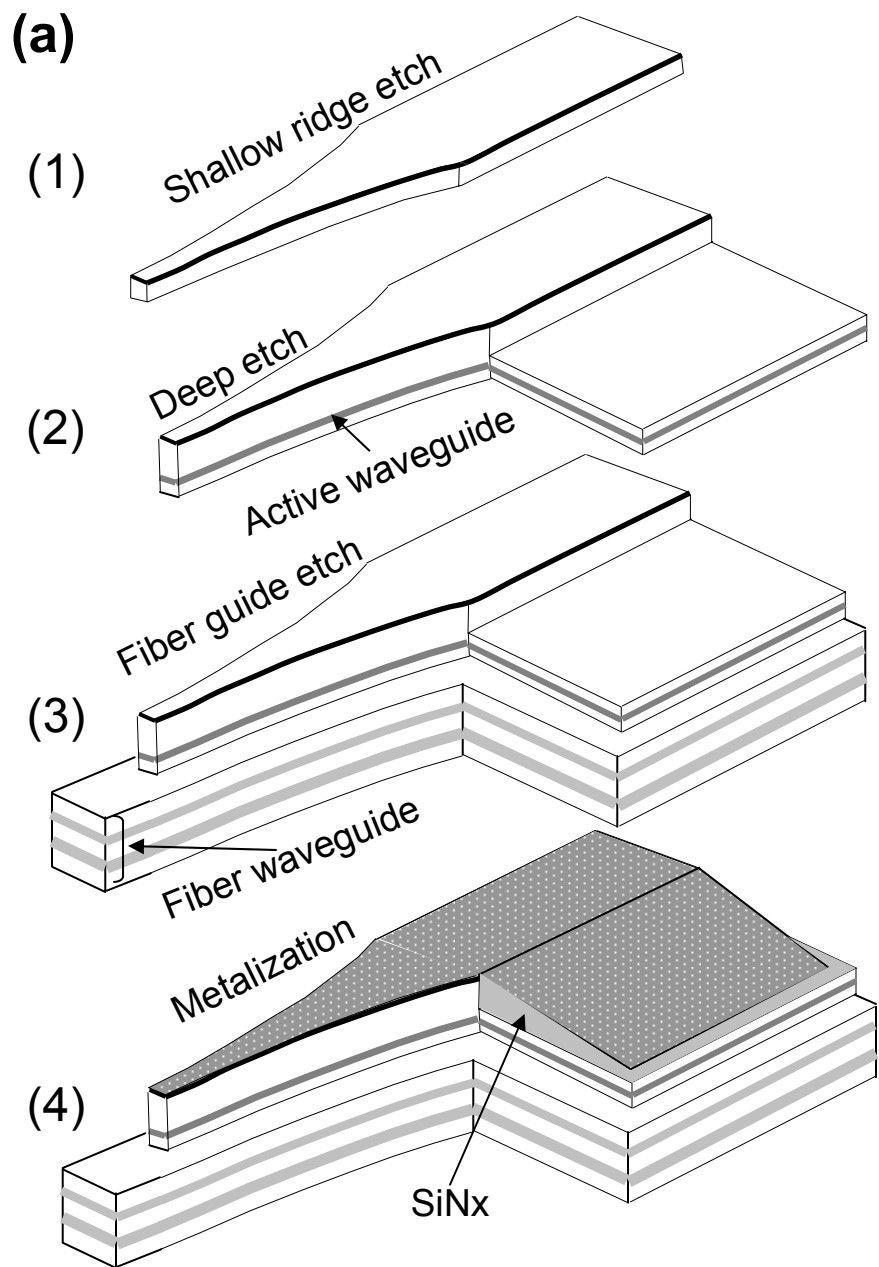


**Fig. 4**

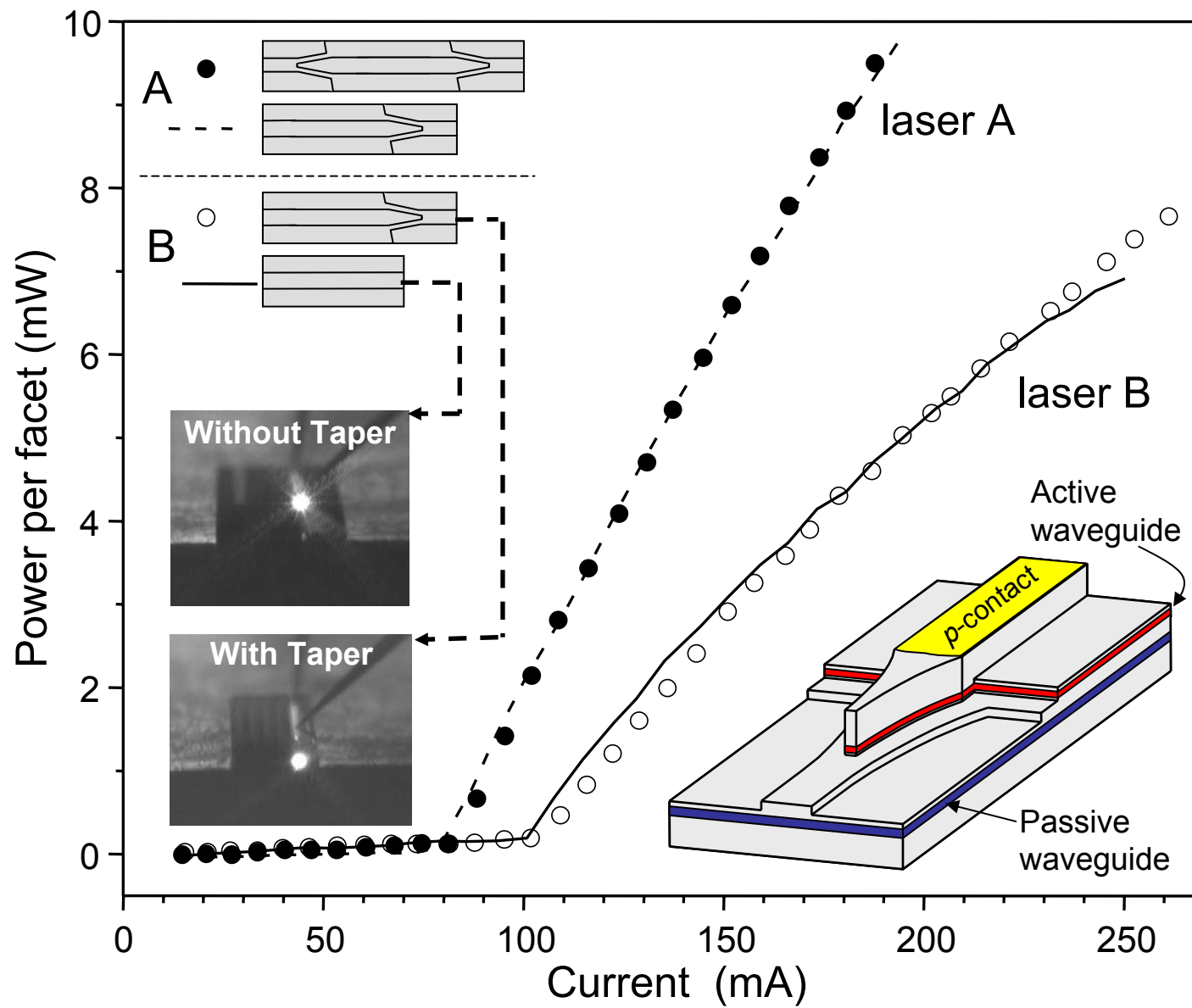
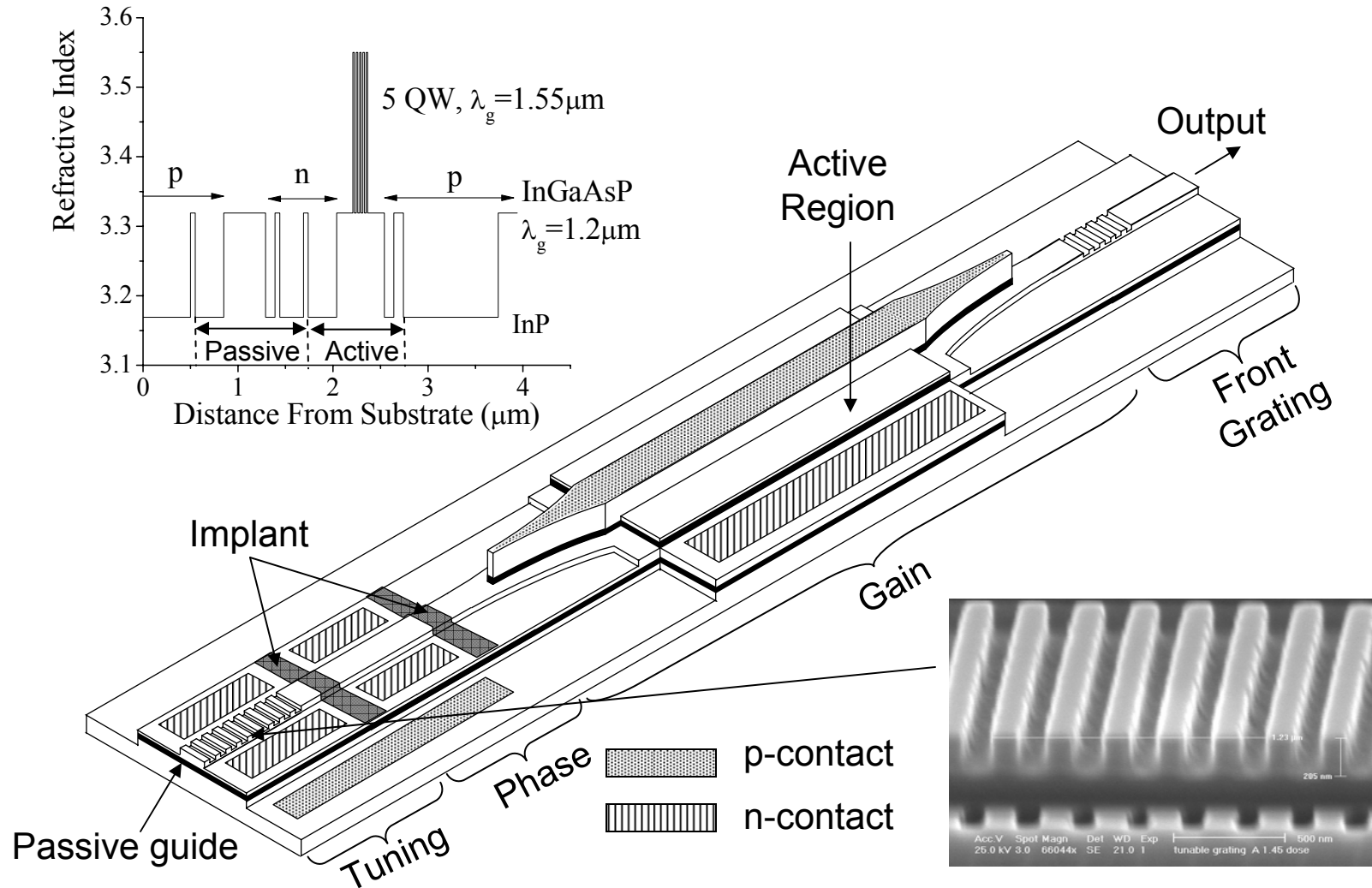
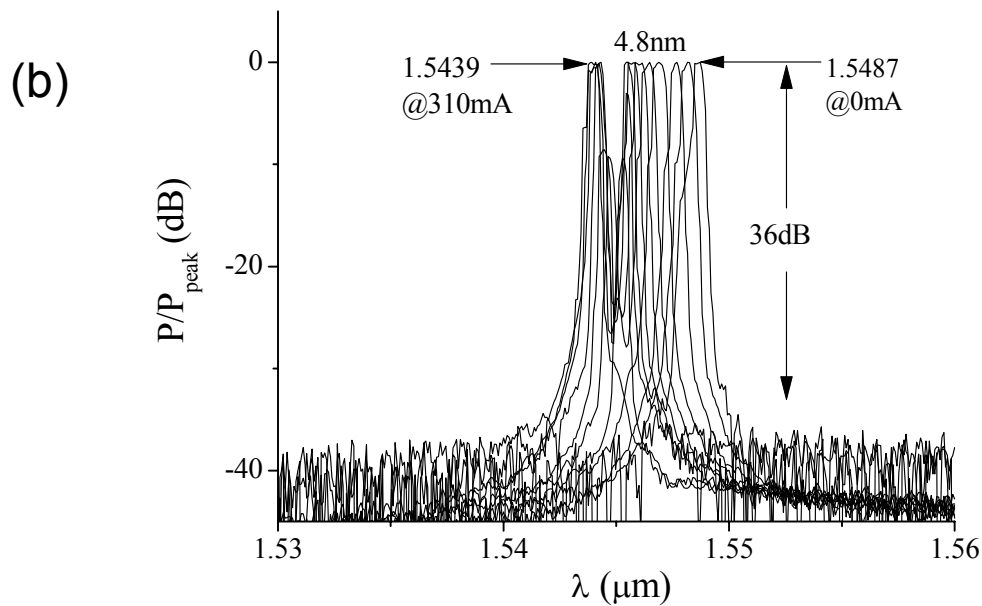
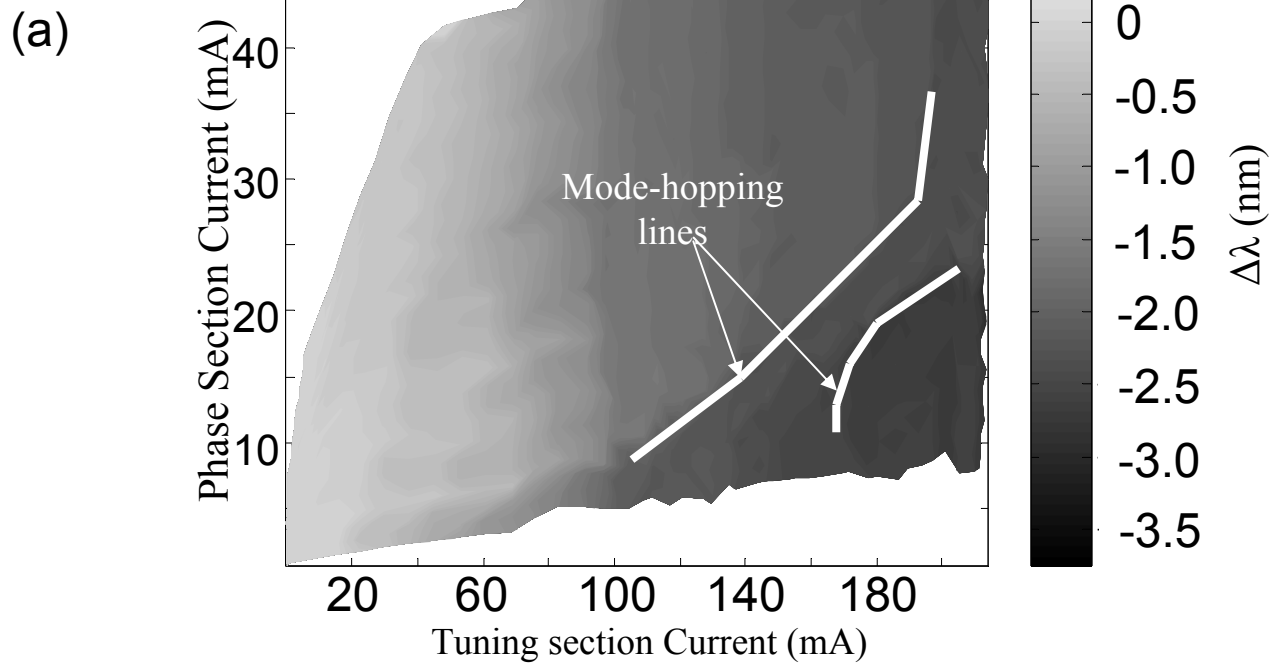


Fig. 5



**Fig. 6**



**Fig. 7**

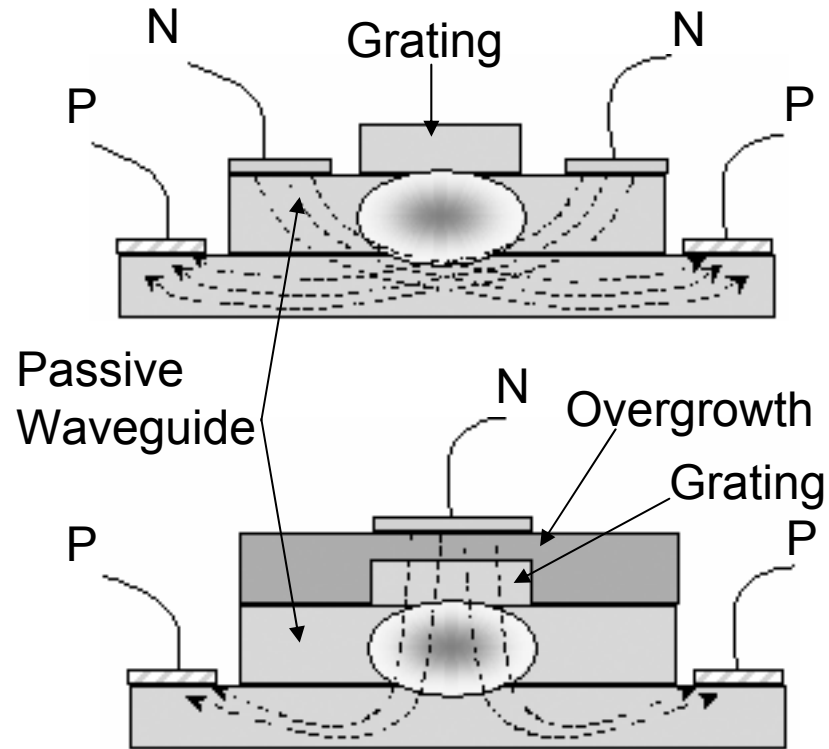


Fig. 8

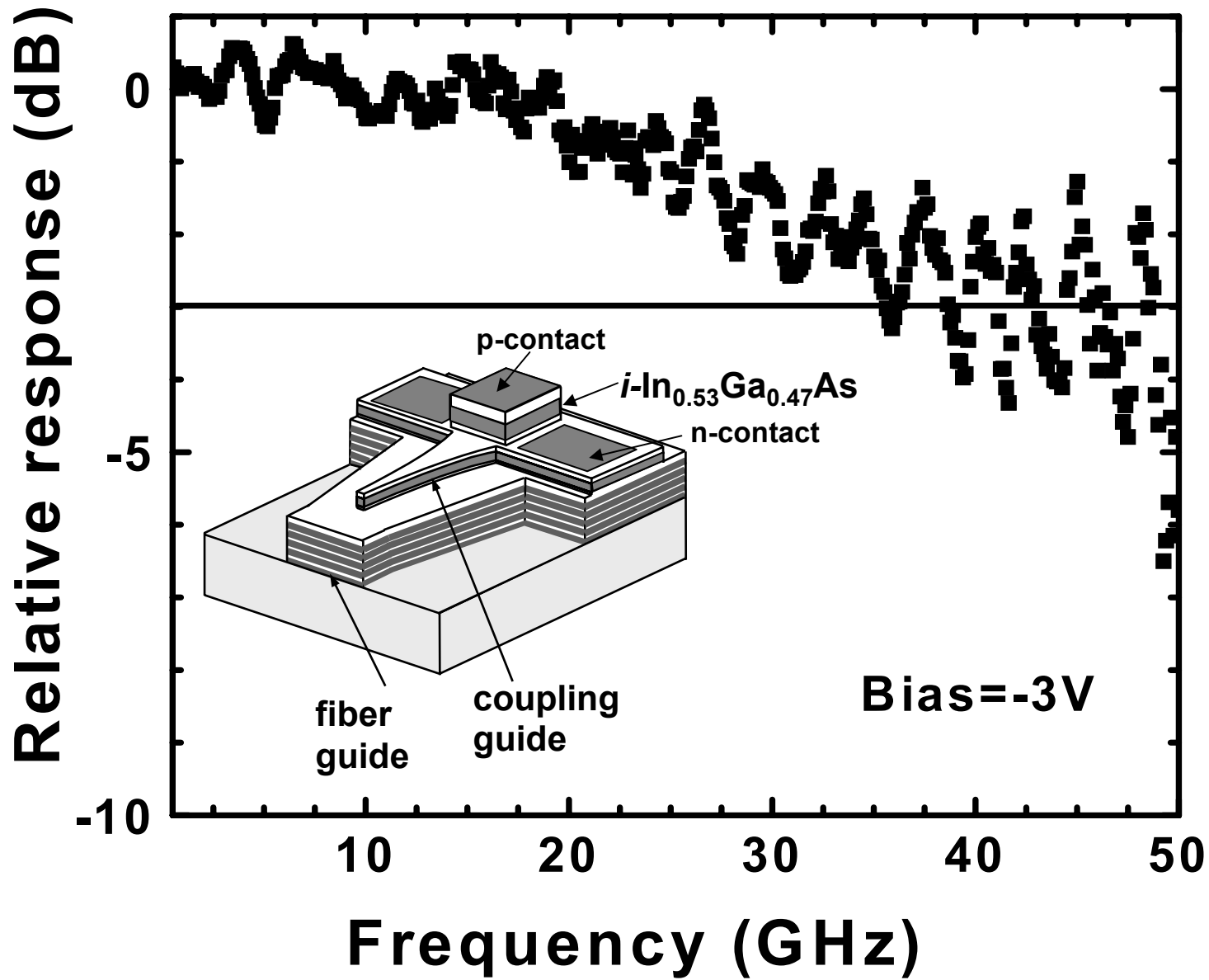


Fig. 9

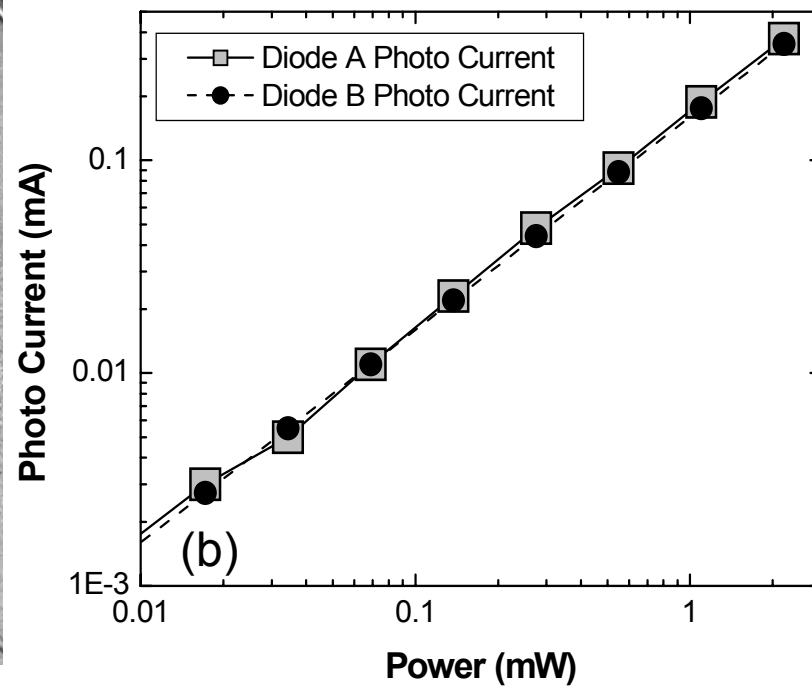
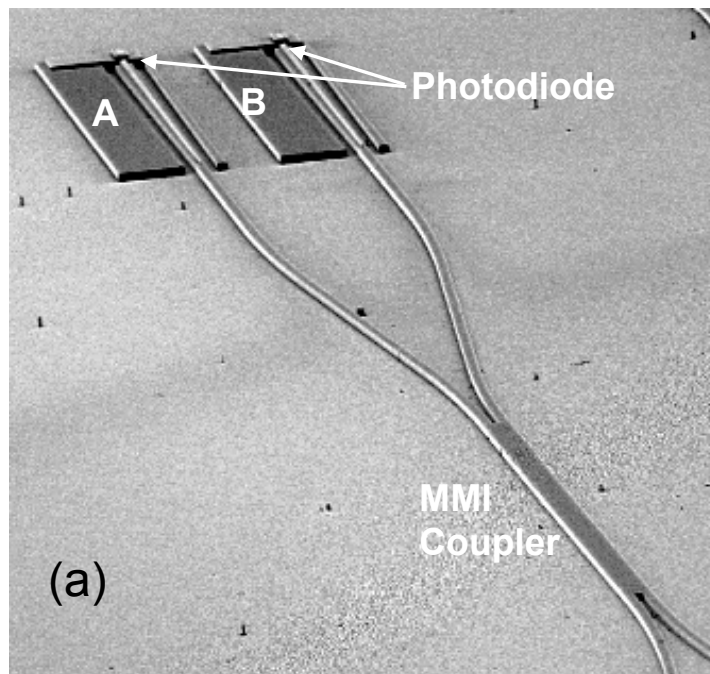
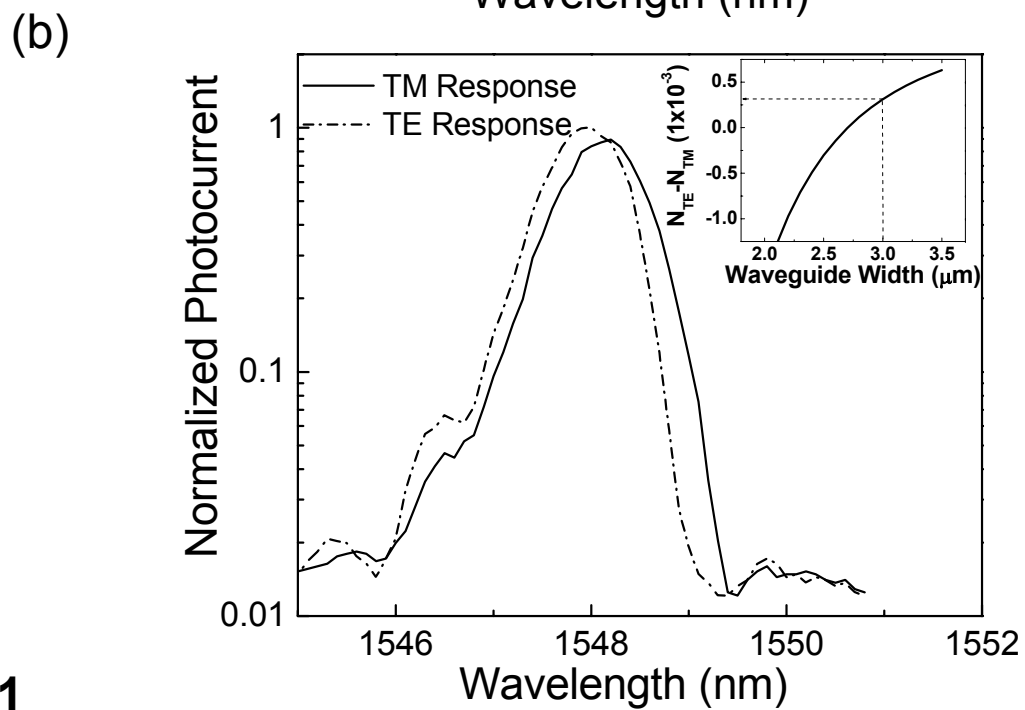
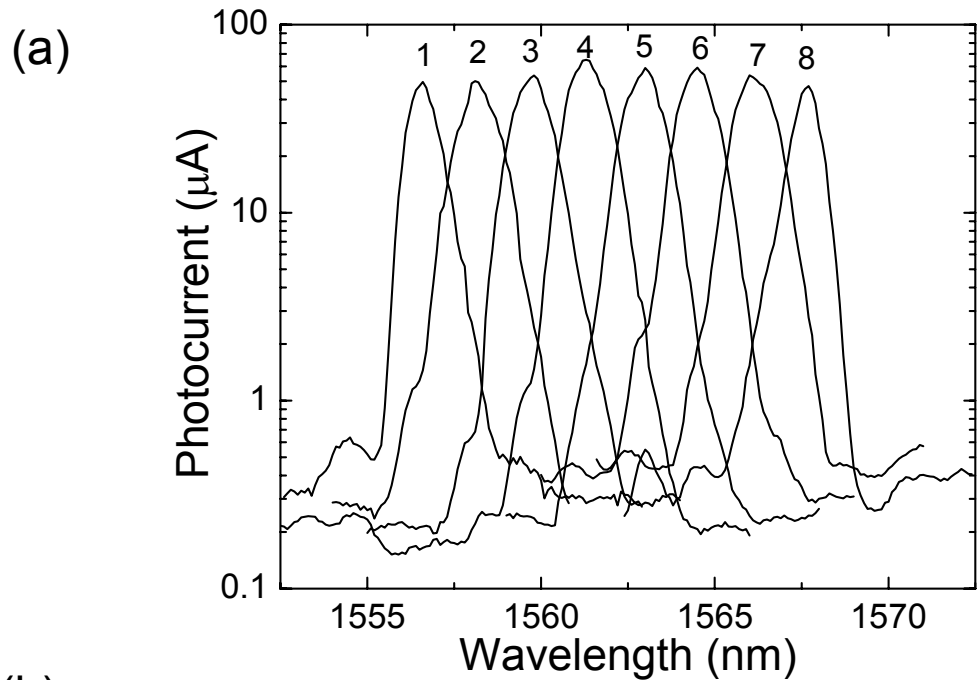


Fig. 10



**Fig. 11**

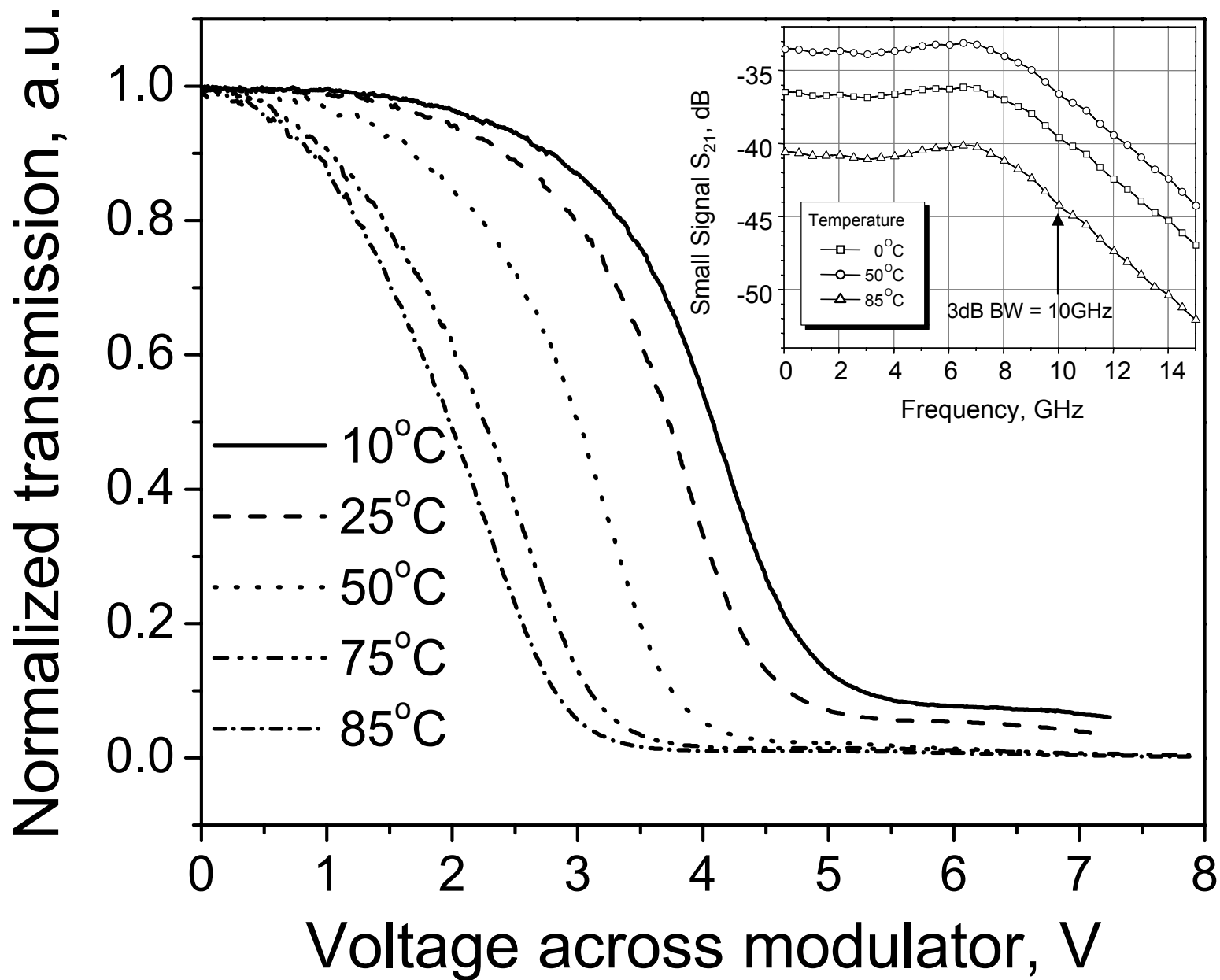


Fig. 12

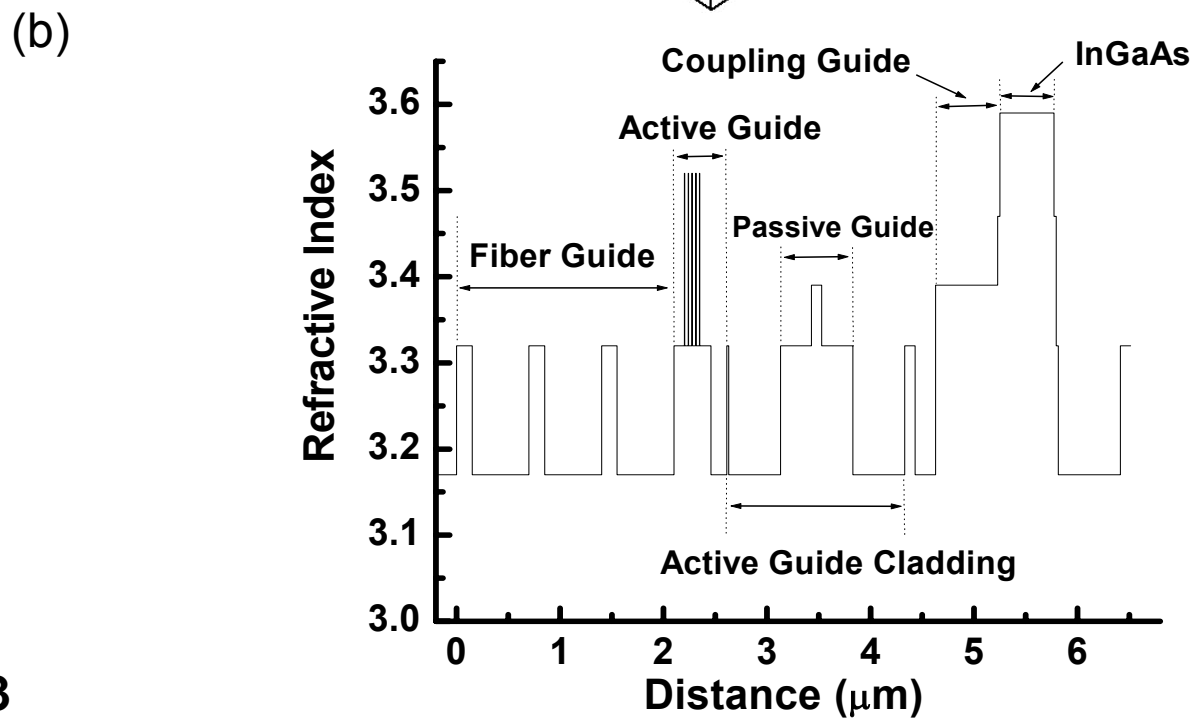
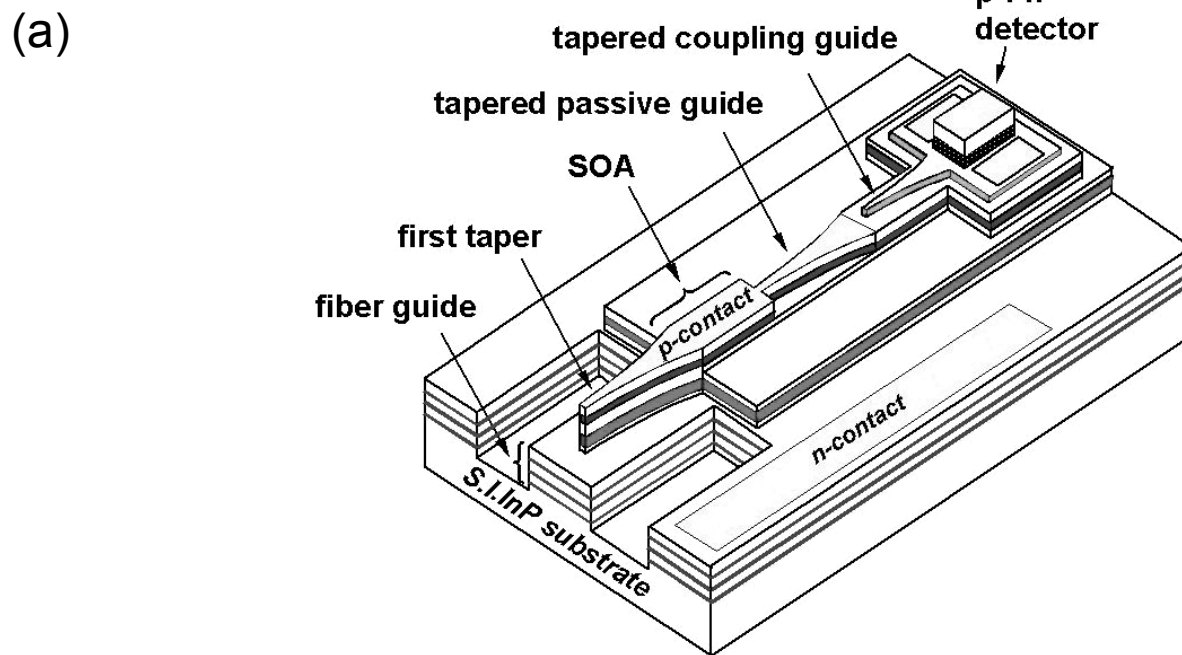


Fig. 13

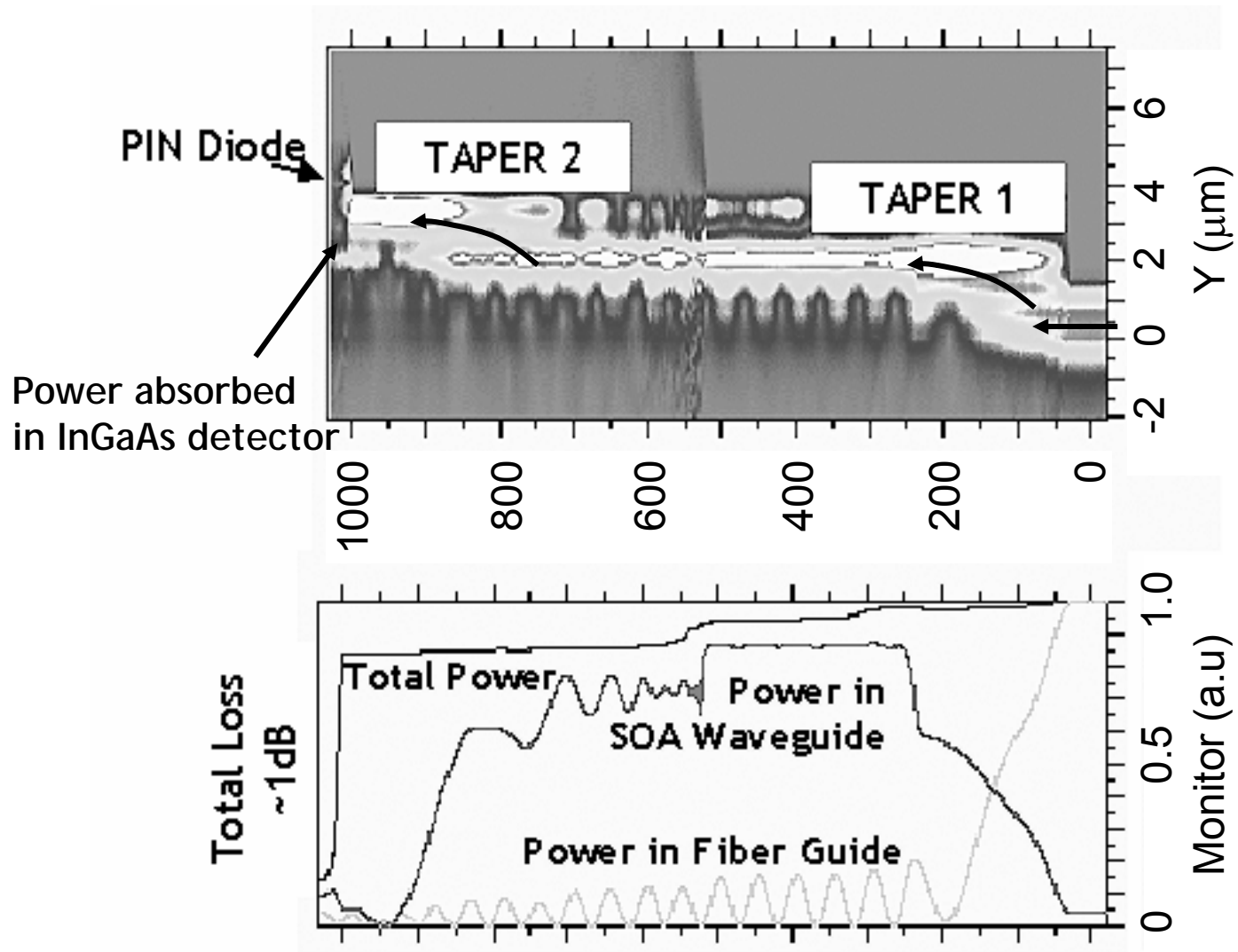


Fig. 14

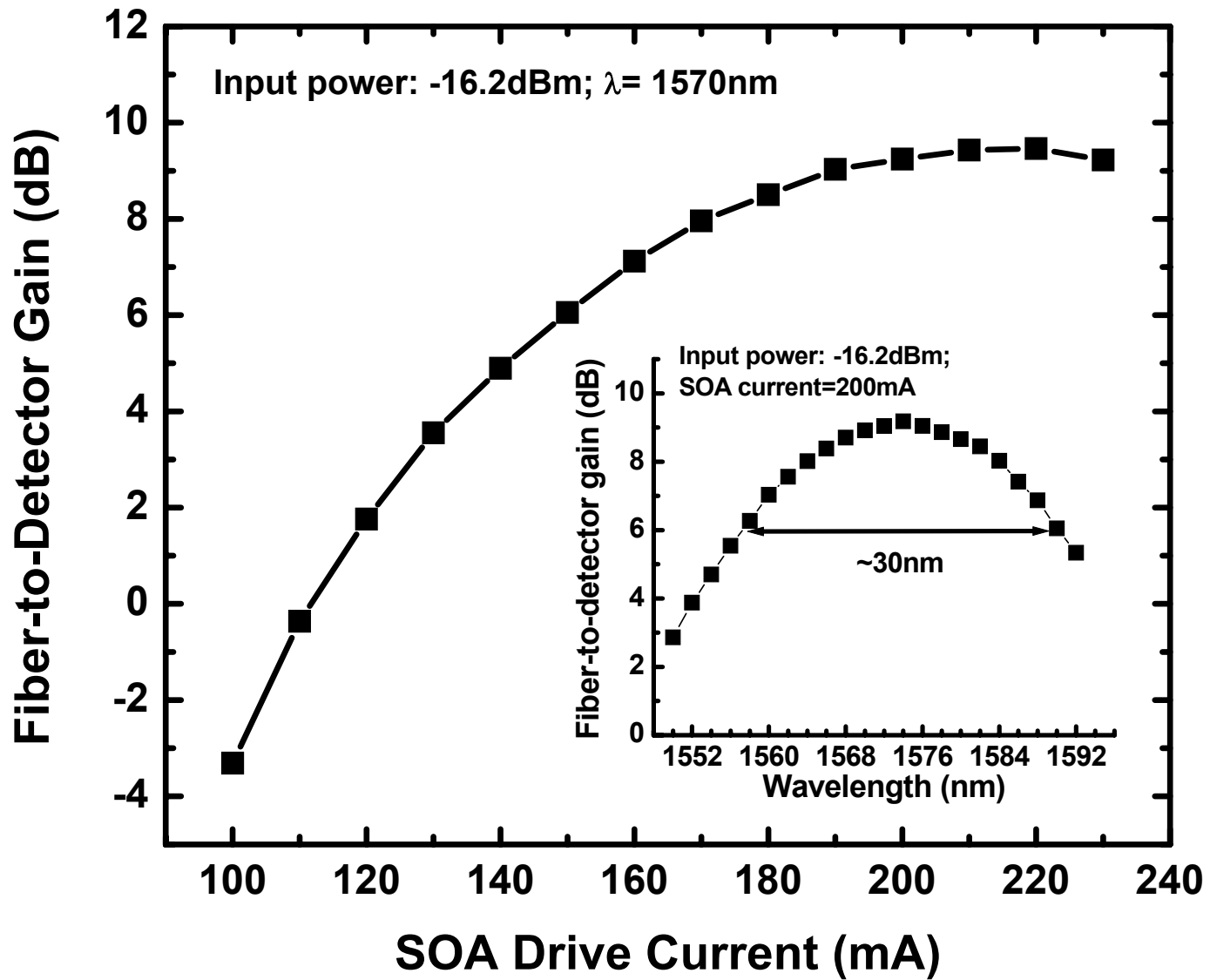


Fig. 15

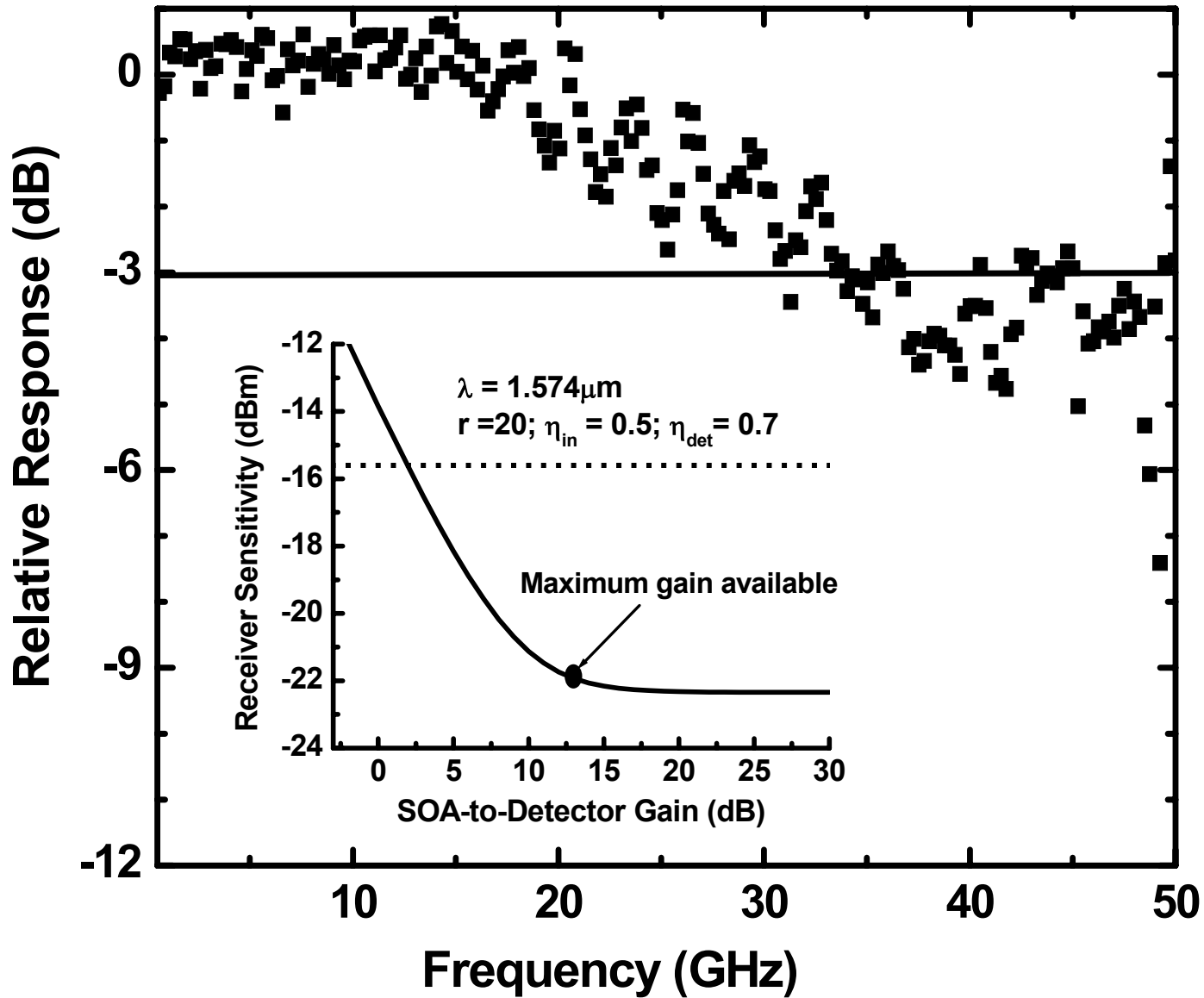


Fig. 16

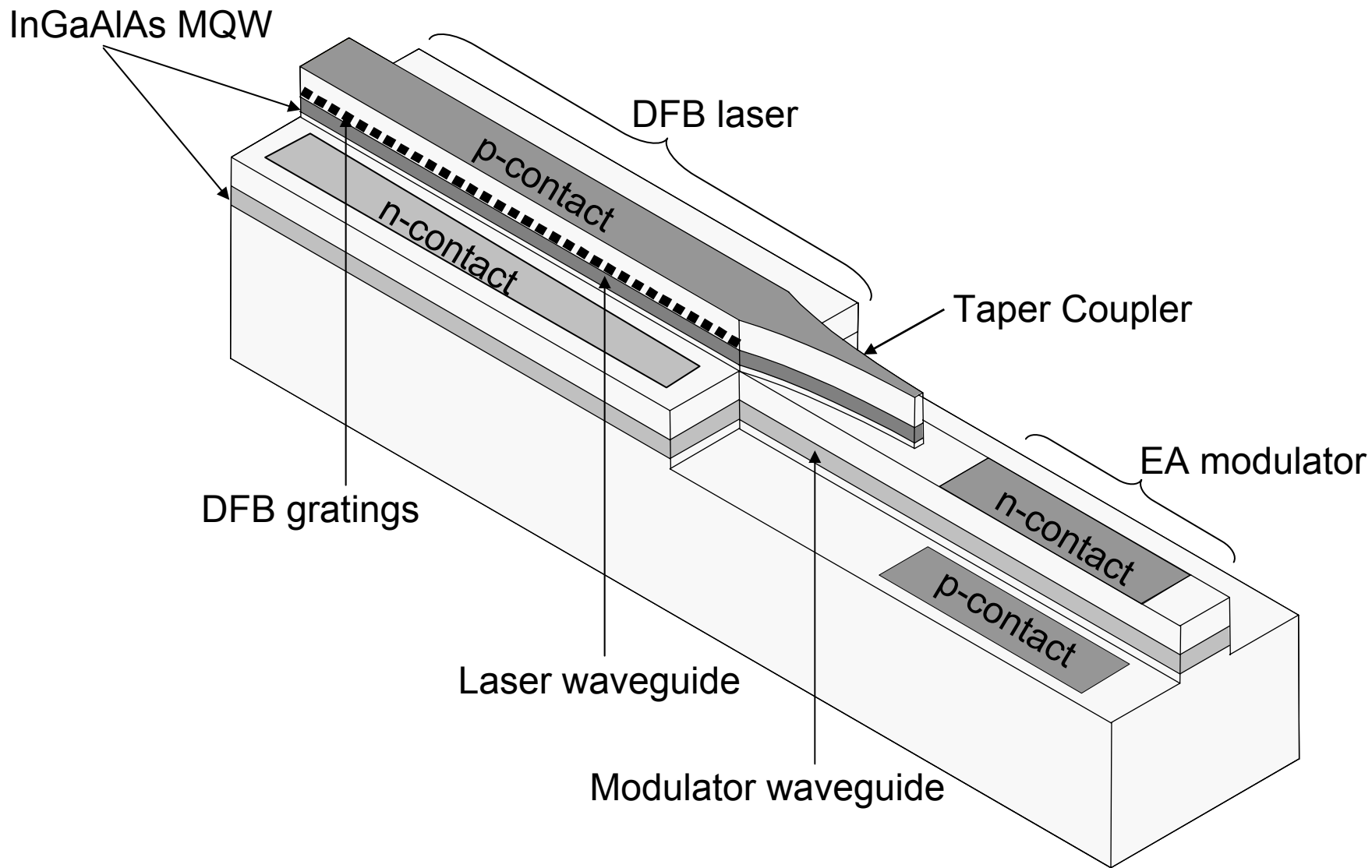


Fig. 17

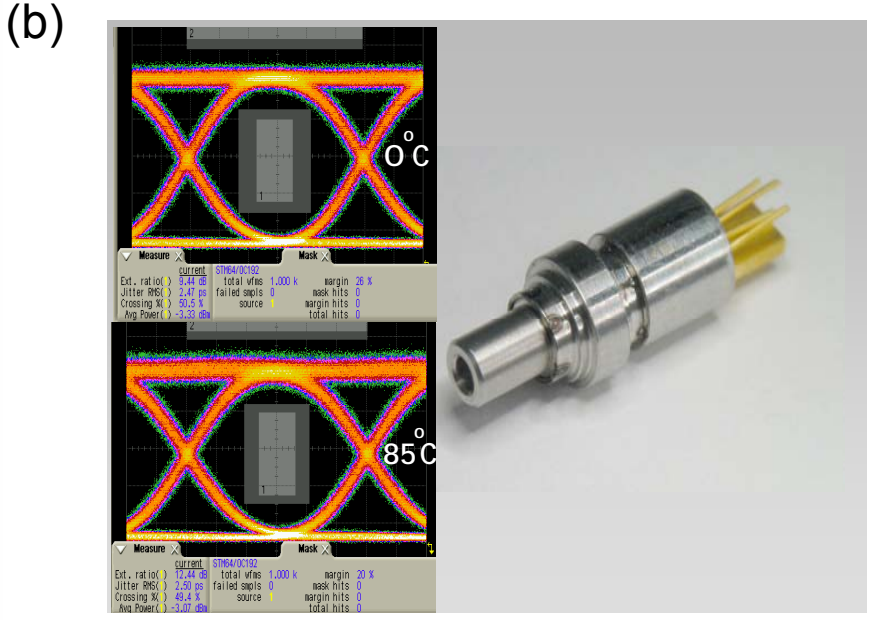
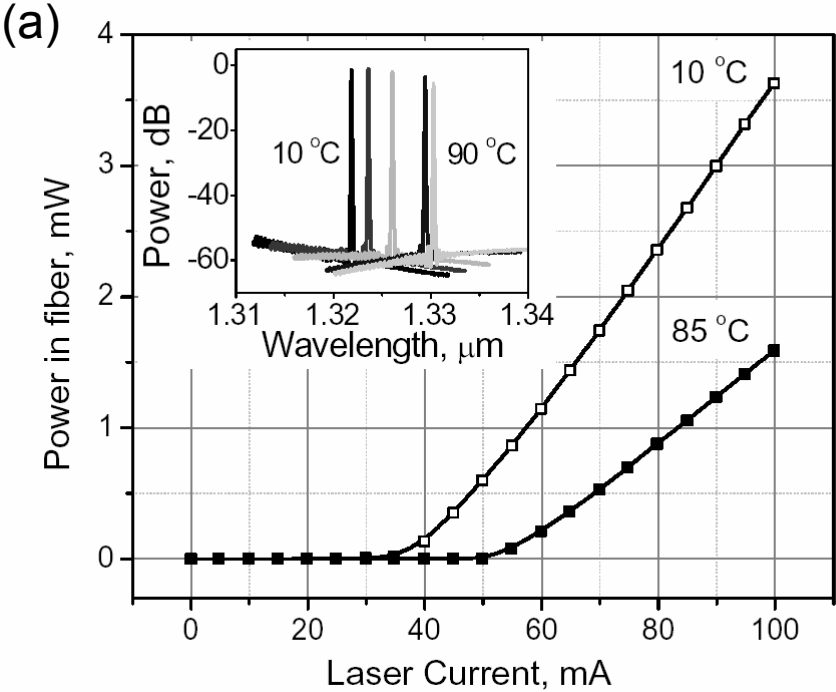


Fig. 18

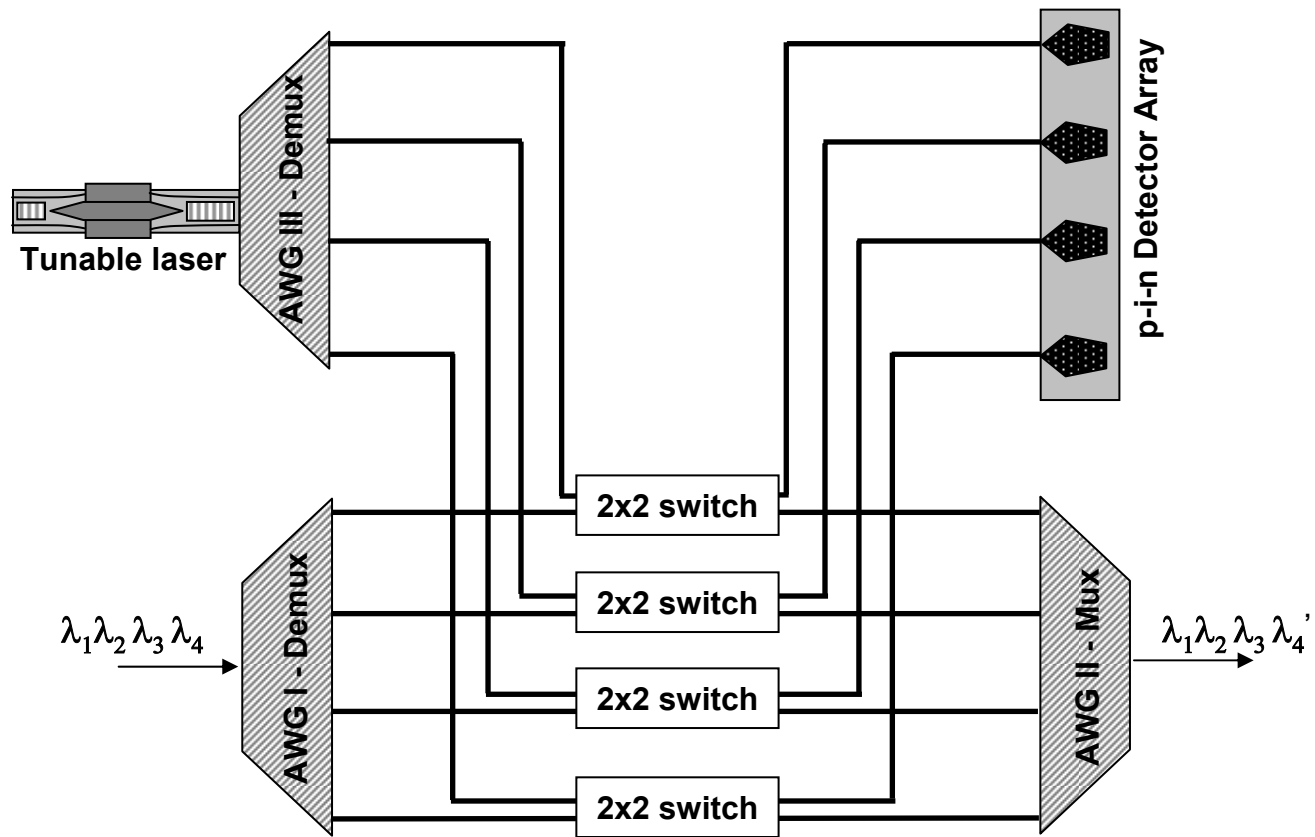


Fig. 19

**A monolithically integrated optical heterodyne receiver using asymmetric twin-waveguide (ATG) technology**

Fengnian Xia, Shubhashish Datta, and Stephen R. Forrest

Princeton Institute for the Science and Technology of Materials (PRISM),

Department of Electrical Engineering, Princeton University

Princeton, NJ 08544

**Abstract**

We demonstrated a monolithically integrated optical heterodyne receiver consisting of an input fiber waveguide, a single frequency distributed Bragg reflector (DBR) laser, a multimode interferometer (MMI) based 3dB coupler, and a pair of SOA/p-i-n modules using a single epitaxial step based on asymmetric twin-waveguide (ATG) technology. The incoming signal was collected by the input fiber waveguide and heterodyned with the on-chip DBR local oscillator (LO) laser using a MMI-based 3dB coupler. A pair of SOA/p-i-n modules then detected the mixed signals. A 3GHz frequency modulated analog coherent optical link was realized using this optical receiver chip and an electronic wideband rectifier narrowband (WIRNA) receiver. In this receiver chip, separation of optical functions (light guiding or filtering, amplification or generation, and detection) into different waveguides allows for optimization of materials for each function without material regrowth. Moreover, regrowth-free monolithic integration of complex combinations of these three optical functions is demonstrated here using this chip based on ATG technology.

**Index Terms**--- analog coherent optical link, asymmetric twin-waveguide technology, and photonic integrated circuits.

Coherent optical communication techniques are attractive due to their potential for high sensitivity and high density wavelength multiplexing [1]. Analog coherent optical links are used for a variety of applications such as optically controlled phased array antennas [2], cable television distribution [3], and wireless communication [4]. Optical coherent receivers play a pivotal role in both digital and analog coherent communication systems. Incorporation of single frequency local oscillator (LO) laser and balanced photodiodes into the coherent optical receiver chip can not only reduce the packaging complexity, but also potentially increase the LO power coupled to the photodiodes and reduce relative intensity noise (RIN) originating from the LO laser. In early reports of integrated heterodyne receivers [5, 6] consisting of a single frequency local oscillator (LO) laser and a pair of p-i-n photodiodes, the components shared the same active material, making their separate optimization difficult. Kaiser *et al.* reported a monolithically integrated polarization diversity heterodyne receiver [7] that required 7 growth steps and 23 photolithographic exposures. In a simplified version of this receiver reported by the same group [8], the growth steps were optimized and reduced to 3. Here, we present an optical heterodyne receiver realized using asymmetric twin-waveguide (ATG) technology. Similar to photonic integrated circuits (PICs) previously demonstrated using this technology [9, 10], separation of optical functions (light guiding or filtering, amplification or generation, and detection) into different waveguides allows for separate optimization of materials for each function without material regrowth, and complex combinations of these three optical functions are defined by post growth processing. Moreover, a 3GHz frequency modulated analog optical link was realized using this

optical heterodyne receiver chip and an electronic wideband rectifier narrowband (WIRNA) receiver [11].

The heterodyne receiver chip is shown schematically in Fig. 1. The frequency modulated incoming optical signal was collected by the input fiber waveguide and heterodyned with the on-chip distributed Bragg reflector (DBR) local oscillator (LO) laser using a multi-mode interferometer-based 3dB coupler [12]. A pair of SOA/p-i-n modules [9] then detected the mixed signals. The receiver epitaxial structure grown by gas source molecular beam epitaxy on a (100) semi-insulating (Fe doped) InP substrate is the same as that reported in [9]. The  $4\mu\text{m}$  wide by  $2.1\mu\text{m}$  thick input fiber waveguide, consisting of three periods of  $0.15\mu\text{m}$  thick InGaAsP (with a bandgap cutoff wavelength of  $\lambda_g = 1.2\mu\text{m}$ ) layers interleaved between  $0.55\mu\text{m}$  thick InP layers, supports an approximately circular mode that allows for low-loss, positionally tolerant fiber coupling. Although the input fiber waveguide is not anti-reflection coated, the  $7^\circ$  tilt of the guide relative to the chip edge efficiently reduces the mode reflectivity [9]. The active and fiber waveguides of the DBR laser are also the same as those reported in [9]. The length of the untapered active region of the DBR laser is  $1.6\text{mm}$ . The tapers on both sides of the DBR laser active region are  $200\mu\text{m}$ , and their width varies from  $1\mu\text{m}$  at the tip to  $3\mu\text{m}$  at the base. We optimized the shape of the taper couplers using the algorithm reported in [13]. The gratings shown in the inset of Fig. 1 on top of the fiber waveguide have a period of approximately  $245\text{nm}$  and a duty cycle of around 40%. The etch depth of the gratings is approximately  $260\text{nm}$ , corresponding to a coupling efficiency  $\kappa$  of about  $40\text{cm}^{-1}$ . The grating lengths are  $450\mu\text{m}$  and  $200\mu\text{m}$  at the front and back laser ends, leading to the

calculated reflectivities for front and back ends of about 90% and 45%, respectively. The MMI based 3dB coupler is 565 $\mu\text{m}$  long and 11 $\mu\text{m}$  wide. The SOA/p-i-n modules are the same as those reported in [9] except that the metallization scheme of the balanced p-i-n photodiodes follows that reported in [12]. The total chip dimension is approximately 8mm long by 300 $\mu\text{m}$  wide.

The fabrication of the heterodyne receiver chip is very similar to that previously reported for ATGA/p-i-n chip [9], with an additional sub-micron grating fabrication process using electron beam lithography (EBL) on top of the fiber waveguide. In this process, the wafer was first coated with 30nm thick  $\text{SiN}_x$  using plasma enhanced chemical vapor-phase deposition (PECVD), and then spin-coated with around 0.2 $\mu\text{m}$  thick, electron sensitive polymethyl methacrylate (PMMA) resist. After EBL writing in selected areas and development, the PMMA mask was transferred to  $\text{SiN}_x$ , followed by PMMA resist mask removal and grating pattern transfer from  $\text{SiN}_x$  to semiconductor using reactive ion etch (RIE).

The responsivities of both SOA/p-i-n modules were measured as a function of the SOA driving current at an input light wavelength ( $\lambda=1.565\mu\text{m}$ ) close to the DBR laser (LO) operating wavelength. Light from a tunable external cavity laser was coupled into the input fiber waveguide with a loss of  $\sim 3\text{dB}$  ( $\sim 1.6\text{dB}$  mode mismatch loss and  $\sim 1.4\text{dB}$  reflection loss) using a lensed single mode fiber with a radius of 11 $\mu\text{m}$ , resulting in a beam diameter of 4 $\mu\text{m}$ . Only the TE mode experiences gain since the quantum wells in active waveguide are compressively strained, hence a polarization controller was used on

the input fiber to maximize the photocurrent. The external responsivities vs. current for both SOA/p-i-n modules are shown in Fig. 2. Here, both SOA/p-i-n responsivities only reach approximately 1A/W at a driving current of 150mA. Compared to the results reported in a simple SOA/p-i-n module [9], this value is about 7dB smaller. This discrepancy can be reconciled by incorporating the extra losses in this chip consisting of the 1.4dB reflection loss, the 3dB intrinsic loss of MMI coupler, and possible additional loss introduced by the MMI coupler [12]. Fig. 2, inset, shows normalized spectrum of the free running DBR laser and the spectrum when the left branch SOA was pumped at 130mA. In both cases, the driving current of the DBR laser was 125mA. The lasing wavelength of the DBR laser red shifted for about 0.4nm due to the heating effect caused by the SOA injection current. On the other hand, the output power of the DBR laser dropped by about 1.5dB probably due to the same reason.

The FM link experiment setup is shown schematically in Fig. 3. The output light from the tunable transmitter laser was modulated using an external phase modulator [11], and then coupled into the input fiber waveguide of the integrated heterodyne receiver chip. The MMI based 3dB coupled mixed the LO light and the signal light. Only the upper branch SOA/p-i-n in Fig. 3 (corresponding to the left branch SOA/p-i-n in Fig. 1) was used for detection in the unpackaged chip. The RF signal was coupled out by a microwave probe, which was also used to bias the photodiode at -2V through an external bias tee. Fig. 4 (a) shows the intermediate frequency (IF) signal when the transmitter was phase modulated at 1.25GHz with a RF power of 10dBm [11]. The laser and SOA driving currents were 125mA and 130mA, respectively. Demodulation was performed using a WIRNA receiver

[11] consisting of a bandpass IF filter, a square law device and a narrowband filter. The bandpass IF filter selected the IF signal and its first lower sideband, then the square law device mixed them, and finally the narrowband filter in baseband rejected all other unwanted components except for the baseband signal. A 3GHz FM link was constructed using this chip and the WIRNA receiver. In this case, the SOA and the DBR laser driving currents were 140mA and 125mA, respectively. The input transmitter power was -3dBm. The total photocurrent was about 1.3mA, consisting of  $\sim 92\mu\text{A}$  induced by SOA spontaneous emission,  $\sim 0.8\text{mA}$  induced by LO laser, and  $\sim 0.4\text{mA}$  induced by the transmitter laser. The 3GHz input RF signal which modulated the transmitter, the WIRNA receiver output with LO (demodulated signal), and the output signal without LO (non-heterodyne term) are shown in Fig. 4(b). As shown in Fig. 4 (b), the link gain was lower ( $\sim 62\text{dB}$ ) compared to that reported in [11] ( $\sim 37\text{dB}$ ), and we attribute this phenomenon to the following two reasons. First, the total photocurrent (hence the transmitter and LO power coupled to the photodiode) was smaller compared to that reported in [11]. On the other hand, single detector configuration intrinsically leads to 3dB loss for both LO and transmitter power. Hence, both IF and its lower sideband power will be 6dB smaller, leading to a demodulated signal power which will be 12dB smaller. Currently, this chip is being packaged and the link performance using both SOA/p-i-n will be investigated.

In conclusion, we demonstrated a monolithically integrated optical heterodyne receiver using asymmetric twin-waveguide (ATG) technology. In this chip, light guiding and filtering components (the input fiber waveguide and MMI coupler), light generation and

amplification components (the DBR laser and SOA), and light detection components (the waveguide photodiodes) were monolithically integrated using separately optimized materials without regrowth. Moreover, a 3GHz frequency modulated optical link was constructed using this chip and a WIRNA receiver in electronic domain. Integration of the heterodyne receiver not only can reduce the packaging complexity, but also potentially increase the LO power detected by the photodiodes, leading to an analog link which operates at the shot noise limit. Besides, we believe that the integration platform (ATG technology) demonstrated here could be a universal solution to a variety of monolithic integration challenges.

The authors gratefully acknowledge DARPA (RFLICs program) for support of this work. The authors also wish to thank Vinod Menon of the City University of New York, Flushing, NY for helpful technical discussions.

## References:

1. G. Agrawal, Fiber-optic communication systems, Chapter 6, John Wiley & Sons, Inc., New York, 1997.
2. R. Taylor and S. R. Forrest, "Steering of an optically driven true-time delay phased array antenna based on a broad-band coherent WDM architecture," IEEE Photon. Technol. Lett., vol. 10, pp. 144-146, 1997.
3. R. Olshansky, R. Gross, and M. Schimdt, "Subcarrier multiplexed coherent lightwave system for video distribution," IEEE J. Select. Areas Commun., vol. 8, pp. 1268-1275, 1990.
4. O. Tonguz and H. Jung, "Personal communications access networks using subcarrier multiplexed optical links," J. Lightwave Technol., vol. 14, pp. 1400-1408, 1996.
5. H. Takeuchi, K. Kasaya, Y. Kondo, H. Yasaka, K. Oe, and Y. Imamura, "Monolithic integrated coherent receiver on InP substrate," IEEE Photon. Technol. Lett., vol. 1, pp. 398-400, 1989.
6. T. Koch, U. Koren, R. Gnall, F. Choa, F. Hernandez-gil, C. Burrus, M. Young, M. Oron, and B. Miller, "GaInAs/GaInAsP multiple-quantum-well integrated heterodyne receiver," Electron. Lett., vol. 25, pp. 1621-1623, 1989.
7. P. Kaiser, D. Trommer, F. Fidorra, H. Heidrich, S. Malchow, D. Franke, W. Passenberg, W. Rehbein, H. Schroeter-Janßen, R. Stenzel, and G. Unterbörsch, "Monolithically integrated polarization diversity heterodyne receivers on GaInAsP/InP," Electron. Lett., vol. 30, pp. 1446-1447, 1994.
8. M. Hamacher, D. Trommer, K. Li, H. Schroeter-Janßen, W. Rehbein, and H. Heidrich, "Fabrication of heterodyne receiver OEIC with optimized integration

- process using three MOVPE growth steps only,” *IEEE Photon. Technol. Lett.*, vol. 8, pp. 75-77, 1996.
9. P. V. Studenkov, M. R. Gokhale, and S. R. Forrest, “Efficient coupling in integrated twin-waveguide lasers using waveguide tapers,” *IEEE Photon. Technol. Lett.*, vol. 11, pp. 1096-1098, 1999.
  10. F. Xia, J. Wei, V. M. Menon, and S. R. Forrest, “Monolithic integration of a semiconductor optical amplifier and a high bandwidth p-i-n photodiode using asymmetric twin-waveguide technology,” *IEEE Photon. Technol. Lett.*, vol. 15, pp. 452-454, 2003.
  11. S. Datta, S. Agashe and S. R. Forrest, “A high bandwidth analog optical heterodyne RF link with high dynamic range and low noise figure,” *IEEE Photon. Technol. Lett.*, vol. 16, pp. 1733-1735, 2004.
  12. S. Agashe, S. Datta, F. Xia, and S. R. Forrest, “A monolithically integrated long-wavelength balanced photodiode using asymmetric twin-waveguide technology,” *IEEE Photon. Technol. Lett.*, vol. 16, pp. 236-238, 2004.
  13. F. Xia, V. Menon, and S. R. Forrest, “Photonic integration using asymmetric twin-waveguide technology. I. Concepts and theory,” to be published in Jan. 2005 in *IEEE J. Select. Topics Quantum Electron.*

## Figure Captions

Fig. 1: Three-dimensional schematic view of the integrated heterodyne receiver chip.

Inset: scanning electron micrograph of the gratings fabricated on top of the fiber waveguide.

Fig. 2: Responsivity of left/right branch SOA/p-i-n versus SOA injection current. Inset:

free running LO laser spectrum and the spectrum when left SOA was pumped at 130mA.

Fig. 3: Schematic view of the setup of the frequency modulated optical analog link.

Fig. 4: (a) Intermediate frequency signal when transmitter laser was phase-modulated at a

frequency of 1.25GHz. (b) 3GHz input RF signal, WIRNA receiver output with LO laser (demodulated signal) and output without LO laser (non-heterodyne term).

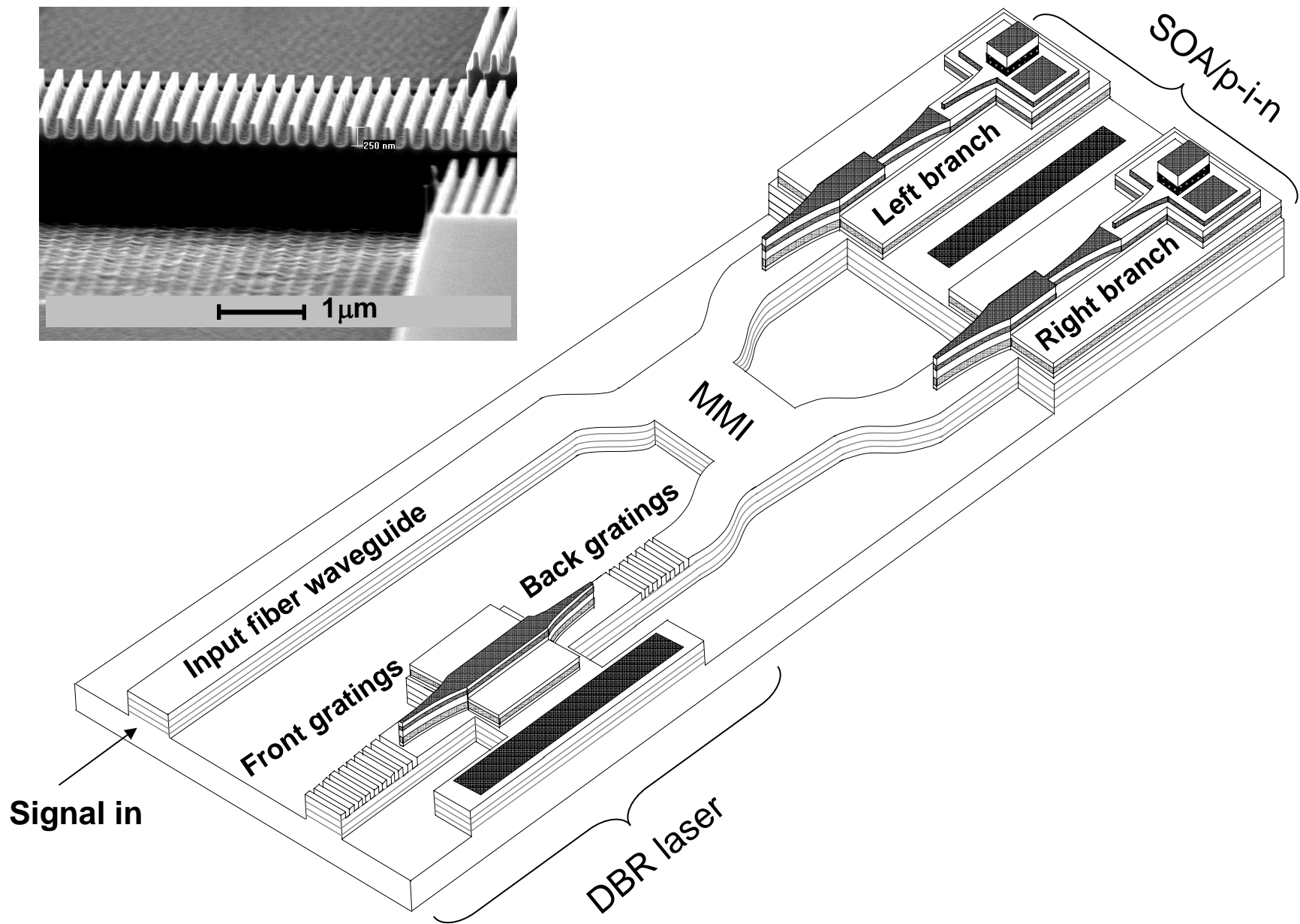


Fig. 1, XIA et al.

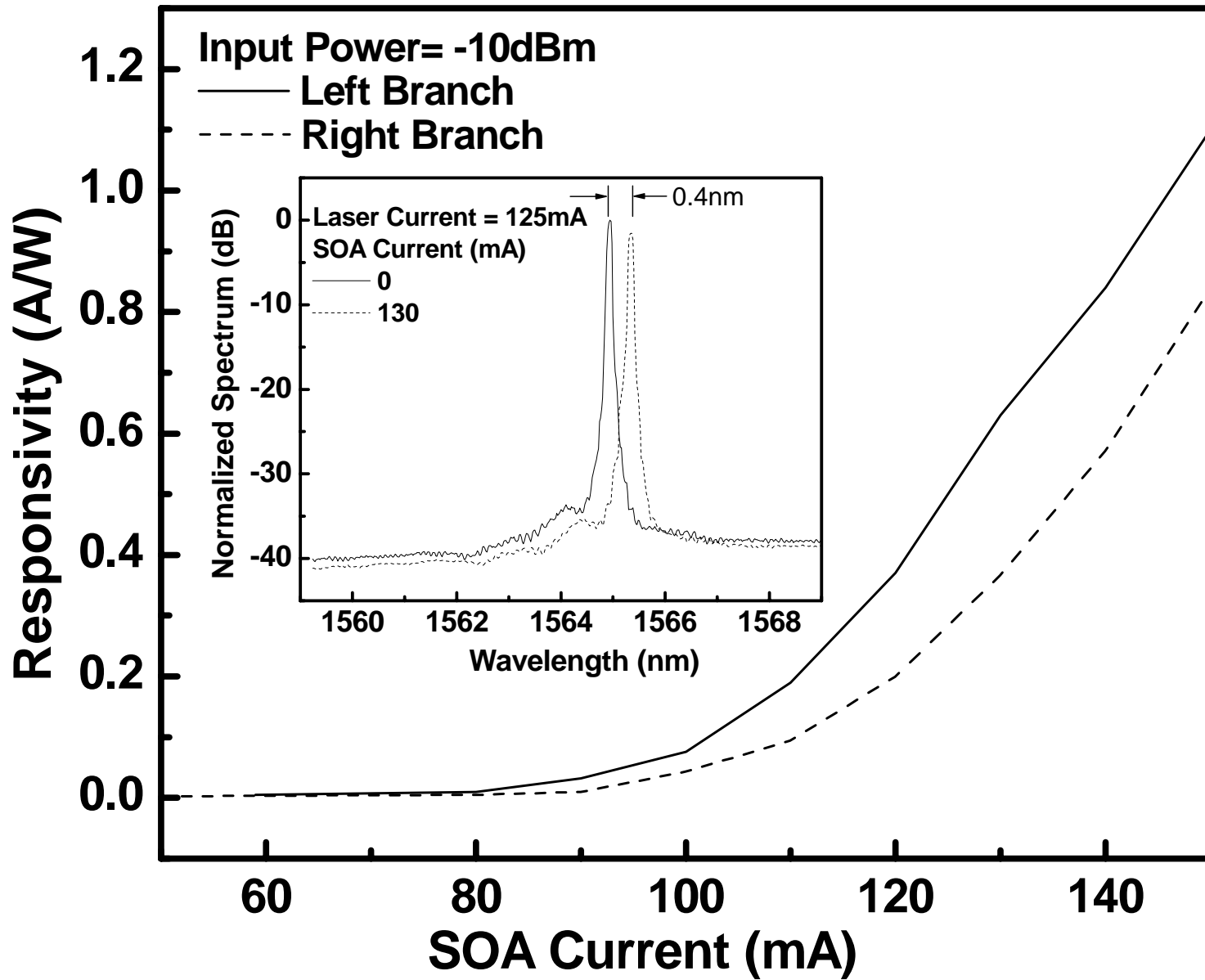


Fig. 2, XIA et al.

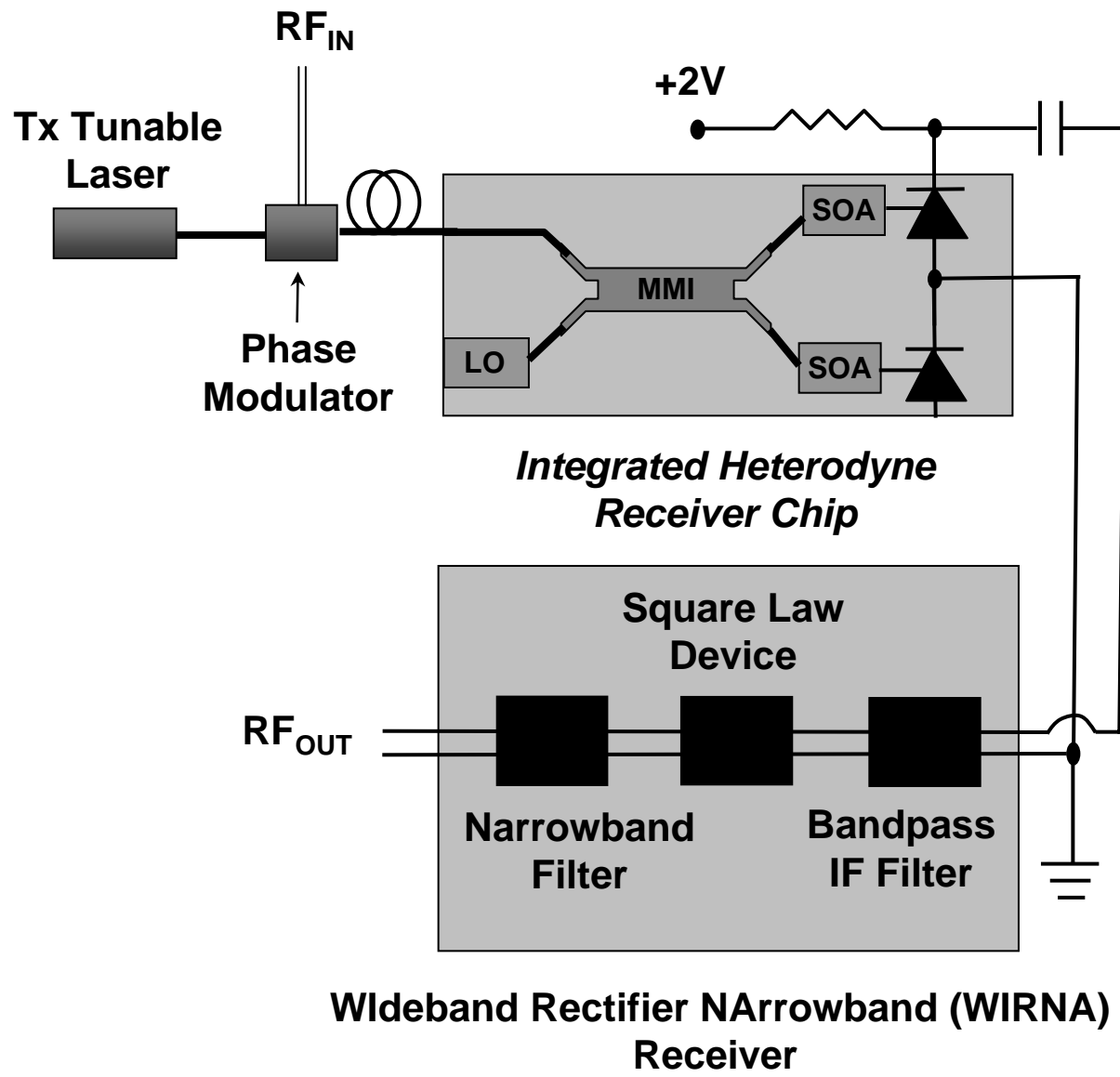
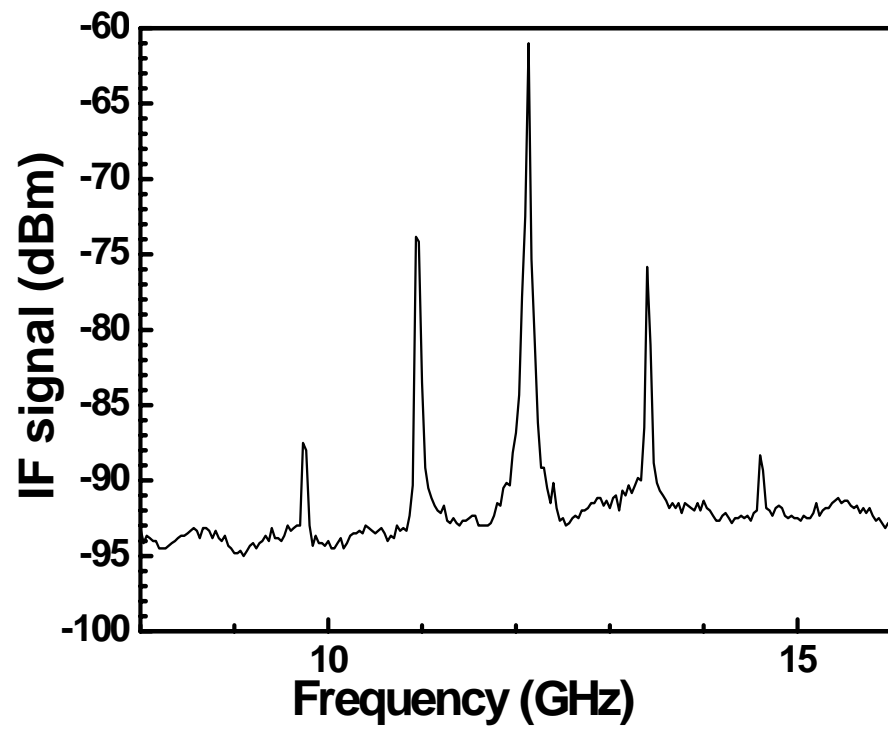
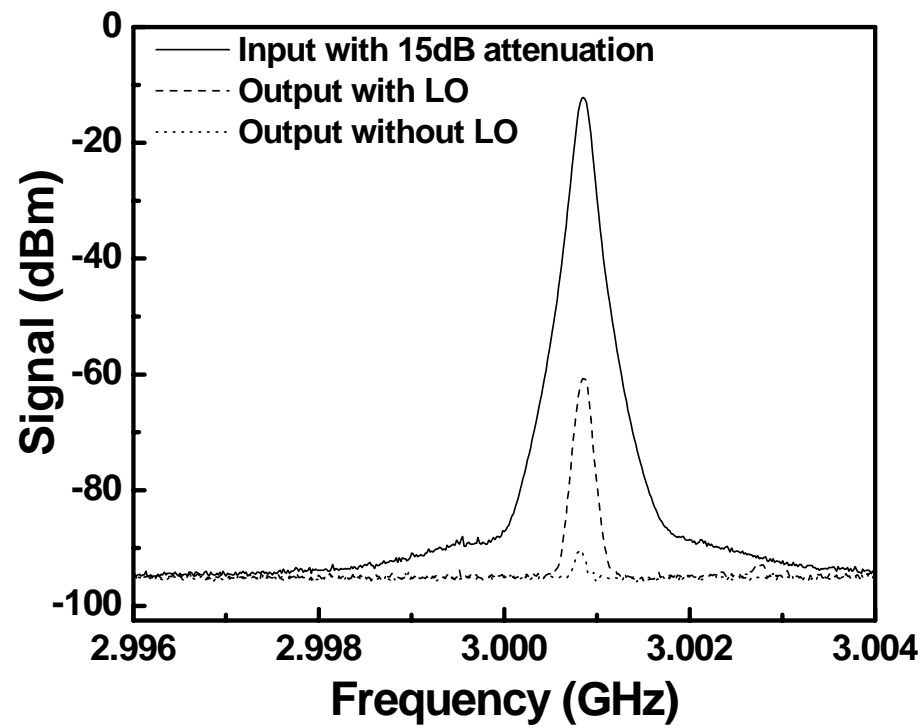


Fig. 3, XIA et al.



(a)



(b)

Fig. 4, XIA et al.